NASA/TM–2010-215862

The Interaction of the Solar Wind with *Solar Probe Plus* — 3D Hybrid Simulation

Report 1: The study for the distance 4.5Rs

Alexander S. Lipatov, Edward C. Sittler, Richard E. Hartle, and John F. Cooper

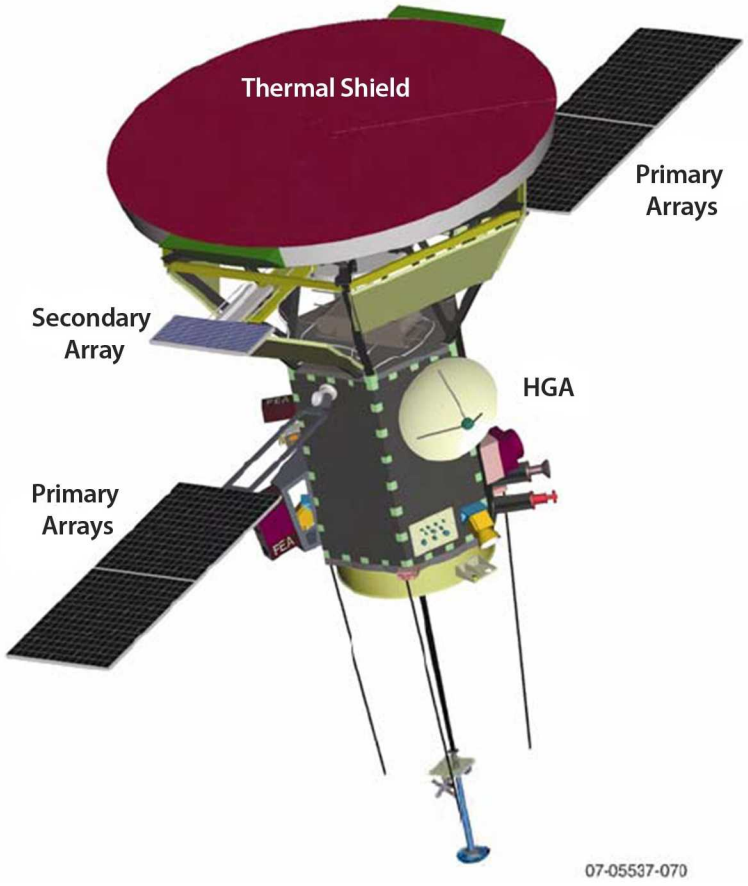

December 2010

The NASA STI Program Office … in Profile

Since its founding, NASA has been dedicated to the advancement of aeronautics and space science. The NASA Scientific and Technical Information (STI) Program Office plays a key part in helping NASA maintain this important role.

The NASA STI Program Office is operated by Langley Research Center, the lead center for NASA's scientific and technical information. The NASA STI Program Office provides access to the NASA STI Database, the largest collection of aeronautical and space science STI in the world. The Program Office is also NASA's institutional mechanism for disseminating the results of its research and development activities. These results are published by NASA in the NASA STI Report Series, which includes the following report types:

- TECHNICAL PUBLICATION. Reports of completed research or a major significant phase of research that present the results of NASA programs and include extensive data or theoretical analysis. Includes compilations of significant scientific and technical data and information deemed to be of continuing reference value. NASA's counterpart of peer-reviewed formal professional papers but has less stringent limitations on manuscript length and extent of graphic presentations.
- TECHNICAL MEMORANDUM. Scientific and technical findings that are preliminary or of specialized interest, e.g., quick release reports, working papers, and bibliographies that contain minimal annotation. Does not contain extensive analysis.
- CONTRACTOR REPORT. Scientific and technical findings by NASA-sponsored contractors and grantees.
- CONFERENCE PUBLICATION. Collected papers from scientific and technical conferences, symposia, seminars, or other meetings sponsored or cosponsored by NASA.
- SPECIAL PUBLICATION. Scientific, technical, or historical information from NASA programs, projects, and mission, often concerned with subjects having substantial public interest.
- TECHNICAL TRANSLATION. English-language translations of foreign scientific and technical material pertinent to NASA's mission.

Specialized services that complement the STI Program Office's diverse offerings include creating custom thesauri, building customized databases, organizing and publishing research results . . . even providing videos.

For more information about the NASA STI Program Office, see the following:

- Access the NASA STI Program Home Page at http://www.sti.nasa.gov/STI-homepage.html
- E-mail your question via the Internet to help@sti.nasa.gov
- Fax your question to the NASA Access Help Desk at (443) 757-5803
- Telephone the NASA Access Help Desk at (443) 757-5802
- Write to:
  NASA Access Help Desk
  NASA Center for AeroSpace Information
  7115 Standard Drive
  Hanover, MD 21076

NASA/TM–2010-215862

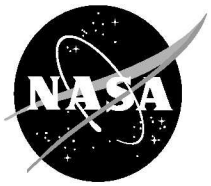

The Interaction of the Solar Wind with *Solar Probe Plus* — 3D Hybrid Simulation

Report 1: The study for the distance 4.5Rs

Alexander S. Lipatov
The Goddard Earth Sciences and Technology Center,
University of Maryland, Baltimore County, Baltimore, MD

Edward C. Sittler
NASA Goddard Space Flight Center Greenbelt, MD

Richard E. Hartle
NASA Goddard Space Flight Center Greenbelt, MD

John F. Cooper
NASA Goddard Space Flight Center Greenbelt, MD

Prepared under NASA Grant NCC5–494

January 1, 2008 to -DQXDU\ 1, 2009
Prepared for Dr. Madhulika Guhathakurta
NASA Headquarters, Code SMD
Washington, DC 20546

National Aeronautics and
Space Administration

Goddard Space Flight Center
Greenbelt, Maryland 20771

December 2010

Available from:

NASA Center for AeroSpace Information
7115 Standard Drive
Hanover, MD 21076-1320

National Technical Information Service
5285 Port Royal Road
Springfield, VA 22161

Abstract. Our report devotes a 3D numerical model of the interaction of the solar wind with the Solar Probe Plus (SPP) spacecraft. The SPP model includes 3 main parts, namely, a non-conducting heat shield, a support system, and cylindrical section or spacecraft bus that contains the particle analysis devices and antenna. The simulation was performed using 3D hybrid code which describes the proton dynamics by the particle motions whereas the electrons are considered in a fluid approximation. One observes an excitation of the low frequency Alfvén and whistler type wave directed by the magnetic field with an amplitude about of (0.06-0.6) V/m. The compression waves and the jumps in an electric field with an amplitude about of (0.15-0.7) V/m were also observed. The wave amplitudes are comparable to or greater than previously estimated max wave amplitudes that SPP is expected to measure. The results of our hybrid simulation will be useful for understanding the plasma environment near the Solar Probe Plus spacecraft. Future simulation will take into account the charging of the spacecraft, the charge separation effects, an outgassing from heat shield, a photoionization and an electron impact ionization effects near the spacecraft. We also need to perform a longer simulation in order to receive a "steady-state" solution with a formation of a plasma wake in quasi-parallel interaction.

Numerical simulation studies; **Key words:** Solar wind; Alfvén waves, Whistlers, Ionospheres; Atmospheres; Induced magnetospheres; Magnetic barrier; Satellites

1. Introduction

The numerical simulation of the interaction of space plasma with spacecraft devices plays a key-role in their design. The study of the excitation of waves near a rapidly moving body has long history starting from the quasi-analytical approach (see e.g. Alpert (1974) and the references thereby) to the recent electrostatic modeling. While the electrostatic studies produced very important information concerning the charging of spacecraft, plasma void and wake, the problem of excitation of the electromagnetic waves upstream and downstream flow near spacecraft are great interest for onboard measurement in the SW, magnetosphere and ionosphere. This is especially true for SPP where new regimes of solar wind plasma are being explored. The simulation provides the general characteristics of the plasma environment and the electromagnetic field distribution near the probe and at it's surface. The external surface of the "SPP" consists of a conducting part and an insulating part. It moves in the supersonic/subsonic and superalfvénic/subalfvénic solar wind flow.

In the first approximation the plasma environment near the "Solar Probe+" may be similar to the plasma environment near the Moon with a weakly conducting surface. In the case of a non-conducting model of the Moon the solar wind particles penetrate the surface on the day-side of the Moon whereas on the night-side a plasma wake with the low-density void is formed. On the day side of the Moon's surface the plasma particles are absorbed, and the perturbation region forms a thin boundary layer of thickness $\delta \sim c/\omega_{\rm pe} \propto 1\,{\rm km}$ at 1 AU. (Neugebauer, 1960). On the night side the perturbation region is bounded by a surface of weak perturbations forming a cone with half-apex

angle $\sin^2\theta = 1/M_A^2 + 1/M_S^2$ ($M_A \propto 8$ and $M_S \propto 8$ are the Alfvén and sound Mach numbers, $V_A \approx 50\,\mathrm{km/s}$, $w_{th} \approx 50\,\mathrm{km/s}$, $U \approx 400\,\mathrm{km/s}$, and $\theta \approx 10°$) (Whang, 1969; Lipatov, 1976).

No bow shock or oblique Mach cone are formed. The perturbation of the magnetic field inside the wake is determined by drift currents [Wang, 1968; Wang, 1969; Wang and Ness, 1970; Lipatov 1976, Lipatov, 2002]. Kinetic instabilities may also play a role in wake dynamics. Hybrid simulation of the interaction between supersonic plasma flow and a weakly conducting body shows formation of a strong Mach cone outside the plasma wake [Lipatov, Motschmann, et al., 2005].

2. Formulation of the Problem and Mathematical Model

2.1. Solar Wind Simulation Model

The interaction of solar wind particles with the "SPP" is more complicated because the gyroradius of the protons (for Maxwellian core of the velocity distribution $50 - 500\,\mathrm{km}$) is much larger than the size of the spacecraft (2-3m). For energetic component the ion gyroradius may be extremely large with respect to the spacecraft. So the kinetic approximation for ions is an essential part of the mathematical model. The electron gyroradius may vary in range from 2.5×10^2m at Earth orbit to much smaller scale near Sun. Therefore, electrons need a fluid-kinetic approximation to study the plasma environment along the "Solar Probe+" trajectory.

We expect to study the plasma environment near the "SPP" by various simulations; e.g., (a) standard hybrid simulation (ion in kinetic approximation, electron in fluid

approach) on the large scale; (b) fully kinetic implicit simulation with kinetic model for electrons and ions (see e.g. Hewett and Langdon, 1987; Lipatov and Lobachev, 1996; Lipatov, 2002; Damiano, Sydora, Samson, 2003; Lipatov and Rankin, 2008) incorporated in the large scale hybrid model. The last simulation will take into account the charge separation near the surface of the spacecraft and finite electron gyroradius effects. We will take into account the realistic distribution of the spacecraft surface's conductivity. Our simulation will serve as an expert system for design of the "Solar Probe Plus" spacecraft. The present model of the interaction of the solar wind with the SPP does not take into account several effects in plasma environment near spacecraft. Future simulation will take into account the charging of the spacecraft, the charge separation effects, an outgassing from heat shield, a photoionization and an electron impact ionization effects near the spacecraft.

To study the interaction of the solar wind with the SPP spacecraft we use a quasi-neutral hybrid model for ions and electrons.

In our coordinate system the X axis is parallel to the solar wind velocity - $\mathbf{U_0}$, Z is aligned with the equatorial plane, and $\mathbf{Y} = \mathbf{Z} \times \mathbf{X}$ is perpendicular to equatorial plane and anti-aligned with the $\mathbf{E} = -\frac{1}{c}\mathbf{U} \times \mathbf{B}$ electric field (electric field points upward).

In the hybrid simulations described here, the dynamics of upstream ions is described in a kinetic approach, while the dynamics of the electrons is described in a hydrodynamical approximation.

The single particle ion distribution function $f_i(t, \mathbf{x}, \mathbf{v})$ has to fulfil the

Vlasov/Boltzmann equation

$$\frac{\partial}{\partial t} f_i + \mathbf{v} \frac{\partial}{\partial \mathbf{x}} f_i + \frac{\mathbf{F}}{M_i} \frac{\partial}{\partial \mathbf{v}} f_i = F_{coll}, \tag{1}$$

where $\mathbf{F}$ symbolizes forces due to electric and magnetic fields acting on the ions, F_{coll} is the collision term. In this paper we use the particle-mesh model for ion dynamics instead of the Vlasov equation, Eq. (1).

The single ion particle motion is described by the equations (see, e.g. Eqs. (1) and (14) from [Mankofsky, Sudan and Denavit, 1987]):

$$\frac{d\mathbf{r}_{i,l}}{dt} = \mathbf{v}_{i,l}; \quad \frac{d\mathbf{v}_{i,l}}{dt} = \frac{e}{M_\mathrm{i}} \left(\mathbf{E} + \frac{\mathbf{v}_{i,l} \times \mathbf{B}}{c} \right) - \frac{m_e \nu_{ie}}{M_i e n_i} \mathbf{J}. \tag{2}$$

Here we assume that the charge state is $Z_i = 1$ and that all ions have the same mass M_i. $\mathbf{U}_i$ and $\mathbf{J}$ denote the charge-averaged velocity of all (incoming and pickup) ions and the total current, Eq. (6). The subscript i denotes the ion population and the index l is the macro-particle index. ν_{ie} is collision frequencies between ions and electrons, that may include Coulomb collisions and collisions due to particle-wave interaction. Note that the collision rates used in Eq. (2) must depend on individual velocities of ions and electrons. However, we use the effective resistivity η, $\eta = \sigma^{-1} = m_e/(ne^2\tau_e)$, where $\tau_e = \nu_{ie}^{-1}$. The electrical conductivities may be estimated as

$$\sigma_\perp = \sigma_1 T_e^{3/2}, \quad \sigma_\parallel = 1.92\sigma_\perp, \quad \sigma_1 = 0.9 \times 10^{13}/((\Lambda/10)Z_i)\,\mathrm{s}^{-1} \cdot \mathrm{eV}^{-3/2}, \tag{3}$$

where T_e denotes the electron temperature and Λ is the Coulomb logarithm (see, e.g., pages 215-216 from [Braginskii, 1965]). For the typical solar wind parameters

$T_e = 100\,\mathrm{eV}$ (electron temperature) and $n_0 = 10^4 \mathrm{cm}^{-3}$ (density) the electrical conductivities are $\sigma_\perp \approx 4.7 \times 10^{13}\,\mathrm{s}^{-1}$ and $\sigma_\parallel \approx 9.2 \times 10^{13}\,\mathrm{s}^{-1}$.

In our simulation we use the low (much smaller than the real value) effective conductivity to suppress "shot" noise and for modeling Solar Probe Plus's bus; hence, we must keep the first collision term in the right hand side of Eq. (2).

In the nonradiative limit Ampère's law is given by

$$\frac{4\pi}{c}\mathbf{J} = \nabla \times \mathbf{B}; \tag{4}$$

and the induction equation (Faraday's law) by

$$\frac{1}{c}\frac{\partial \mathbf{B}}{\partial t} + \nabla \times \mathbf{E} = 0. \tag{5}$$

The total current is given by

$$\mathbf{J} = \mathbf{J}_\mathrm{e} + \mathbf{J}_\mathrm{i}; \quad \mathbf{J}_\mathrm{i} = e n_i \mathbf{U}_i. \tag{6}$$

We further assume quasi-neutrality

$$n_\mathrm{e} \approx n_i. \tag{7}$$

The equation of motion of the electron fluid takes the form of standard generalized Ohm's law (e.g. Braginskii, 1965):

$$\mathbf{E} = \frac{1}{e n_\mathrm{e} c}(\mathbf{J}_\mathrm{e} \times \mathbf{B}) - \frac{1}{e n_\mathrm{e}}\nabla p_\mathrm{e} + \frac{m_\mathrm{e}}{e}\nu_{e,i}\frac{\mathbf{J}}{ne} - \frac{m}{e}\frac{d}{dt}\mathbf{U}_e, \tag{8}$$

where $p_\mathrm{e} = n m_\mathrm{e} \langle v_\mathrm{e}'^2 \rangle / 3 = n_\mathrm{e} k_B T_\mathrm{e}$, and v_e' are the scalar electron pressure and the thermal velocity of electrons, and the electron current is estimated from Eq. (6). The last term

on the right side of Eq. (8) is the electron inertial term. At $5R_s$ we have $n_0 = 10^4\,\mathrm{cm}^{-3}$, $v'_\mathrm{e} = 5000\,\mathrm{km/s}$, and from Eq. (3) one gets $\sigma_{e,i} = 0.4 \times 10^{14}\,\mathrm{s}^{-1}$ for background plasma parameters.

Since we suppose that electron heating due to collisions with ions is very small, the electron fluid is considered adiabatic. For simplicity we assume that the electron pressure may be represented as:

$$p_\mathrm{e} \propto n_\mathrm{i}^{5/3}. \tag{9}$$

We also assume that $n_\mathrm{e} \approx n_\mathrm{i}$. Otherwise, we have to calculate the electron pressure from heat balance for electrons (see, e.g., Braginski, 1965) taking into account the heat fluxes. The ion kinetic approach allows us to take into account the effects of anisotropy of ion pressure, the finite gyroradius effects, the asymmetry of plasma flow around the Solar Probe Plus, and to estimate the particle flux at the surface of the spacecraft. Remember that the fluid models which account only for the scalar (i.e., isotropic) ion pressure may result in an extra-expansion of the ions along the magnetic field. Our plasma model may support the kinetic ion cyclotron wave and electron fluid cyclotron waves.

2.2. SPP Spacecraft Model

Figure 1 shows a scheme of the SPP spacecraft, a system of coordinates and a direction of the plasma flow and magnetic field. The SPP model includes 3 main parts, namely, a non-conducting heat shield (1), a support system (2), and cylindrical section or spacecraft bus (3) that contains the particle analysis devices and antenna. The heat shield has the following geometrical parameters: the diameter, $D_{shield} = 2.7\,\mathrm{m}$, and the

thickness = 0.335 m. The gap between the heat shield and cylindrical section is equal 1.188 m. The cylindrical section or bus has a diameter equals 1.026 m and a length 1.188 m. We also take into account the effective resistivity of the Solar Probe+'s bus, the heat shield and the gap between the heat shield and the spacecraft bus:

$$\rho_{bus} = (1-15)\times 10^{-3}\, ohm\cdot m; \quad \rho_{shield} = (3-15)\, ohm\cdot m; \quad \rho_{gap} = (3-15)\times 10^{-3}\, ohm\cdot m \tag{10}$$

Our code solves equations (1) - (5), (6) - (9). Here we note that the gap has several trusses to provide mechanical interface between bus and heat shield. If electrical conductivity of trusses high enough that differential charging between spacecraft bus and heat shield is low then the heat conduction from heat shield to spacecraft bus maybe too high. We are not aware of the exact number at this time with regard to truss electrical conductivity parameters.

Initially the computational domain contains only supersonic (subsonic) solar wind flow with a homogeneous spatial distribution and a Maxwellian velocity distribution. The magnetic field and electric fields are $\mathbf{B} = \mathbf{B_0}$ and $\mathbf{E} = \mathbf{E_0} = -\mathbf{U}_0 \times \mathbf{B}_0$. Inside Solar Probe spacecraft electromagnetic fields are $\mathbf{E}$ =0 and $\mathbf{B} = \mathbf{B}_0$, and the bulk velocities of ions and electrons are also equal to zero. In the cases examined here we choose spiral angle of field $\theta_{bu} = 11° - 45°$.

Far upstream ($x = -DX/2$), the ion flux is assumed to have a Maxwellian distribution,

$$f = n_\infty (\pi v_{th}^2)^{-3/2} \exp\left[-\frac{(\mathbf{v}-\mathbf{U})^2}{2v_{th}^2}\right], \tag{11}$$

where v_{th} and $\mathbf{U}$ are the thermal and the bulk velocities of the solar wind plasma flow. We have not included the importance of the field aligned strahl electrons which are non-Maxwellian.

Far downstream, we use a buffer zone to provide the return of the particle with negative value of the u velocity component. We also adopted Sommerfeld's radiation condition for the magnetic field. On the side boundaries ($y = \pm DY/2$ and $z = \pm DZ/2$), unperturbed boundary conditions were imposed for incoming flow particles and the electromagnetic field. At Solar Probe Plus's surface the particles are reflected or absorbed. There is no boundary condition for electromagnetic field, and we also use our equations for the electromagnetic field, Eqs. (4-5) and 8 inside Solar Probe Plus spacecraft but with internal conductivity and the bulk velocity that is calculated from the particles. In this way the jump in the electric field is due to the variation of the value of the conductivity and bulk velocity across the Solar Probe Plus bus's surface. Note that the position of the center of the bottom of the heat shield of Solar Probe Plus is $x = 0, y = 0, z = 0$.

The three-dimensional computational domain has dimensions $DX = 10L$, $DY = 8L$, and $DZ = 8L$, where $L = D_{shield}/2 = 1.35\,\mathrm{m}$ is a radius of heat shield. We used mesh of $401 \times 301 \times 301$ grid points, and 9×10^8 particles for protons for a homogeneous mesh computation. The time step for the particle update, Δt_p satisfies the condition $v_{max}\Delta t_p \leq \min(\Delta x, \Delta y, \Delta z)/16$, whereas the time step for the electromagnetic field time integration Δt_f satisfies the condition $v_{max}\Delta t_f \leq \min(\Delta x, \Delta y, \Delta z)/6400$. Note that the grid spacing are the following: $\Delta x = \Delta y = \Delta z = 0.036\,\mathrm{m}$.

The relationship between dimensional (U, E, B, p_e, n, T) and dimensionless (U', E', B', p'_e, n', T') parameters may be expressed via the dimensional upstream values as follows:

$$\mathbf{U} = \mathbf{U}' U_0, \quad \mathbf{E} = \mathbf{E}' B_0 U_0 / c, \quad \mathbf{B} = \mathbf{B}' B_0, \quad p_\mathrm{e} = p_{e'} p_{e0},$$

$$n = n' n_0, \quad T = T' M_\mathrm{i} U_0^2, \tag{12}$$

whereas the dimensional time and distance may be expressed via the bulk velocity U_0 and characteristic scale $L = D_{shield}/2$:

$$t = t' L / U_0, \quad x = x' L. \tag{13}$$

The global physics in SPP's environment is controlled by a set of dimensionless independent parameters such as Alfvén Mach number M_A, the ion and electron plasma betas β_i, β_e, the electron/proton mass ratio m/M_p, diffusion lengths, and the ion gyroradius $\epsilon = \rho_\mathrm{ci}/L$. Here $\rho_\mathrm{ci} = U_0/(eB/M_\mathrm{i}c) = M_\mathrm{A} c/\omega_\mathrm{pi}$ and the ion plasma frequency $\omega_\mathrm{pi} = \sqrt{4\pi n_0 e^2/M_\mathrm{i}}$. The actual value of the proton gyroradius is about $(0.31 - 2.5)\,\mathrm{km}$ using the above formulas using the above formulas. The grid spacing has the value $\Delta_x = L/50 = 0.036\,\mathrm{m}$. In order to study the ion kinetic effect, the ion gyroradius has to be resolved on the grid.

2.3. Numerical Method

We employed a standard particle-in-cell (PIC) method with a homogeneous grid. The time integration of the particle equations of motion uses a leapfrog scheme. The time integration of the electromagnetic field equations uses an implicit finite difference

scheme (see, e.g., Lipatov (2002)).

The finite difference approximation for the electric field and the electron velocity equations may be produced by the following way:

$$d\nabla \times (\nabla \times \mathbf{E}^{n+\theta}) + A\mathbf{E}^{n+\theta} + (\nabla \times \mathbf{E}^{n+\theta}) \times \mathbf{I}$$

$$+g((\nabla \times (\nabla \times \mathbf{E}^{n+\theta})) \times \mathbf{B}^n) = \mathbf{Q}, \tag{14}$$

where

$$d = \frac{m}{M}\frac{\epsilon^2}{M_{\mathrm{A}}^2} + \theta n_{\mathrm{e}} l_{\mathrm{d}}^* \Delta t, \quad A = n_{\mathrm{e}}, \quad g = \frac{\theta \Delta t \epsilon}{M_{\mathrm{A}}^2}, \tag{15}$$

$$\mathbf{I} = \frac{\theta \epsilon \Delta t}{M_{\mathrm{A}}^2}\left(\frac{M_{\mathrm{A}}^2}{\epsilon}\sum_{k=1}^{N_{\mathrm{s}}} \mathbf{J}_k^{n+1/2} - \nabla \times \mathbf{B}^n\right), \tag{16}$$

$$\mathbf{Q} = -\left(\sum_{k=1}^{N_{\mathrm{s}}} \mathbf{J}_k^{n+\frac{1}{2}} - \frac{\epsilon}{M_{\mathrm{A}}^2}\nabla \times \mathbf{B}^n\right) \times \mathbf{B}^n - \frac{\epsilon \beta_{\mathrm{e}}}{2M_{\mathrm{A}}^2}\nabla p_{\mathrm{e}} + n_{\mathrm{e}} l_{\mathrm{d}}^* \nabla \times \mathbf{B}^n. \tag{17}$$

and

$$\mathbf{U}_{\mathrm{e}} = \mathbf{U}_{\mathrm{i}} - \epsilon \mathbf{J}/(M_{\mathrm{A}}^2 n_{\mathrm{e}}). \tag{18}$$

In the case with adiabatic electrons one can split the total electric field into the sum of inductive ($\vec{E}_1$) and electrostatic ($\vec{E}_2$) fields:

$$\vec{E} = \vec{E}_1 + \vec{E}_2, \tag{19}$$

where $\vec{E}_2$ satisfies the condition

$$\nabla \times \vec{E}_2 = 0. \tag{20}$$

Then we can solve (14) for component $\vec{E}_1$ neglecting ∇p_{e}. The electrostatic electric field $\vec{E}_2$ can be calculated from p_{e} (Lipatov, 2002) because

$$\vec{E}_2 = -\frac{1}{en_{\mathrm{e}}}\nabla p_{\mathrm{e}}. \tag{21}$$

Let us consider two meshes. The first mesh contains the nodes i, j, k, which are located in the center of a cell. It is used for the computation of the density, current, bulk velocity, electron pressure and inductive electric field. The second mesh contains the nodes $i \pm 1/2, j \pm 1/2, k \pm 1/2$, which are located at the corners of a cell. This mesh is used for the computation of the magnetic field components, electrostatic field and final electric field. Let us assume that $\vec{J}_{\rm i}^{n+1/2}$, $\omega_{\rm pe}$ and $n_{\rm i}$ are known at time level $n + 1/2$. Then, expressing $\nabla \times \vec{E}_1^{n+\theta}$ and $\nabla \times (\nabla \times \vec{E}_1^{n+\theta})$ via central finite differences at each cell center, one can obtain the following 3×3 matrix equation:

$$\vec{L} \cdot \vec{E}_{i,j,k}^{n+\theta} = \vec{F}\left(\vec{E}_{i\pm1,j\pm1,k\pm1}^{n+\theta}\right). \tag{22}$$

Equation (18) may be solved by iteration. In each iteration the electric field on the right side is given. The iteration continues until some convergence criterion is satisfied. At the same time the electrostatic field $\vec{E}_2$ is calculated at from Eq. 21.

The second term on right side of Eq. 17 keeps a large parameter, so that a strong shot noise in a density computation may cause a strong oscillation in the electric field. Note that the first term (electron inertia) on the left side of the Eq. 14 has a large coefficient so that this term may play very important role in damping of the low frequency waves. In this report we assume that $m/M_p = 0$ and we neglect the electron inertia term (first term on the left side) in Eq. 14.

We used different time steps for particle and field pushing (subcycling). The code was optimized for parallel computation using OpenMP parallel environment. However, the staff from the Computational and Information Sciences and Technology Office

(NASA GSFC) is working on the conversion the our code to the MPI environment. That may allow us to use a distributed memory parallel computer system for our computation.

Since the gyroradius must be resolved, a grid point spacing of less than 1 gyroradius is required in order to avoid numerical dispersion and dissipation. On the other hand, good statistics are required, therefore a sufficiently large number of particles per cell have to be used (i.e., to obtain low "shot" noise, which manifests itself as fluctuations in the numerical plasma parameters due to a small number of particles per cell).

A multiscale simulation will be conducted using adaptive mesh and particle refinement techniques with composite grids. This code exploits a splitting-of-particles procedure to keep a low level of "shot" noise on the finer mesh. At the end of the global time step we use the synchronization for the values of the electromagnetic field on coarse and finer meshes. A.S. Lipatov has developed a version of the Complex Particle Kinetic method (see, Hewett, 2003) [in collaboration with D.W. Hewett (LLNL) and M.R. Combi (Univ. of Michigan)] for the case of multiple plasma beams (inter-penetrating flow) which allows us a reduction in computational resources by factors of 100 - 1000 in comparison with standard PIC simulation (Lipatov, 2008a). These codes were optimized for parallel computation using MPI and OMP.

3. Results of the Simulation

To study the interaction of the solar wind with the SP+ we use the following sets of the solar wind plasma parameters: $\beta_{\rm i} = 0.1$; $\beta_{\rm e} = 0.000125 - 0.00125 - 0.1$;

magnetic field, $B_0 = 1500 - 6250\,\mathrm{nT}$; bulk velocity $U_0 = 400 - 200\,\mathrm{km/s}$, density $n_{SW} = 5 \times 10^3 - 10^4\,\mathrm{cm}^{-3}$, Alfvén Mach number $M_\mathrm{A} = 1.2 - 10$ and $\theta_{bu} = 11° - 45°$. Table 2 shows the all parameters that correspond the case: (a), (b) and (c). These parameters correspond to the values of the motional electric field $E_0 = U_0 B_0 \approx 1.24\,\mathrm{V/m}$ for $r = 5R_s$ and $E_0 \approx 0.3\,\mathrm{V/m}$ for $r = 9.5R_s$. The higher values of the magnetic field and density correspond to the distance from the Sun of about $5R_s$, whereas the lower values correspond to the distance of 9.5 R_s. We present here the results of simulation for the first case. The time step for electromagnetic field update is 48 times smaller in a quasi-parallel case than it the time step in an oblique case. In the present simulation, we use a reduced value for the electron plasma beta, $\beta_e = 0.001$ to reduced the oscillation in the polarization electric field because of the large value of the dimensional proton gyroradius, $\epsilon = \rho_p/L = 1840 - 230$, see the equations (13-17).

3.1. Quasi-parallel Interaction of the Solar Wind with Solar Probe+

Let us consider first the global picture of the interaction of the solar wind with Solar Probe+ in the quasi-parallel case, $\theta_{bu} = 11°$. We have performed the simulation of this case only for a short time because of the small time step that needs to be done for numerical stability. One simulation takes around 1 month for computing with 16 processors on the "shared memory" Palm/Explore machine. Figure 2 shows 2D cut for proton density in the $y - x$ and $z - x$ planes. We see the picture of the solar wind flow around the spacecraft. Behind the heat shield a density profile forms a cone due to expansion of the external plasma into the gap between the heat shield and the

spacecraft bus. Behind the spacecraft bus there is no lunar-type plasma wake due to low value of the Mach number, $M_A = 1.2 - 1.5$, and high values of the plasma betas, $\beta_p = 0.1$. $\beta_e = 0.000125$ (case a, Table 2). Possibly, the plasma wake may form in longer simulations.

In this case the current closure near a spacecraft is very complicated and is directed by the external magnetic field. Figures 3, 5 and 7 show the 2D cuts for the electric field at $t = 0.014T_{ce}$. Note that T_{ce} is the electron gyroperiod. In upstream one sees the linear perturbation in the electric field in form of whistler/Alfvén waves in upstream and downstream regions at the beginning of simulation $t = 0.014T_{ce}$. The value of perturbation in the electric field is about of $\delta E \approx 0.02E_0$, $E_0 \approx 1.24\text{V/m}$).

Figures 4, 6 and 8 show 1-D cuts for the electric field profile along the x, y and z axis through the point $x = 1.5L, y = 0$ and $z = 0$.

Far from the spacecraft, the value of perturbation in the electric field component, E_x, is about of $\delta E_x \approx (0.001 - 0.005)E_0$ in the y- direction, whereas $\delta E_x \approx 0.01E_0$ in the z- direction. The value of perturbation in the electric field components, E_y and E_z, is about $\delta E_y \approx 0.5E_0$ (whistler type waves) in the x- direction (upstream and downstream), and $\delta E_y \approx 0.01E_0$ in the y- direction, and $\delta E_y \approx 0.01E_0$ in the z- direction. The value of perturbation in the electric field component, E_z, is about of $\delta E_z \approx 0.05E_0$ in the x- direction, $\delta E_z \approx 0.05E_0$ in the y- direction, and $\delta E_z \approx 0.1E_0$ in the z- direction.

Near spacecraft, the E_x profile has a jump, $\delta E_x = -1000E_0$ behind the heat shield. Near spacecraft one sees an excitation of strong Alfvén waves with an amplitude ,

$\delta E_x \approx 0.005 E_0$ along y axis, and $\delta E_x \approx (0.02 - 0.15) E_0$ along the z axis. We also see a jump in E_y component of the electric field, $\delta E_y \approx 0.1 E_0$ in y direction and $\delta E_y \approx 0.05 E_0$ in z direction. The components E_y and E_z have a jump, $\delta E \approx (0.02 - 0.5) E_0$ in y and z directions.

Figures 9, 10 and 11 demonstrate 2D cuts for the magnetic field. At the front of the heat shield a formation of the magnetic field barrier is observed. At the side parts of the computational domain compression waves were observed in simulations. The value of perturbation in the magnetic field is about of $\delta B \approx 0.02 B_0$ ($\approx 120\,\mathrm{nT}$ for $B_0 \approx 6200\,\mathrm{nT}$.).

Let us consider the result of simulation at the later time, $t = 0.29 T_{ce}$ ($t = 0.04 T_{transit}$), where $T_{transit}$ is the time for particle transit from the left boundary to the right boundary of the computational domain. Figure 12 shows a 2D cuts for proton density in the $y - x$ and $z - x$ planes. The perturbation in the electromagnetic field reaches the saturation level, since the density distribution showed no change during the simulation.

Figure 13, 15 and 17 show the 2D cuts for the electric field at later time $t = 0.29 T_{ce}$. Since the density distribution had not changed during the simulation and the perturbation in the electromagnetic field reaches the saturation level (left hanging). We do not see any strong transverse perturbation in the electric fields in the upstream region, but we do see large perturbations in the downstream region. The value of these perturbations is about of $\delta E \approx 1.0 E_0 \approx 1.24\mathrm{V/m}$.

Figures 14, 16 and 18 shows 1-D cuts for the electric field profile along the x, y and

z axis through the point $x = 1.5L, y = 0$ and $z = 0$.

Far from the spacecraft in the downstream region, the value of perturbation in the electric field component, E_x, is about of $\delta E_x \approx 0.005E_0$ in the y- direction, whereas $\delta E_x \approx 0.01E_0$ in the z- direction. The value of perturbation in the electric field components, E_y and E_z, is about of $\delta E \approx 2.0E_0$ (whistler type waves) in the x- direction (downstream), Fig. 14, and $\delta E_y \approx 0.05E_0$ in the y- direction, and $\delta E_y \approx 0.03E_0$ in the z- direction, Fig. 16. The value of perturbation in the electric field component, E_z, is about of $\delta E_z \approx 0.05E_0$ in the x- direction, $\delta E_z \approx 0.025E_0$ in the y- direction, and $\delta E_z \approx 0.025E_0$ in the z- direction, Fig. 18.

Near spacecraft, the E_x profile has a jump, $\delta E_x = 250E_0$ behind the cylindrical section (conducting bus). We also see a jump in E_y component of the electric field, $\delta E_y \approx (0.5 - 0.75)E_0$ in y direction and $\delta E_y \approx 0.2E_0$ in z direction. The component E_z has a jump, $\delta E \approx (0.15 - 0.2)E_0$ in y and z directions.

Figures 19, 20 and 21 demonstrate 2D cuts for the magnetic field. At time, $t = 0.29T_{ce}$ ($t = 0.04T_{transit}$), we do not observe any magnetic field barrier near the heat shield. At the side parts of the computational domain compression waves were observed in the simulations. The value of perturbation in the magnetic field is about of $\delta B \approx 0.02B_0$.

Let us consider the results of the simulation with higher value of $\beta_e = 0.025$ (case b, Table 2). Figure 22 shows a 2D cuts for proton density in the $y - x$ and $z - x$ planes. We see the picture of the solar wind flow around the spacecraft. Behind the heat shield a density profile forms a cone due to expansion of the external plasma into

the gap between the heat shield and the spacecraft bus. Behind the spacecraft there is no lunar-type plasma wake due to low value of the Mach number, $M_A = 1.2 - 1.5$.

The general picture of the interaction of the solar wind with spacecraft is very close to the picture that was described above. Figure 23, 25 and 27 show the 2D cuts for the electric field at $t = 0.014 T_{ce}$. Figures 24, 26 and 28 shows 1-D cuts for the electric field profile along the x, y and z axis through the point $x = 1.5L, y = 0$ and $z = 0$. In upstream and downstream we observe the linear perturbation in the electric filed - whistler/Alfv'en waves. The value of perturbation in the electric field (E_y, E_z) in upstream and downstream is about of $\delta E \approx 0.4 E_0$ (whistler type waves) in the x-direction, and the wavelength much larger than in case with $\beta_e = 0.000125$.

Far from the spacecraft, the value of perturbation in the electric field component, E_x, is about of $\delta E_x \approx 0.002 E_0$ in the y- direction, whereas $\delta E_x \approx 0.005 E_0$ in the z-direction. In other directions we observe perturbation - $\delta E_y \approx 0.01 E_0$ in the y- direction, and $\delta E_y \approx 0.01 E_0$ in the z- direction. The value of perturbation in the electric field component, E_z, is about of $\delta E_z \approx 0.05 E_0$ in the x- direction, $\delta E_z \approx 0.01 E_0$ in the y-direction, and $\delta E_z \approx 0.01 E_0$ in the z- direction.

Near spacecraft, the E_x profile has a jump, $\delta E_x = -20 E_0$ before the heat shield and $\delta E_x = 30 E_0$ behind the cylindrical section. Near spacecraft we see an excitation of strong oblique Alfvén (magnetosonic) waves with an amplitude , $\delta E_x \approx (0.005 - 0.01) E_0$ along y axis, and $\delta E_x \approx (0.02 - 0.15) E_0$ along the z axis. We also see a jump in E_y component of the electric field, $\delta E_y \approx 20 E_0$ in y direction and $\delta E_y \approx 0.05 E_0$ in z direction. The components E_z has a jump, $\delta E \approx 0.04 E_0$ in the y and $\delta E \approx 20 E_0$ in the

z directions.

Figures 29, 30 and 31 demonstrate 2D cuts for a magnetic field. At the front of the screen a formation of a magnetic field barrier was observed. At the side parts of the computational domain compression waves were observed in simulations. The value of perturbation in the magnetic field is about of $\delta B \approx 0.02 B_0$.

Let us consider now the result of simulation with $\beta_e = 0.025$ at the later time, $t = 0.03 T_{ce}$ ($t = 0.01 T_{transit}$), where $T_{transit}$ is the time for particle transit from the left boundary to the right boundary of the computational domain. Figure 32 shows a 2D cuts for proton density in the $y - x$ and $z - x$ planes. The perturbation in the electromagnetic field reaches the saturation level, since the density distribution has not changed during the simulation.

Figure 33, 35 and 37 show the 2D cuts for the electric field at $t = 0.03 T_{ce}$. Since the density distribution had not changed during the simulation the perturbation in the electromagnetic field reached the saturation levels. Figures 34, 36 and 38 shows 1-D cuts for the electric field profile along the x, y and z axis through the point $x = 1.5L, y = 0$ and $z = 0$.

Far from the spacecraft, the value of perturbation in the electric field component, E_x, is about of $\delta E_x \approx (0.01 - 0.015) E_0$ in the y- direction, whereas $\delta E_x \approx 0.01 E_0$ in the z- direction. The value of perturbation in the electric field components, E_y and E_z, is about of $\delta E_y \approx 0.02 E_0$ (whistler/Alfv'en waves) in the x- direction (upstream and downstream), and $\delta E_y \approx 0.01 E_0$ in the y- direction, and $\delta E_y \approx 0.01 E_0$ in the z- direction. The value of perturbation in the electric field component, E_z, is about of

$\delta E_z \approx 0.05E_0$ in the x- direction, $\delta E_z \approx 0.05E_0$ in the y- direction, and $\delta E_z \approx 0.1E_0$ in the z- direction.

Near spacecraft, the E_x profile has a jump, $\delta E_x = -1000E_0$ behind the heat shield. Near spacecraft we see an excitation of a strong Alfvén waves with an amplitude , $\delta E_x \approx 0.005E_0$ along y axis, and $\delta E_x \approx (0.02 - 0.15)E_0$ along the z axis. We also see a jump in E_y component of the electric field, $\delta E_y \approx 20E_0$ in y direction and $\delta E_y \approx 0.05E_0$ in z direction. The component E_z has a jump, $\delta E \approx (0.02 - 20.)E_0$ in y and z directions.

Figures 39, 40 and 41 demonstrate 2D cuts for the magnetic field. At the front of the heat shield a formation of the magnetic field barrier or build up was observed. At the side parts of the computational domain a compression waves were observed in simulations. The value of perturbation in the magnetic field is about of $\delta B \approx 0.02B_0$.

3.2. Oblique Interaction of the Solar Wind with Solar Probe Plus

Let us consider the interaction of the solar wind with Solar Probe Plus in the oblique case, $\theta_{bu} = 45°$, and $M_A = 2$ at time, $t = 1.875T_{transit}$, where $T_{transit}$ is the time for particle transit from the left boundary to the right boundary of the computational domain (case c, Table 2). The simulation demonstrates the formation of the plasma wake. A strong perturbation in the plasma density along the wake was observed, Fig. 42. The density profile is a little bit disturbed near the side boundaries. One may see that SP+ bus is located inside the low plasma density cavern. This means particle instrument in wake may see nothing. Figures 43-45 and 46-45 show the distribution of the electric and magnetic fields, respectively. The asymmetry of the distributions in **E**

and **B** appears to be caused by the finite gyroradius effects of incoming protons. A weak perturbation of the magnetic field was observed near the SP+ spacecraft: compression of the upstream magnetic field and decompression in the plasma wake, Fig. 48.

One can see the asymmetry in the distribution relative to the x-axis due to the angle between the bulk velocity and the upstream magnetic field and to the y-axis due to effects of the finite ion gyroradius, Fig. 47. The value of perturbation in the magnetic field is about of $\delta B \approx 0.02 B_0$, Fig. 48. Table 3 accumulates the values of the perturbation in the electric and magnetic field and the jumps in the normal component of the electric field at the surface of the spacecraft bus. Note that strong jumps at the bus surface may be due to the specific boundary condition and the future computations may reduce these values.

4. Conclusions

3D hybrid simulations of the interaction of the solar wind plasma with Solar Probe Plus, have demonstrated several new features:

- In the quasi-parallel case the current closure near a spacecraft is very complicated and is directed by the external magnetic field. At the front of the heat shield a formation of the magnetic field barrier was observed whereas a formation of the strong whistler/Alfvén waves were observed in both upstream and downstream regions. At the side parts of the computational domain compression waves were observed in simulations. The values of the electric field oscillation near the

spacecraft bus may be the same order as the maximum of expected electric field in an antenna (see, Table 1 from Murphy et al, 2008).

- In case of the oblique magnetic field $\theta_{bw} = 45°$ the magnetic barrier is formed at the front of the heat shield.

- The simulations were performed for the distance $r = 4.5\,R_s$ because of a numerical limitation for convergence in the iterations of the electric field equation (Lipatov,2002). For distance $r = 9.5\,R_s$ one needs to design another algorithm for solving the electric field equation, Eq. 8. We are now trying to use the implicit "splitting of operator" method to solve the generalized Ohm's law equation, Eq. 8.

- Our computations were performed only for the case $\beta_e = 0.00125 - 0.025$ that is smaller at least by factor of 4 than realistic values. For higher value of β_e one needs computation with significantly larger number of the macro-particles. It may be possible with the use of more than 320 processors on "SGI-Columbia" parallel computer system (NASA Ames Center) with MPI environment to achieve a good scalability.

- All simulations for $\theta_{bu} = 11°$ were performed for a short period physical time because the present code needs a lot of time steps to compute the electric field. A more effective algorithm needs to be designed for longer period of the physical time. It will be important for an investigation of the low plasma density cavern formation around the SP+ bus.

- Simulated electric field perturbations are comparable to or exceed maximum electric field one expects for the SP+ spacecraft. Therefore, a wake design of SP+ electric field plasma-wave antenna may not be a viable option for SP+.

Future work that is still needed:

Hybrid simulations

- Simulation with higher value of $\beta_e = 0.1$, higher value of the solar wind velocity $U_0 \approx 400 - 800\,\mathrm{km/s}$, and lower value of the magnetic field $B_0 \approx 1500\,\mathrm{nT}$.

- Simulations with various boundary condition on the spacecraft bus and trusses configuration;

- Simulation with much higher space resolution and a number of macro-particles to reduces a "shot" noise in density and polarization electric field;

- Longer simulations in order to receive a "steady-state" solution with a formation of a plasma wake in quasi-parallel interaction.

The results of these simulations will be included in the final Report.

Full kinetic simulations

- Simulation that will take into account the charging of the spacecraft, the charge separation effects, an outgassing from heat shield, a photoionization and an electron impact ionization effects near the spacecraft.

Acknowledgments.

E.C.S. and A.S.L. were supported in part by grant of the NASA' Grant N 93672302010619 (PI - E.C. Sittler) through NASA GSFC and GEST Center UMBC. Computational resources were provided by the NASA's Supercomputing Centers at the NASA Goddard (SGI shared memory parallel system "Palm/Explore") and the Ames (SGI shared memory parallel system "Columbia") Centers through the NASA Computational Projects SMD-07-0458, and SMD-08-0636.

References

Alpert, Ya.L., Waves and satellites in the near-earth plasma. Studies in Soviet space. (Translated from Russian by J.B. Barbour), Consultants Burea, New York, pp. 205 (1974).

Bale, S.D., C.J. Owen, J.I. Bougret, K. Goetz et al., Geophys. Res. Lett., **24**, 1427 (1997).

Braginskii, S.L., Transport processes in a plasma. In: Leontovich, M.A. (Ed.), Reviews of Plasma Physics. Consultants Bur., New York, p. 205 (1965).

Damiano, P.A., R.D. Sydora, J.C. Samson, Hybrid magnetohydrodynamic-kinetic model of standing shear Alfv'en waves, *J. Plasma Physics*, **69**(4), 277-344 (2003).

Hewett, D., Fragmentation, merging, and internal dynamics for PIC simulation with finite size particles, J. Comput. Phys., **189**, 390-426 (2003).

Hewett, D.W. and A.B. Langdon, Electromagnetic Direct Implicit Plasma Simulation, *J. Comput. Phys.*, **72**, 121 (1987).

Lipatov, A.S., *About the three-dimensional structure of the lunar wake. Cosmic Res.* **14**, 103 (1976).

Lipatov, A.S., *The Hybrid Multiscale Simulation Technology. An Introduction with Application to Astrophysical and Laboratory Plasmas*, Springer-Verlag, Berlin, Heidelberg, New York, pp. 1-403 (2002).

Lipatov A.S., V.A. Lobachev, Numerical Kinetic Simulation of the One-dimensional

Structure of Oblique and Quasi-Perpendicular Collisionless Shocks, *Cosmic Res. (Sov. J. Kosmich. Issledov.)*, **34**(5), 420 (1996).

Lipatov, A.S., U. Motschmann, T. Bagdonat, and J.-M. Grießmeier, The interaction of the stellar wind with an extrasolar planet – 3D hybrid and drift-kinetic simulations, *Planet. Space Sci* **53**, 423-432 (2005).

Lipatov, A.S., Merging for complex particle kinetic modeling of the multiple plasma beams (inter-penetrating flows), *J. Comput. Phys.* (to be submitted) (2008a).

Lipatov, A.S., R. Rankin, Electron acceleration by th Alfv'en wave pulses: 2.5D hybrid modeling, *Physics of Plasma*, (to be submitted, 2008b).

Mankofsky, A., Sudan, R.N., and Denavit, J., Hybrid Simulation of Ion Beams in Background Plasma. J. Comput. Phys. 70, 89-116 (1987).

Marconi, M.L., Dagum, L. and Smyth, W.H., Hybrid fluid/kinetic approach to planetary atmospheres: An example of an intermediate-mass body. Astrophys. J. 469, 393-401 (1996).

Murphy, N., et al., Thermal Design Consideration for the Solar Probe Electric Field Antenna, Feb. 2008.

Neugebauer, M., *Phys. Rev. Lett.*, **4**(1), 6 (1960).

Wang, Y.C., Theoretical study of the magnetic field in the lunar wake, *Phys. Fluids* **11**(8), 1713 (1968)

Wang, Y.C., Field and plasma in the lunar wake, *Phys. Rev.* **186**(1), 143 (1969)

Wang, Y.C., N.F. Ness, *J. Geophys. Res.* **75**(31), 6002 (1970)

Received _____

Table 1. Important values of the electromagnetic field in an antenna from "Thermal Design Consideration for the Solar Probe Plus Electric Field Antenna by Murphy et al., Feb. 2008".

	$4R_s$	$12R_s$	$20R_s$
$U \times B$	$12\,\mathrm{V/m}$	$2.5\,\mathrm{V/m}$	$0.5\,\mathrm{V/m}$
E_{max}, DC	$1\,\mathrm{V/m}$	$0.1\,\mathrm{V/m}$	$0.1\,\mathrm{V/m}$
E_{max}, 100kHz	$10^{-3}\,\mathrm{V/m\,Hz^{-1/4}}$	$10^{-4}\,\mathrm{V/m\,Hz^{-1/4}}$	$10^{-4}\,\mathrm{V/m\,Hz^{-1/4}}$
V Noise at 100 kHz	$10^{-6}\,\mathrm{V/Hz^{-1/4}}$	$3 \times 10^{-7}\,\mathrm{V/Hz^{-1/4}}$	$2 \times 10^{-7}\,\mathrm{V/Hz^{-1/4}}$

Table 2. Solar Wind Parameters for Modeling.

Case	U_0	n_{SW}	B_0	θ_{bu}	M_A	β_p	β_e
a	200 km/s	10^4	6250 nT	11°	1.2	0.1	0.000125
b	200 km/s	10^4	6250 nT	11°	1.2	0.1	0.025
c	200 km/s	10^4	6250 nT	45°	2.0	0.1	0.000125

Table 3. Electromagnetic Field Perturbation in Plasma Environment near SP^{+}.

Case	$t(T_{ce})$	$\delta E_x(1.24\,\mathrm{V/m})$	$\delta E_y(1.24\,\mathrm{V/m})$	$\delta E_z(1.24\,\mathrm{V/m})$	$\delta B_x(6250\,\mathrm{nT})$	$\delta B_y(6250\,\mathrm{nT})$	$\delta B_z(6250\,\mathrm{nT})$	E_n at bus
a	0.014	0.005-0.01	0.01-0.5	0.05-0.1	0.001	0.0002	0.001	1000
a	0.29	0.005-0.01	0.05-1.0	0.05-0.2	0.005	0.01	0.1	1200
b	0.014	0.002-0.01	0.05	0.05	0.001	0.0002	0.001	30
b	0.03	0.02-0.04	0.05	0.02-0.2	0.005	0.01	0.04	30
c	13.6	0.2-0.5	0.25-0.5	0.2-2.5	0.05-1	0.05-2	0.05- 1.4	5.0

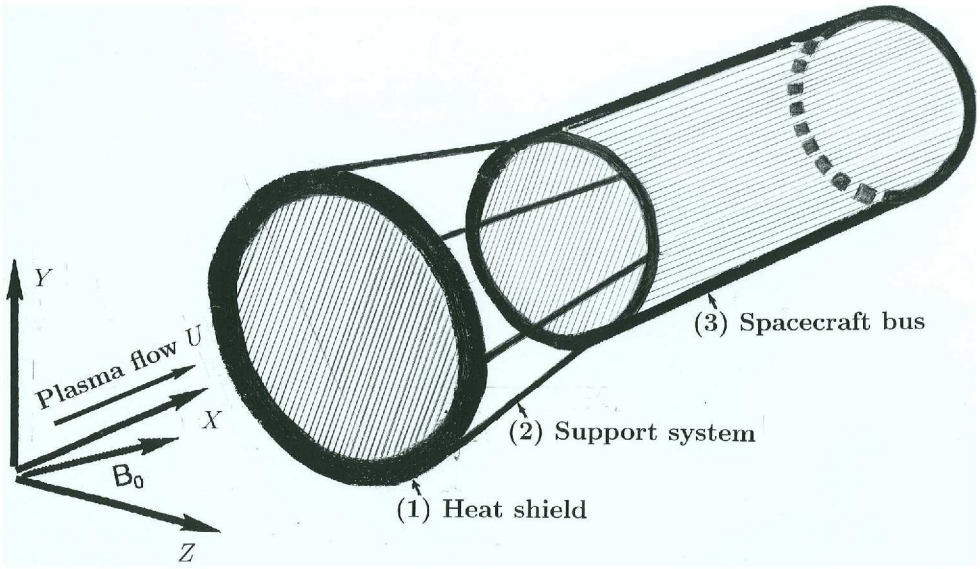

Figure 1. Scheme of the interaction of the solar wind with SP+. The spiral magnetic field is inside the x-z plane. (1) a heat shield; (2) a support system; (3) a spacecraft bus.

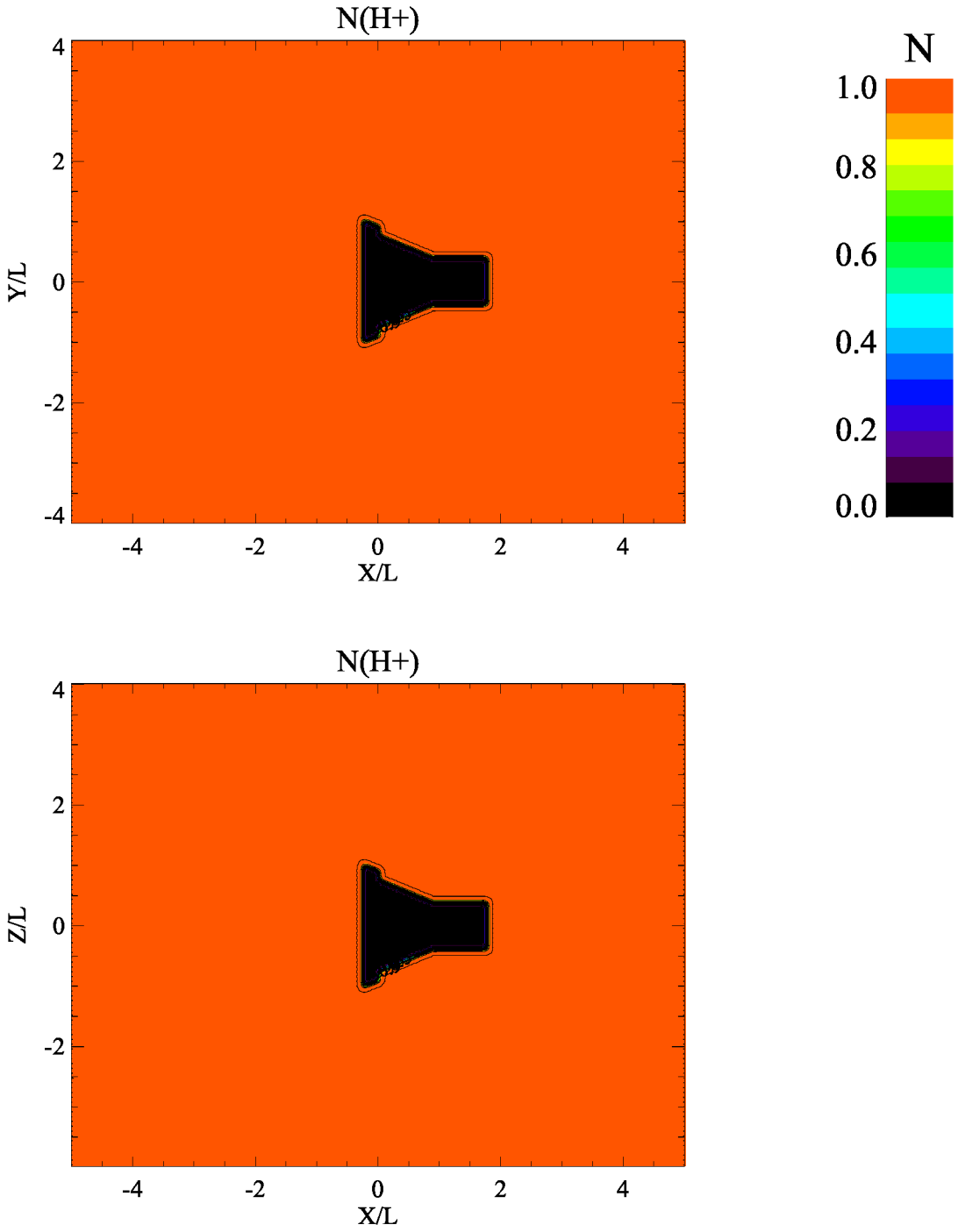

Figure 2. Solar wind ion density in the y-x ($z = 0$) and z-x ($y = 0$) planes. $U_0 = 200\,\mathrm{km/s}$, $M_A = 1.5$, $B_0 = 6250\,\mathrm{nT}$, $E_0 = U_0 B_0 = 1.24\mathrm{V/m}$, $n_{SW} = 10^4\,\mathrm{cm}^{-3}$, $\beta_\mathrm{p} = 0.1$, $\beta_\mathrm{e} = 0.000125$, $\theta_{bu} = 11^o$. Linear perturbations at the beginning of simulation $t = 0.014\,T_{ce}$

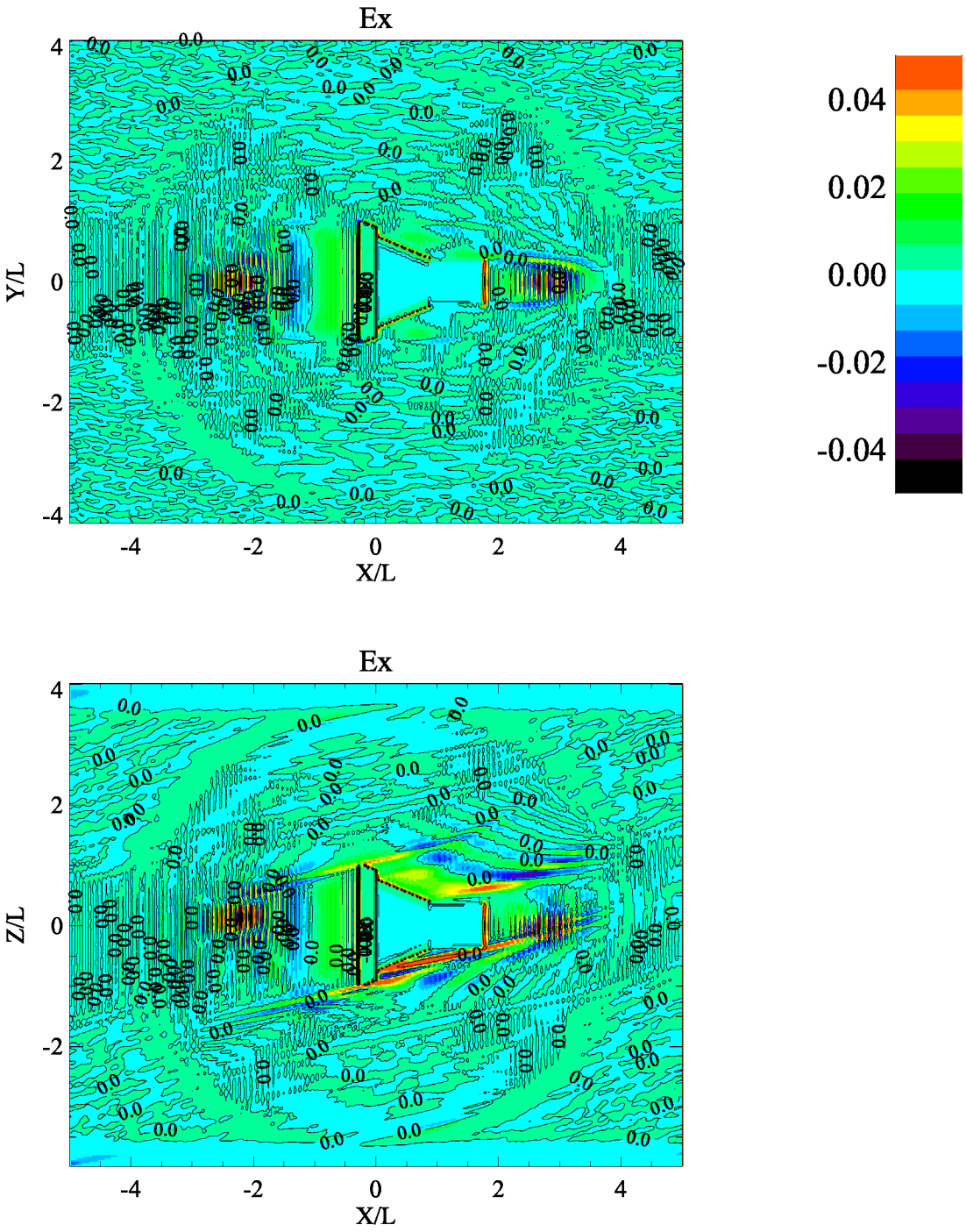

Figure 3. Electric field component $E_x(1.24\,\mathrm{V/m})$ in the y-x ($z = 0$) and z-x ($y = 0$) planes. $U_0 = 200\,\mathrm{km/s}$, $M_A = 1.5$, $B_0 = 6250\,\mathrm{nT}$, $n_{SW} = 10^4\,\mathrm{cm}^{-3}$, $\beta_\mathrm{p} = 0.1$, $\beta_\mathrm{e} = 0.000125$, $\theta_{bu} = 11^o$. Linear perturbations at the beginning of simulation $t = 0.014\,T_{ce}$

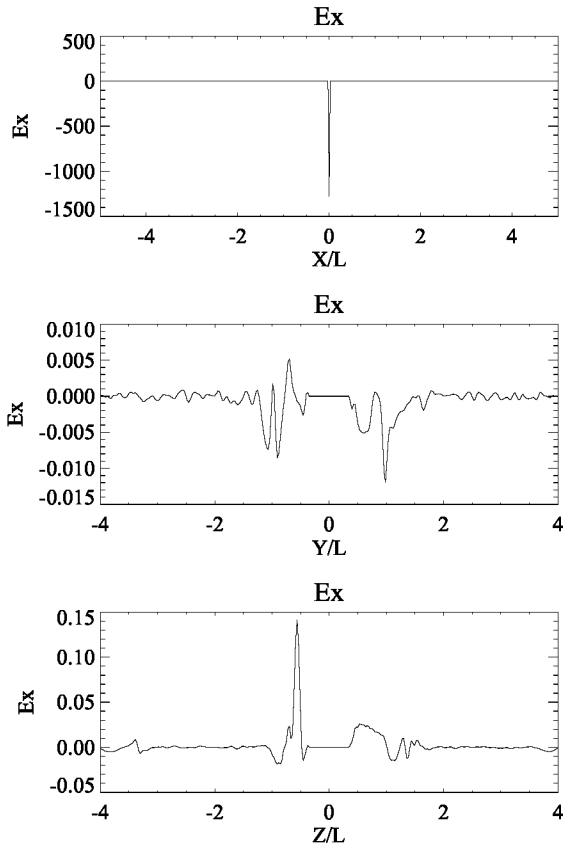

Figure 4. 1-D cuts for the electric field component $E_x(1.24\,\mathrm{V/m})$ (top: $y = 0$, $z = 0$; middle: $x = 1.5$, $z = 0$; bottom: $x = 1.5$, $y = 0$). $U_0 = 200\,\mathrm{km/s}$, $M_A = 1.5$, $B_0 = 6250\,\mathrm{nT}$, $n_{SW} = 10^4\,\mathrm{cm}^{-3}$, $\beta_\mathrm{p} = 0.1$, $\beta_\mathrm{e} = 0.000125$, $\theta_{bu} = 11^o$. Linear perturbations at the beginning of simulation $t = 0.014T_{ce}$

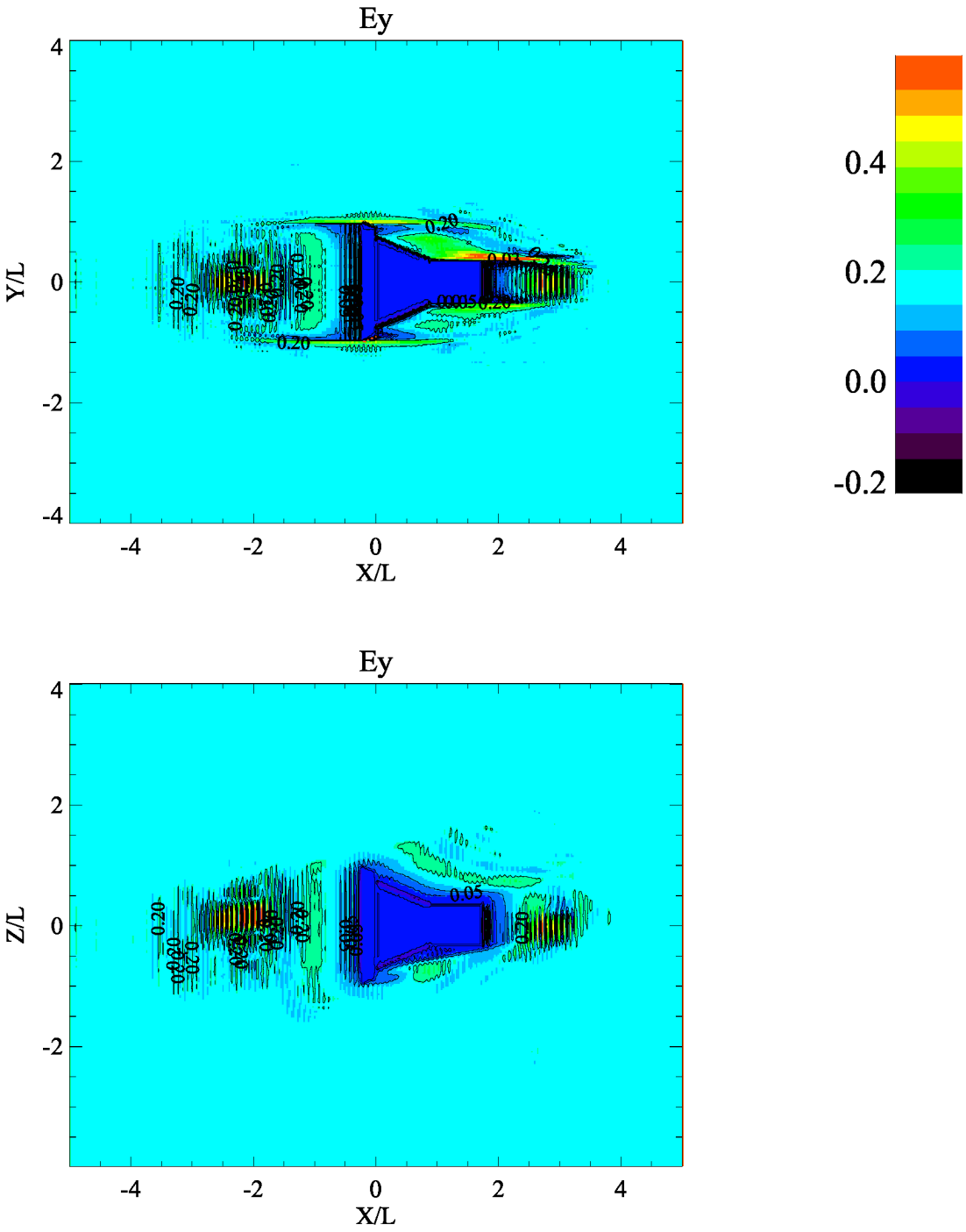

Figure 5. Electric field component $E_y(1.24\,\mathrm{V/m})$ in the y-x ($z = 0$) and z-x ($y = 0$) planes. $U_0 = 200\,\mathrm{km/s}$, $M_A = 1.5$, $B_0 = 6250\,\mathrm{nT}$, $n_{SW} = 10^4\,\mathrm{cm}^{-3}$, $\beta_\mathrm{p} = 0.1$, $\beta_\mathrm{e} = 0.000125$, $\theta_{bu} = 11^o$. Linear perturbations at the beginning of simulation $t = 0.014\,T_{ce}$

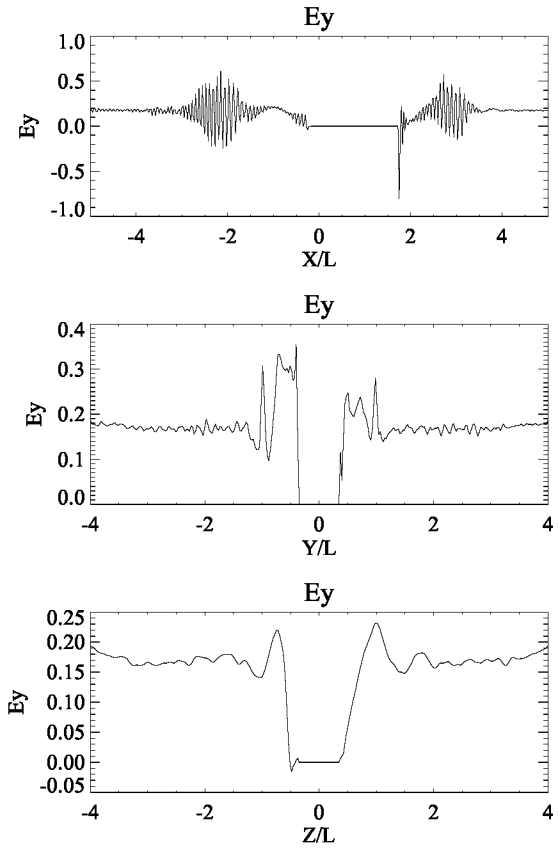

Figure 6. 1-D cuts for the electric field component $E_y(1.24\,\mathrm{V/m})$ (top: $y = 0$, $z = 0$; middle: $x = 1.5$, $z = 0$; bottom: $x = 1.5$, $y = 0$). $U_0 = 200\,\mathrm{km/s}$, $M_A = 1.5$, $B_0 = 6250\,\mathrm{nT}$, $n_{SW} = 10^4\,\mathrm{cm}^{-3}$, $\beta_\mathrm{p} = 0.1$, $\beta_\mathrm{e} = 0.000125$, $\theta_{bu} = 11^o$. Linear perturbations at the beginning of simulation $t = 0.014\,T_{ce}$

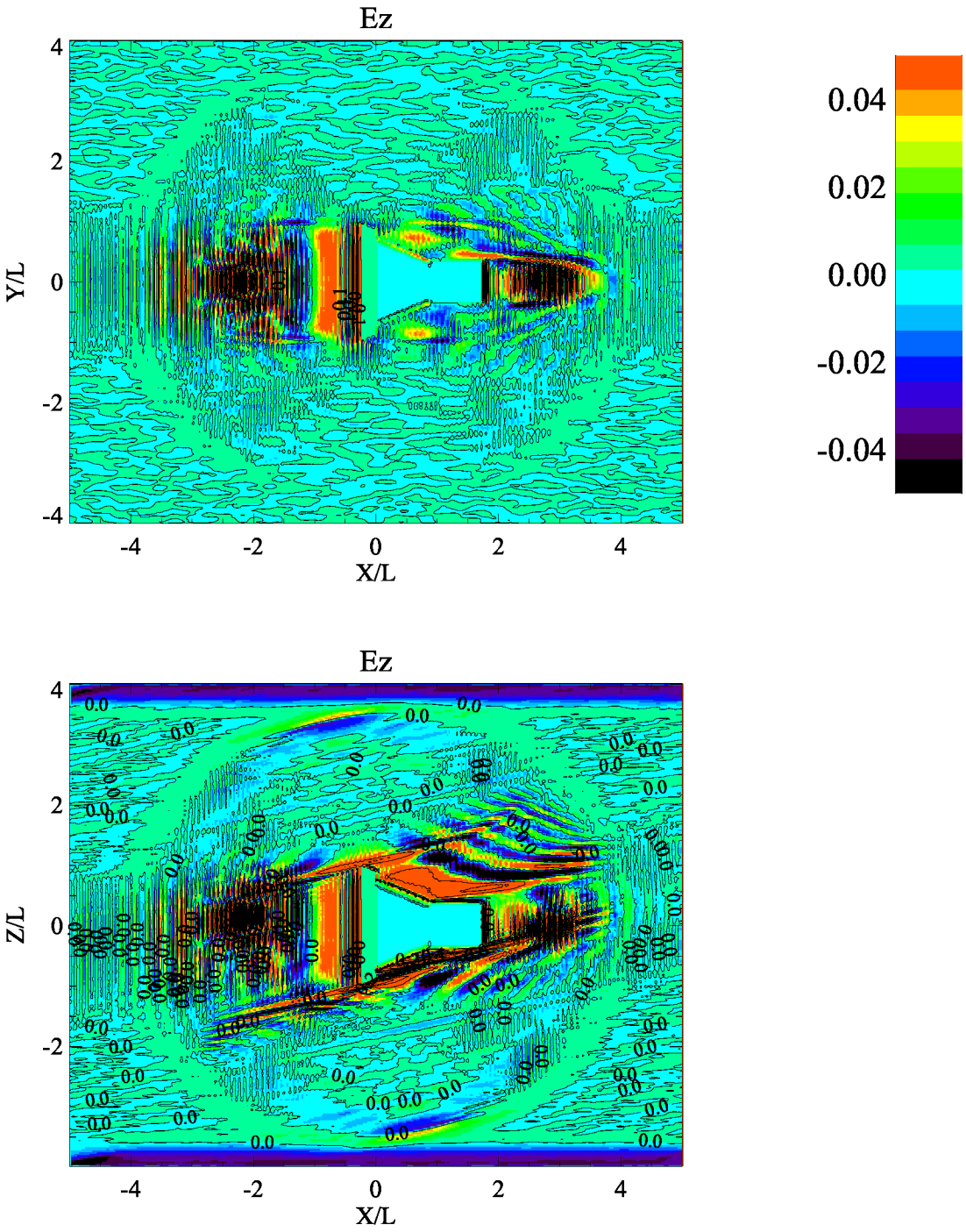

Figure 7. Electric field component $E_z(1.24\,/\mathrm{m})$ in the y-x ($z = 0$) and z-x ($y = 0$) planes. $U_0 = 200\,\mathrm{km/s}$, $M_A = 1.5$, $B_0 = 6250\,\mathrm{nT}$, $n_{SW} = 10^4\,\mathrm{cm}^{-3}$, $\beta_\mathrm{p} = 0.1$, $\beta_\mathrm{e} = 0.000125$, $\theta_{bu} = 11^o$. Linear perturbations at the beginning of simulation $t = 0.014\,T_{ce}$

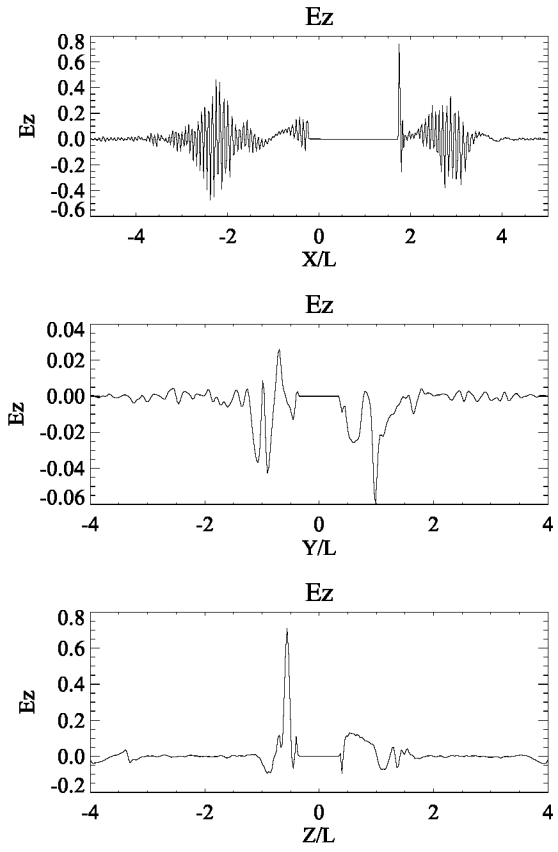

Figure 8. 1-D cuts for the electric field component $E_z(1.24\,\mathrm{V/m})$ (top: $y = 0$, $z = 0$; middle: $x = 1.5$, $z = 0$; bottom: $x = 1.5$, $y = 0$). $U_0 = 200\,\mathrm{km/s}$, $M_A = 1.5$, $B_0 = 6250\,\mathrm{nT}$, $n_{SW} = 10^4\,\mathrm{cm}^{-3}$, $\beta_\mathrm{p} = 0.1$, $\beta_\mathrm{e} = 0.000125$, $\theta_{bu} = 11^o$. Linear perturbations at the beginning of simulation $t = 0.014\,T_{ce}$

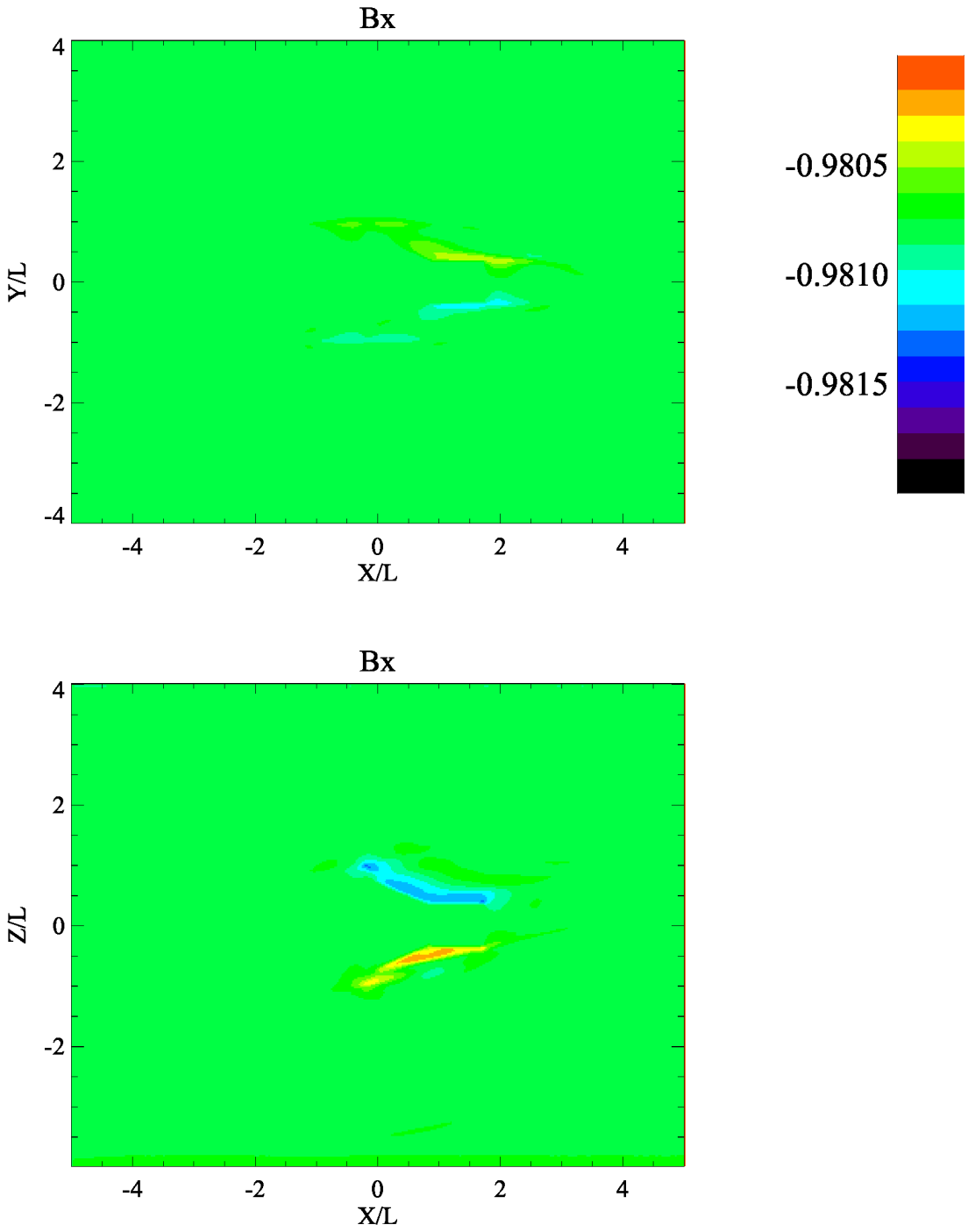

Figure 9. Magnetic field component $B_x(6250\,\mathrm{nT})$ in the y-x ($z = 0$) and z-x ($y = 0$) planes. $U_0 = 200\,\mathrm{km/s}$, $M_A = 1.5$, $B_0 = 6250\,\mathrm{nT}$, $n_{SW} = 10^4\,\mathrm{cm}^{-3}$, $\beta_\mathrm{p} = 0.1$, $\beta_\mathrm{e} = 0.000125$, $\theta_{bu} = 11^o$. Linear perturbations at the beginning of simulation $t = 0.014\,T_{ce}$

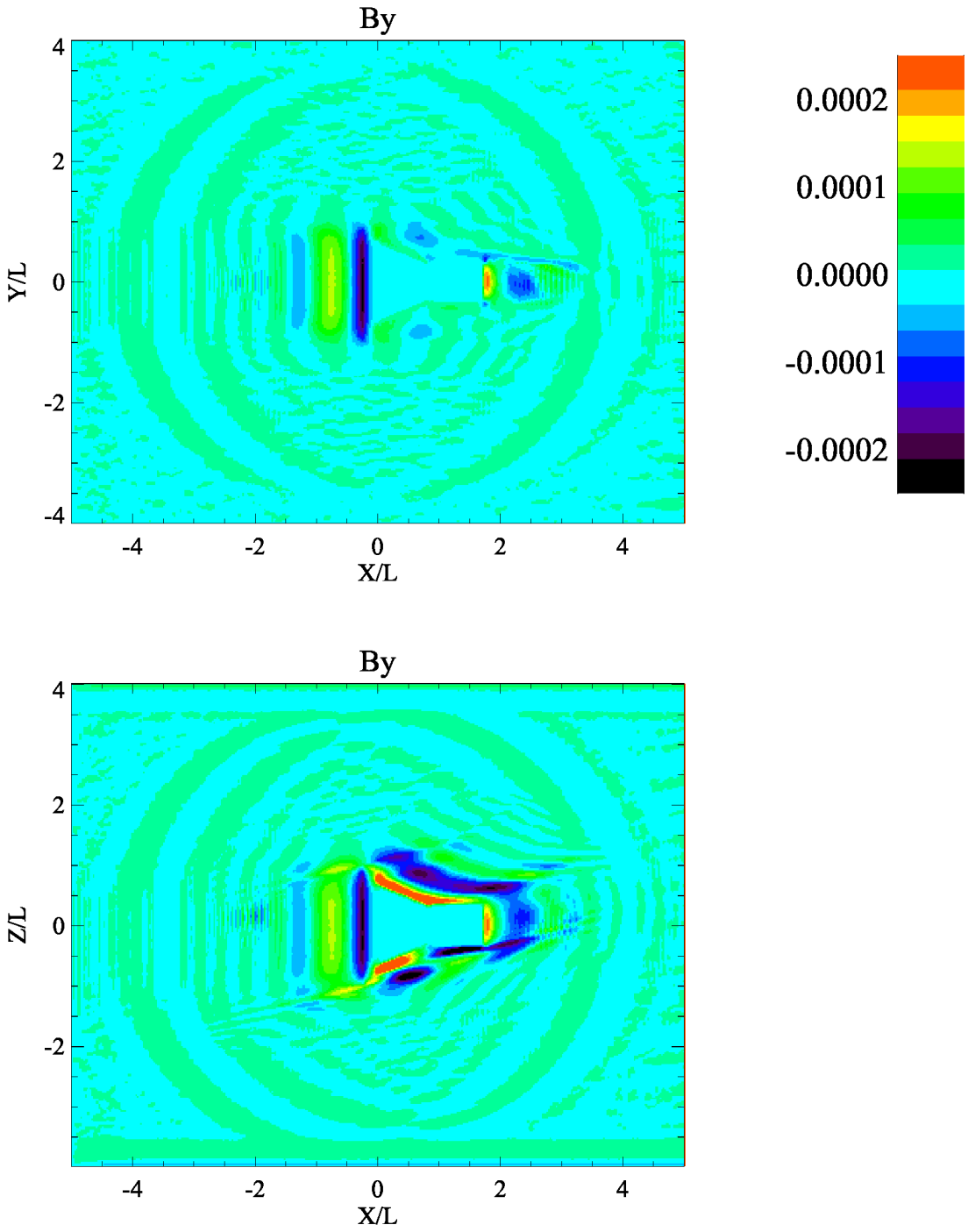

Figure 10. Magnetic field component $B_y(6250\,\mathrm{nT})$ in the y-x ($z = 0$) and z-x ($y = 0$) planes. $U_0 = 200\,\mathrm{km/s}$, $M_A = 1.5$, $B_0 = 6250\,\mathrm{nT}$, $n_{SW} = 10^4\,\mathrm{cm}^{-3}$, $\beta_\mathrm{p} = 0.1$, $\beta_\mathrm{e} = 0.000125$, $\theta_{bu} = 11^o$. Linear perturbations at the beginning of simulation $t = 0.014\,T_{ce}$

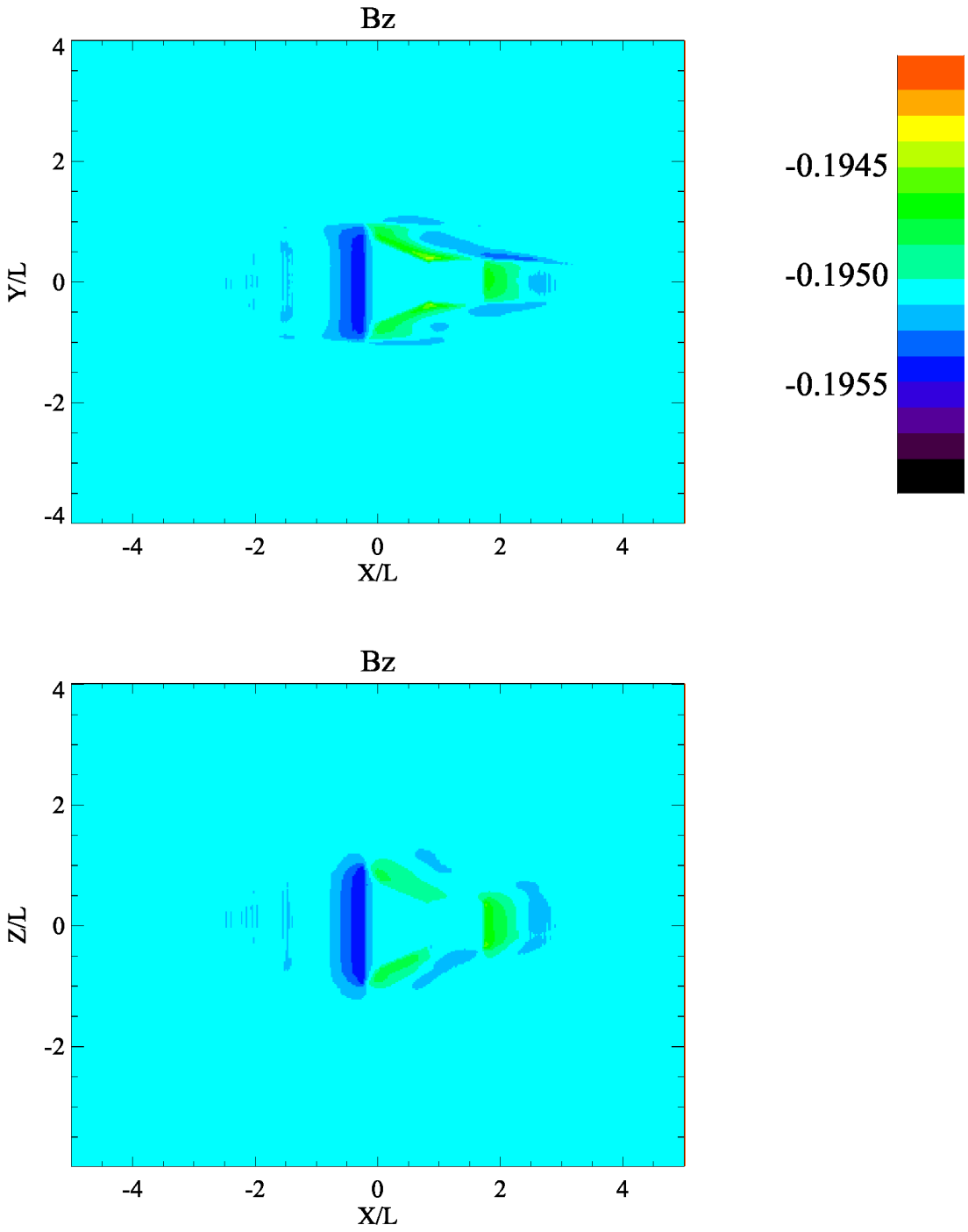

Figure 11. Magnetic field component $B_z(6250\,\mathrm{nT})$ in the y-x ($z = 0$) and z-x ($y = 0$) planes. $U_0 = 200\,\mathrm{km/s}$, $M_A = 1.5$, $B_0 = 6250\,\mathrm{nT}$, $n_{SW} = 10^4\,\mathrm{cm}^{-3}$, $\beta_\mathrm{p} = 0.1$, $\beta_\mathrm{e} = 0.000125$, $\theta_{bu} = 11^o$. Linear perturbations at the beginning of simulation $t = 0.014\,T_{ce}$

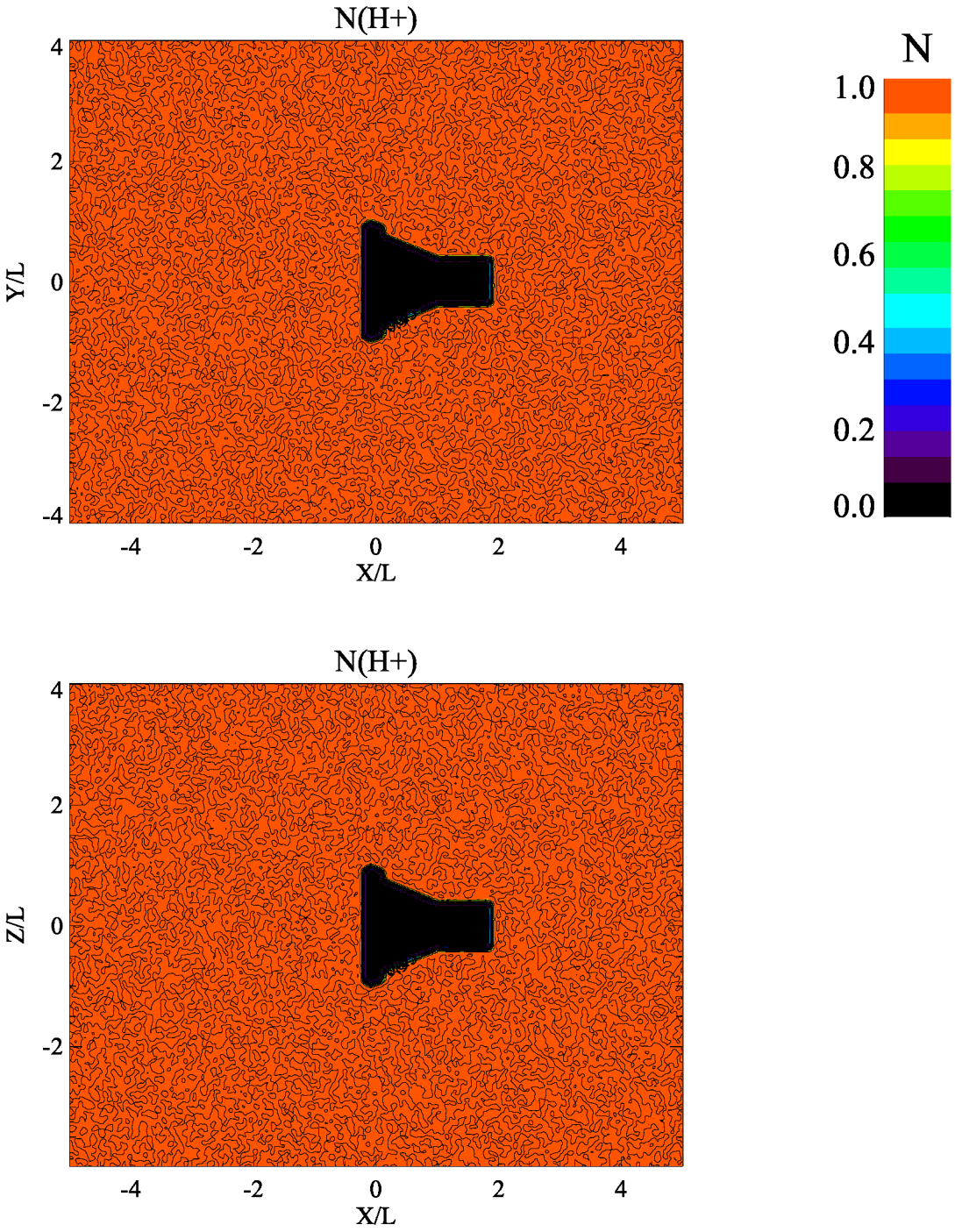

Figure 12. Solar wind ion density in the y-x ($z = 0$) and z-x ($y = 0$) planes. $U_0 = 200\,\mathrm{km/s}$, $M_A = 1.5$, $B_0 = 6250\,\mathrm{nT}$, $E_0 = U_0 B_0 = 1.24\mathrm{V/m}$, $n_{SW} = 10^4\,\mathrm{cm}^{-3}$, $\beta_\mathrm{p} = 0.1$, $\beta_\mathrm{e} = 0.000125$, $\theta_{bu} = 11^o$. Nonlinear saturation of the perturbations at $t = 0.29\,T_{ce}(0.04\,T_{transit})$

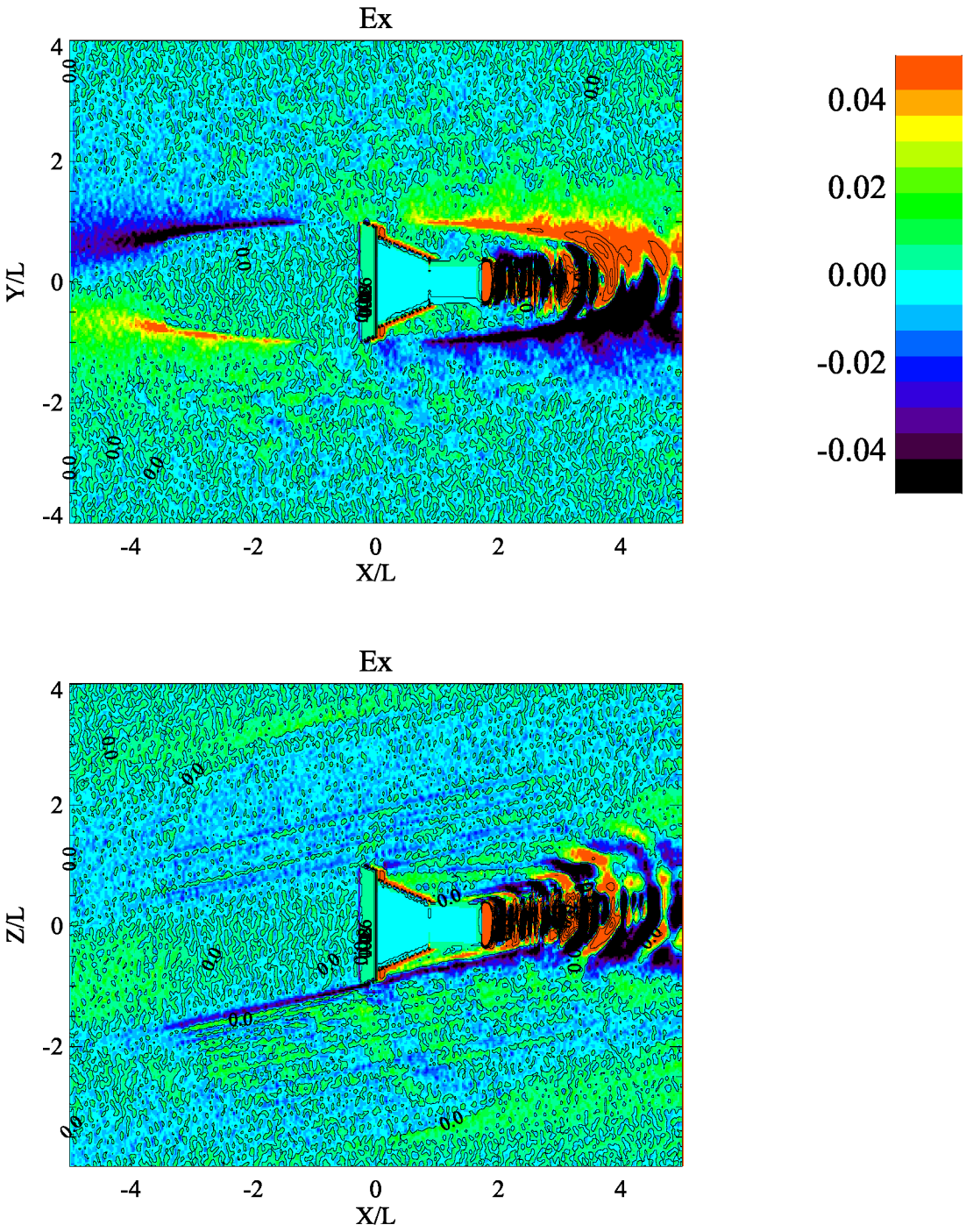

Figure 13. Electric field component $E_x(1.24\,\mathrm{V/m})$ in the y-x ($z = 0$) and z-x ($y = 0$) planes. $U_0 = 200\,\mathrm{km/s}$, $M_A = 1.5$, $B_0 = 6250\,\mathrm{nT}$, $n_{SW} = 10^4\,\mathrm{cm}^{-3}$, $\beta_\mathrm{p} = 0.1$, $\beta_\mathrm{e} = 0.000125$, $\theta_{bu} = 11^o$. Nonlinear saturation of the perturbations at $t = 0.29\,T_{ce}(0.04\,T_{transit})$

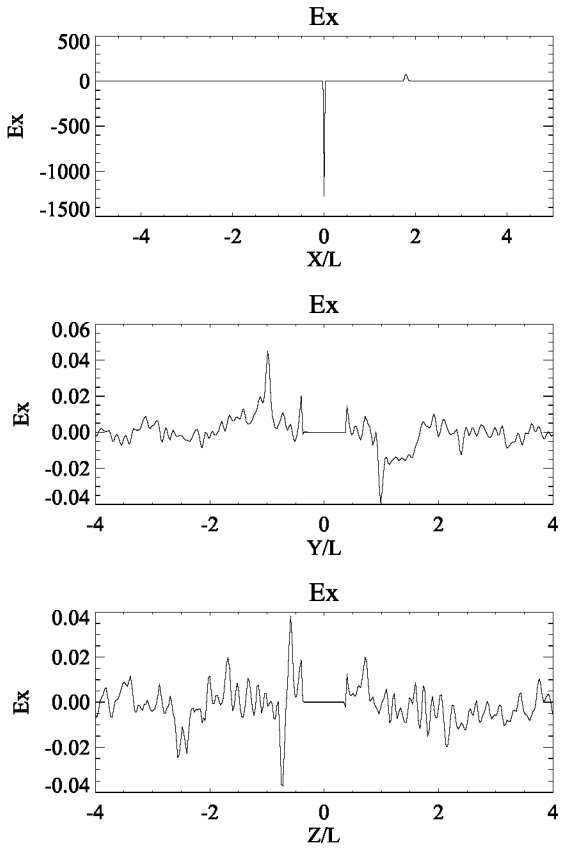

Figure 14. 1-D cuts for the electric field component $E_x(1.24\,\mathrm{V/m})$ (top: $y = 0$, $z = 0$; middle: $x = 1.5$, $z = 0$; bottom: $x = 1.5$, $y = 0$). $U_0 = 200\,\mathrm{km/s}$, $M_A = 1.5$, $B_0 = 6250\,\mathrm{nT}$, $n = 10^4\,\mathrm{cm}^{-3}$, $\beta_\mathrm{p} = 0.1$, $\beta_\mathrm{e} = 0.000125$, $\theta_{bu} = 11^o$. Nonlinear saturation of the perturbations at $t = 0.29\,T_{ce}(0.04\,T_{transit})$

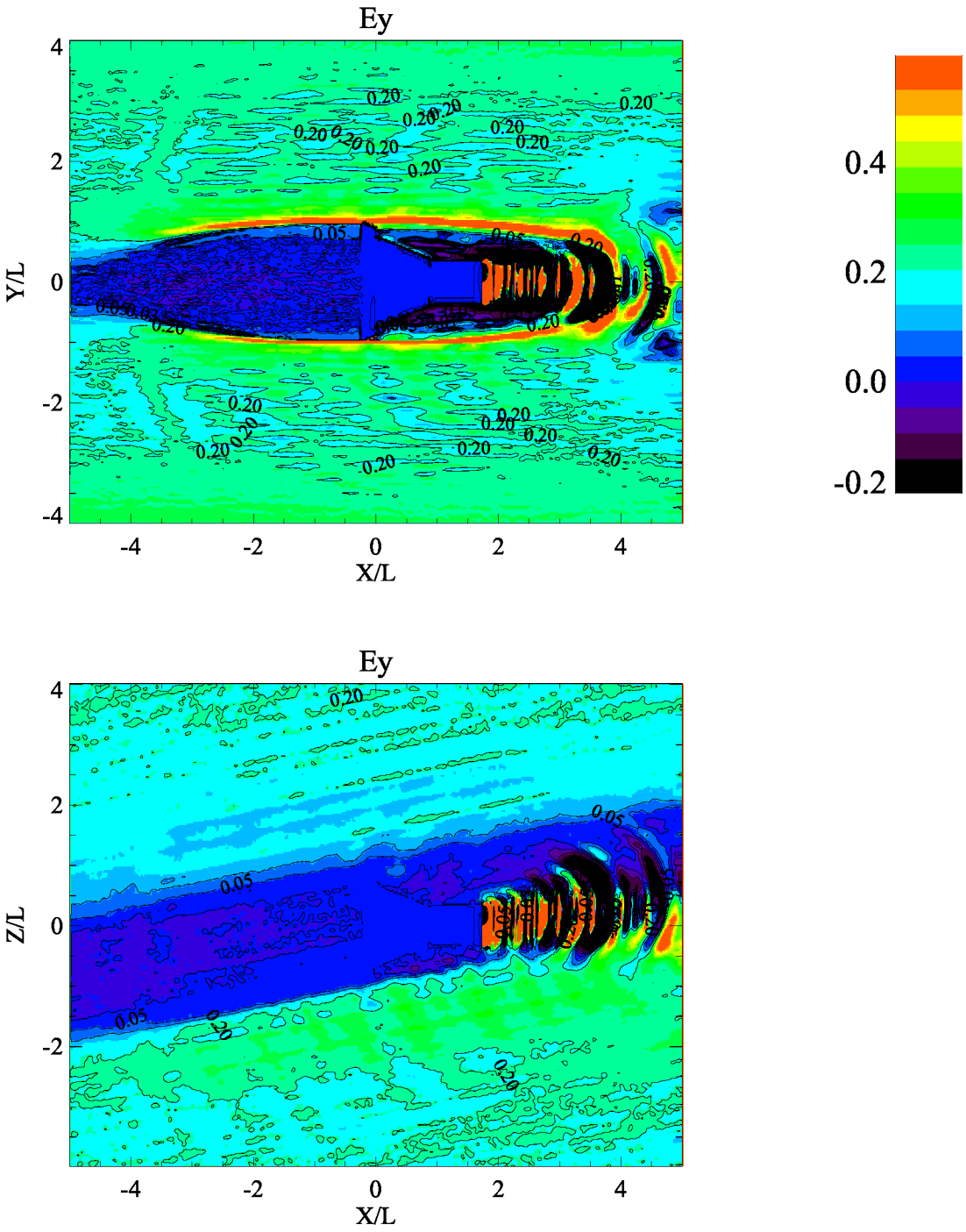

Figure 15. Electric field component $E_y(1.24\,\mathrm{V/m})$ in the y-x ($z = 0$) and z-x ($y = 0$) planes. $U_0 = 200\,\mathrm{km/s}$, $M_A = 1.5$, $B_0 = 6250\,\mathrm{nT}$, $n_{SW} = 10^4\,\mathrm{cm}^{-3}$, $\beta_\mathrm{p} = 0.1$, $\beta_\mathrm{e} = 0.000125$, $\theta_{bu} = 11^o$. Nonlinear saturation of the perturbations at $t = 0.29\,T_{ce}(0.04\,T_{transit})$

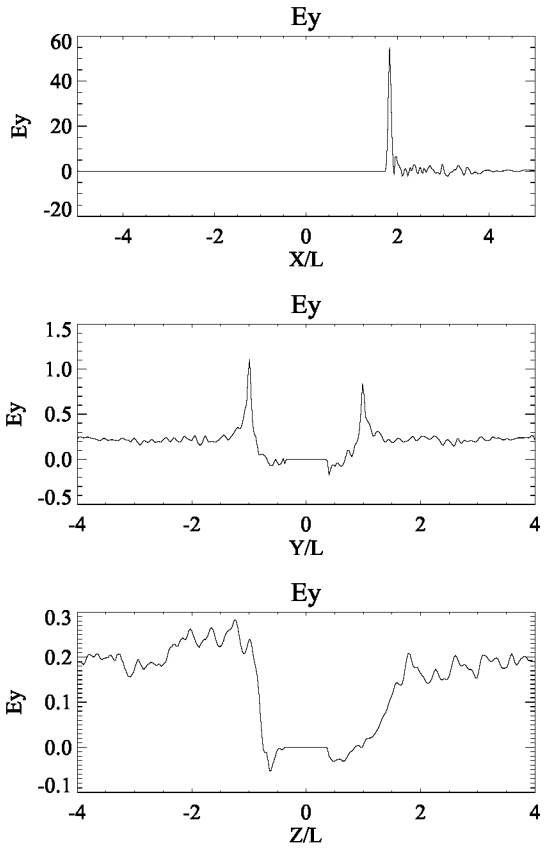

Figure 16. 1-D cuts for the electric field component $E_y(1.24\,\mathrm{V/m})$ (top: $y = 0$, $z = 0$; middle: $x = 1.5$, $z = 0$; bottom: $x = 1.5$, $y = 0$). $U_0 = 200\,\mathrm{km/s}$, $M_A = 1.5$, $B_0 = 6250\,\mathrm{nT}$, $n_{SW} = 10^4\,\mathrm{cm}^{-3}$, $\beta_\mathrm{p} = 0.1$, $\beta_\mathrm{e} = 0.000125$, $\theta_{bu} = 11^o$. Nonlinear saturation of the perturbations at $t = 0.29\,T_{ce}(0.04\,T_{transit})$

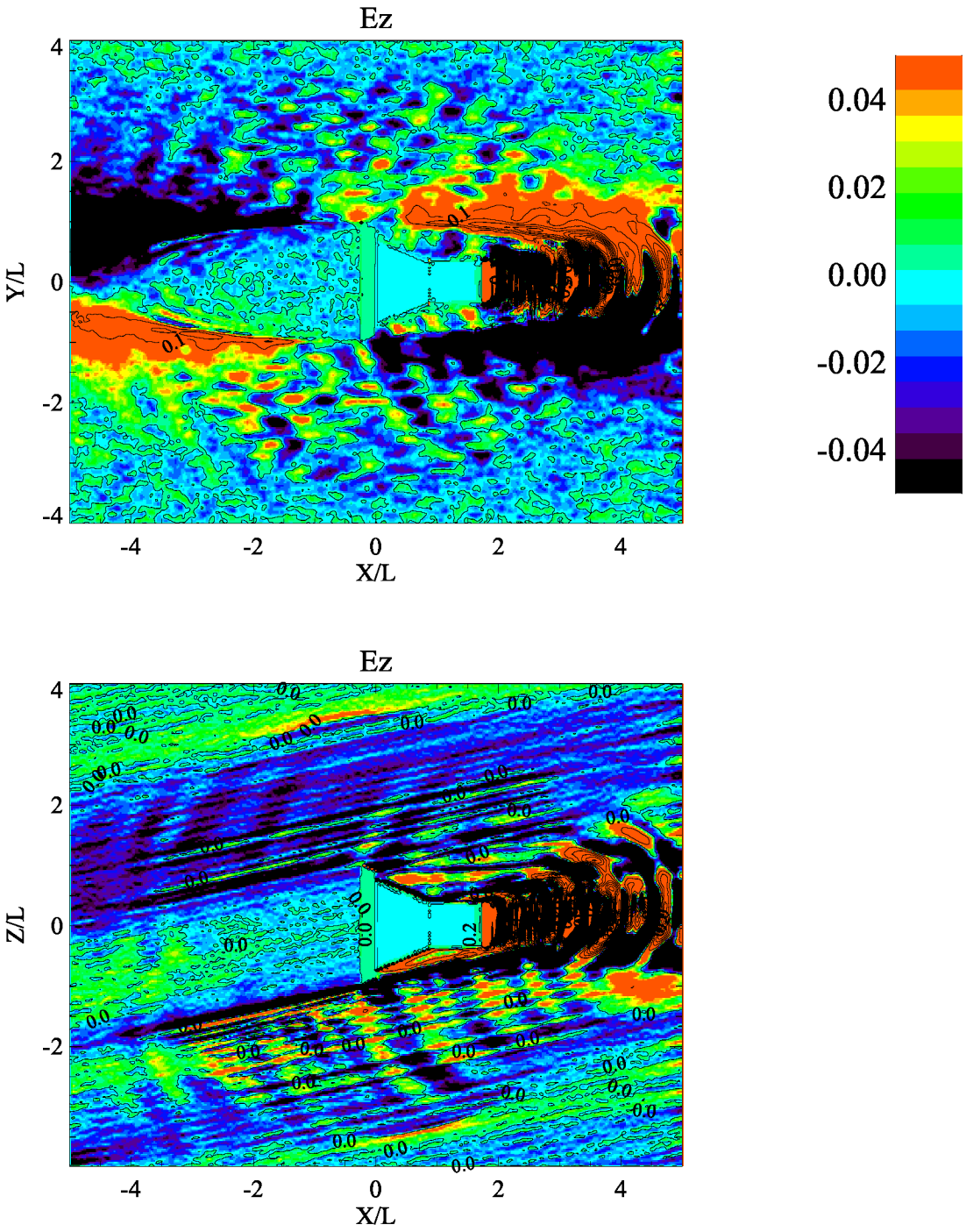

Figure 17. Electric field component $E_z(1.24\,\mathrm{V/m})$ in the y-x ($z = 0$) and z-x ($y = 0$) planes. $U_0 = 200\,\mathrm{km/s}$, $M_A = 1.5$, $B_0 = 6250\,\mathrm{nT}$, $n_{SW} = 10^4\,\mathrm{cm}^{-3}$, $\beta_\mathrm{p} = 0.1$, $\beta_\mathrm{e} = 0.000125$, $\theta_{bu} = 11^o$. Nonlinear saturation of the perturbations at $t = 0.29\,T_{ce}(0.04\,T_{transit})$

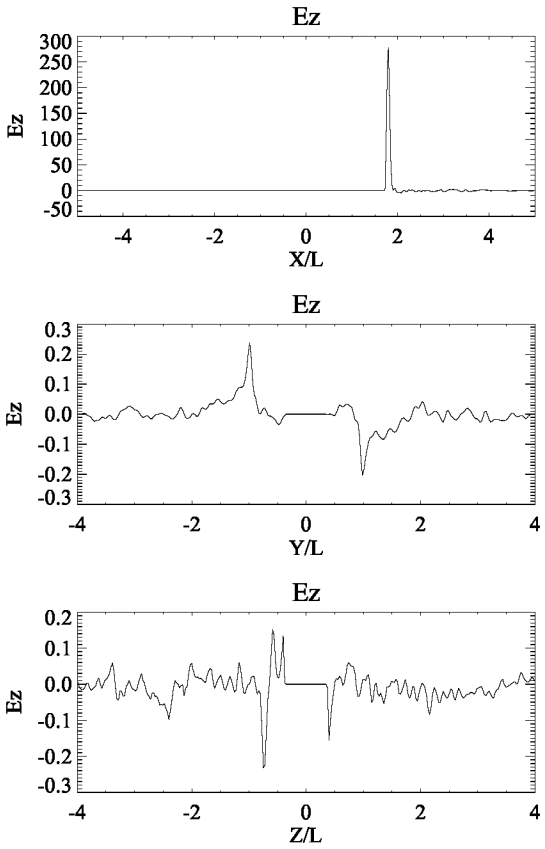

Figure 18. 1-D cuts for the electric field component $E_z(1.24\,\mathrm{V/m})$ (top: $y = 0$, $z = 0$; middle: $x = 1.5$, $z = 0$; bottom: $x = 1.5$, $y = 0$). $U_0 = 200\,\mathrm{km/s}$, $M_A = 1.5$, $B_0 = 6250\,\mathrm{nT}$, $n_{SW} = 10^4\,\mathrm{cm}^{-3}$, $\beta_\mathrm{p} = 0.1$, $\beta_\mathrm{e} = 0.000125$, $\theta_{bu} = 11^o$. Nonlinear saturation of the perturbations at $t = 0.29\,T_{ce}(0.04\,T_{transit})$

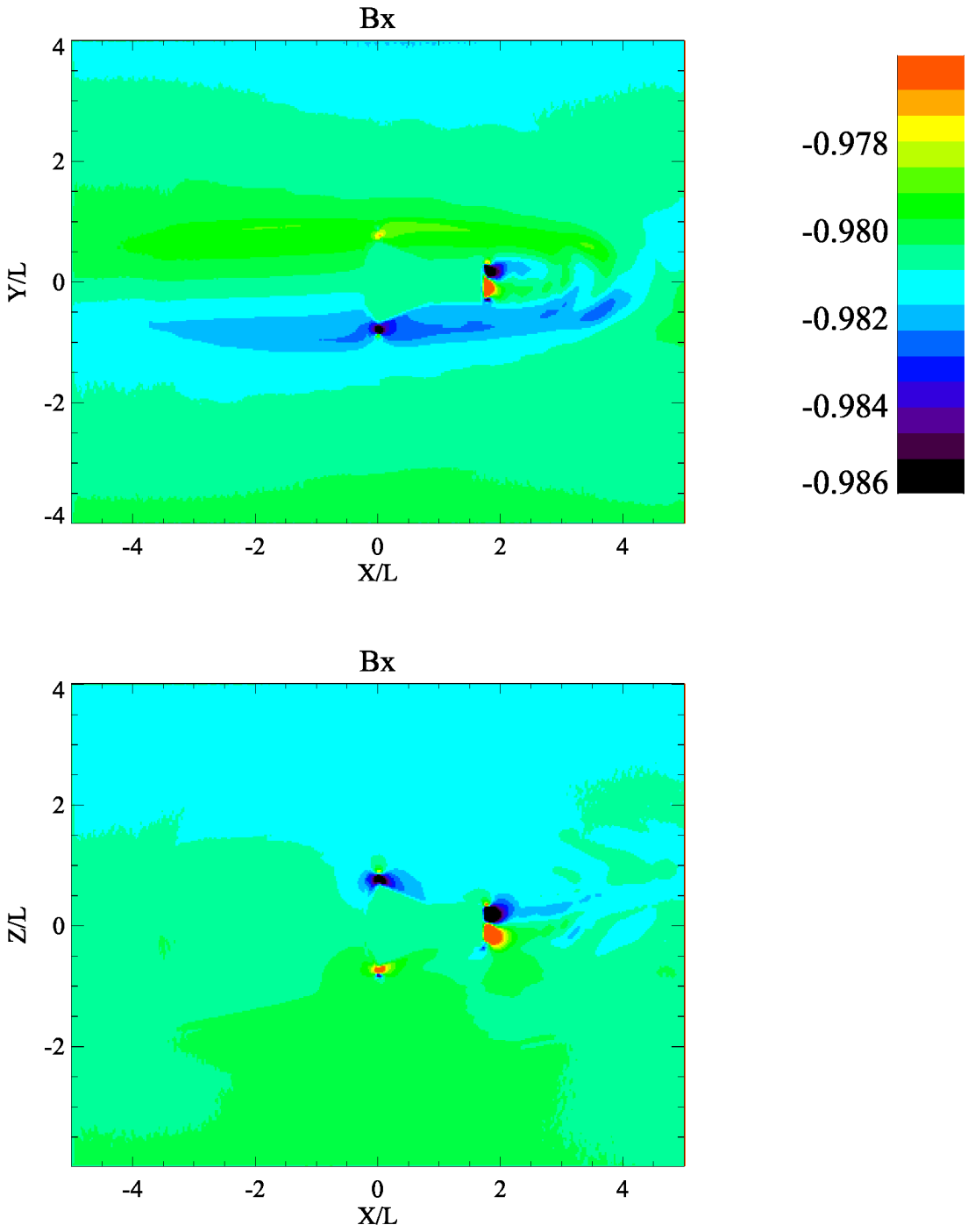

Figure 19. Magnetic field component $B_x(6250\,\mathrm{nT})$ in the y-x ($z = 0$) and z-x ($y = 0$) planes. $U_0 = 200\,\mathrm{km/s}$, $M_A = 1.5$, $B_0 = 6250\,\mathrm{nT}$, $n_{SW} = 10^4\,\mathrm{cm}^{-3}$, $\beta_\mathrm{p} = 0.1$, $\beta_\mathrm{e} = 0.000125$, $\theta_{bu} = 11^o$. Nonlinear saturation of the perturbations at $t = 0.29\,T_{ce}(0.04\,T_{transit})$

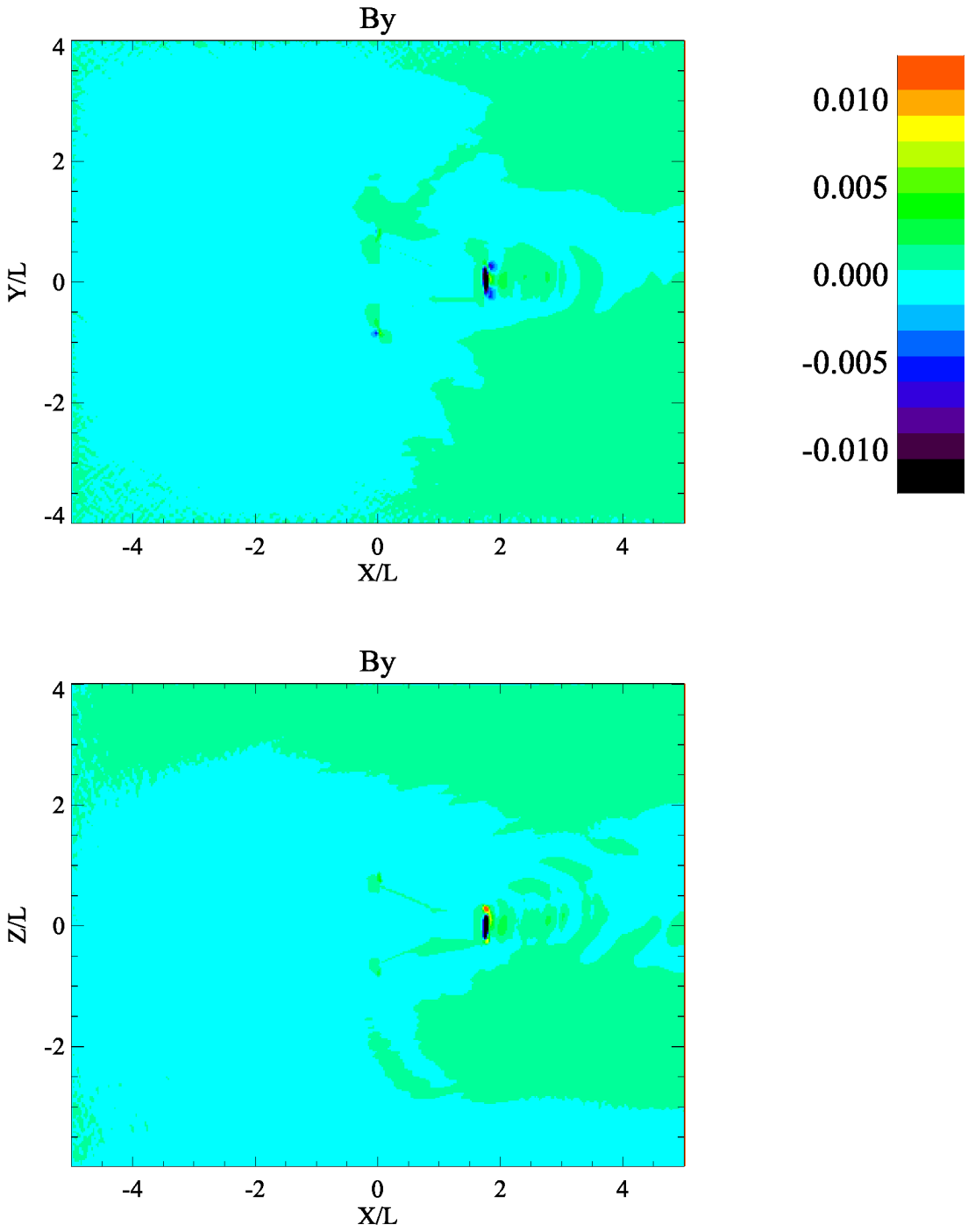

Figure 20. Magnetic field component $B_y(6250\,\mathrm{nT})$ in the y-x ($z = 0$) and z-x ($y = 0$) planes. $U_0 = 200\,\mathrm{km/s}$, $M_A = 1.5$, $B_0 = 6250\,\mathrm{nT}$, $n_{SW} = 10^4\,\mathrm{cm}^{-3}$, $\beta_\mathrm{p} = 0.1$, $\beta_\mathrm{e} = 0.000125$, $\theta_{bu} = 11^o$. Nonlinear saturation of the perturbations at $t = 0.29\,T_{ce}(0.04\,T_{transit})$

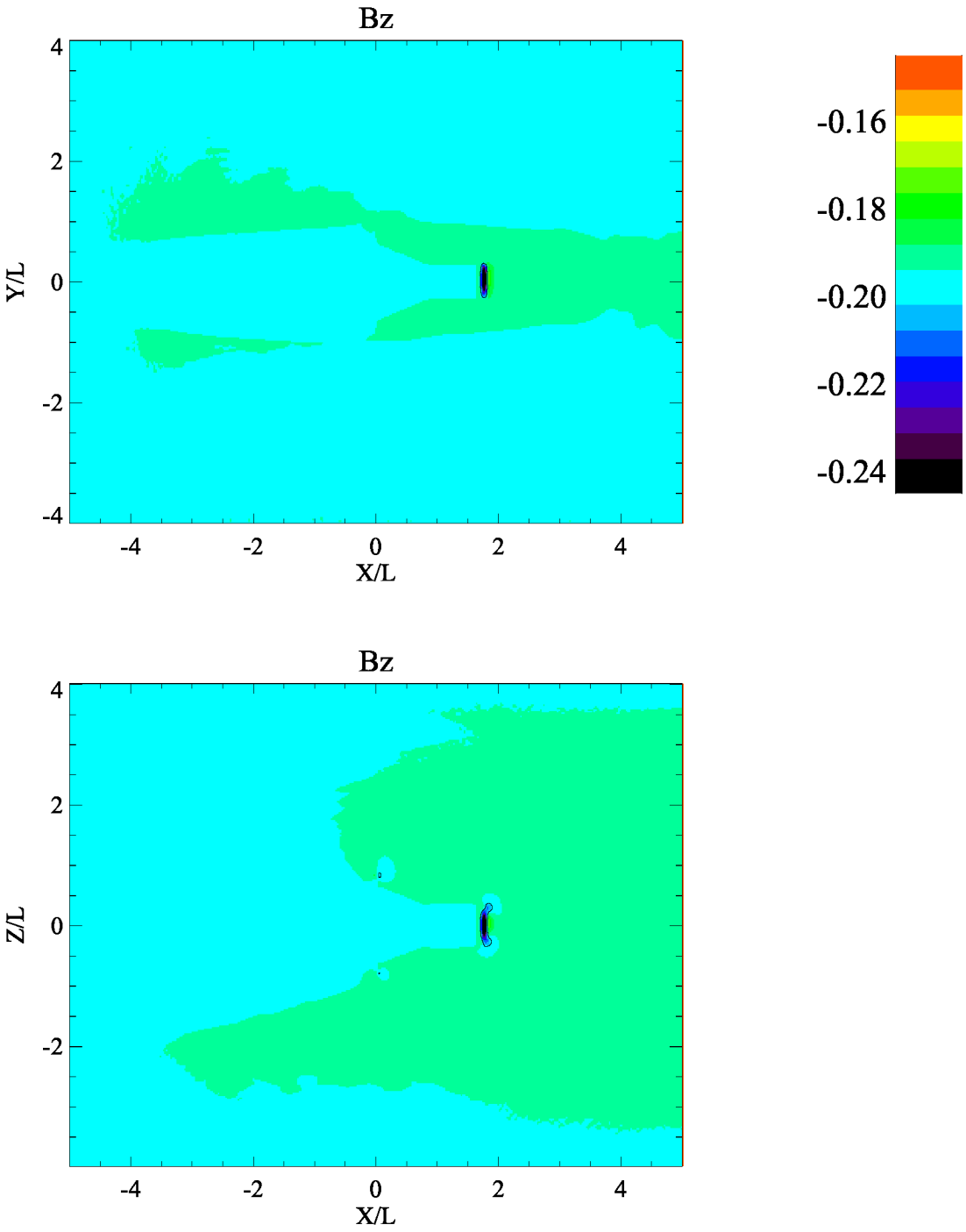

Figure 21. Magnetic field component $B_z(6250\,\mathrm{nT})$ in the y-x ($z = 0$) and z-x ($y = 0$) planes. $U_0 = 200\,\mathrm{km/s}$, $M_A = 1.5$, $B_0 = 6250\,\mathrm{nT}$, $n_{SW} = 10^4\,\mathrm{cm}^{-3}$, $\beta_\mathrm{p} = 0.1$, $\beta_\mathrm{e} = 0.000125$, $\theta_{bu} = 11^o$. Nonlinear saturation of the perturbations at $t = 0.29\,T_{ce}(0.04\,T_{transit})$

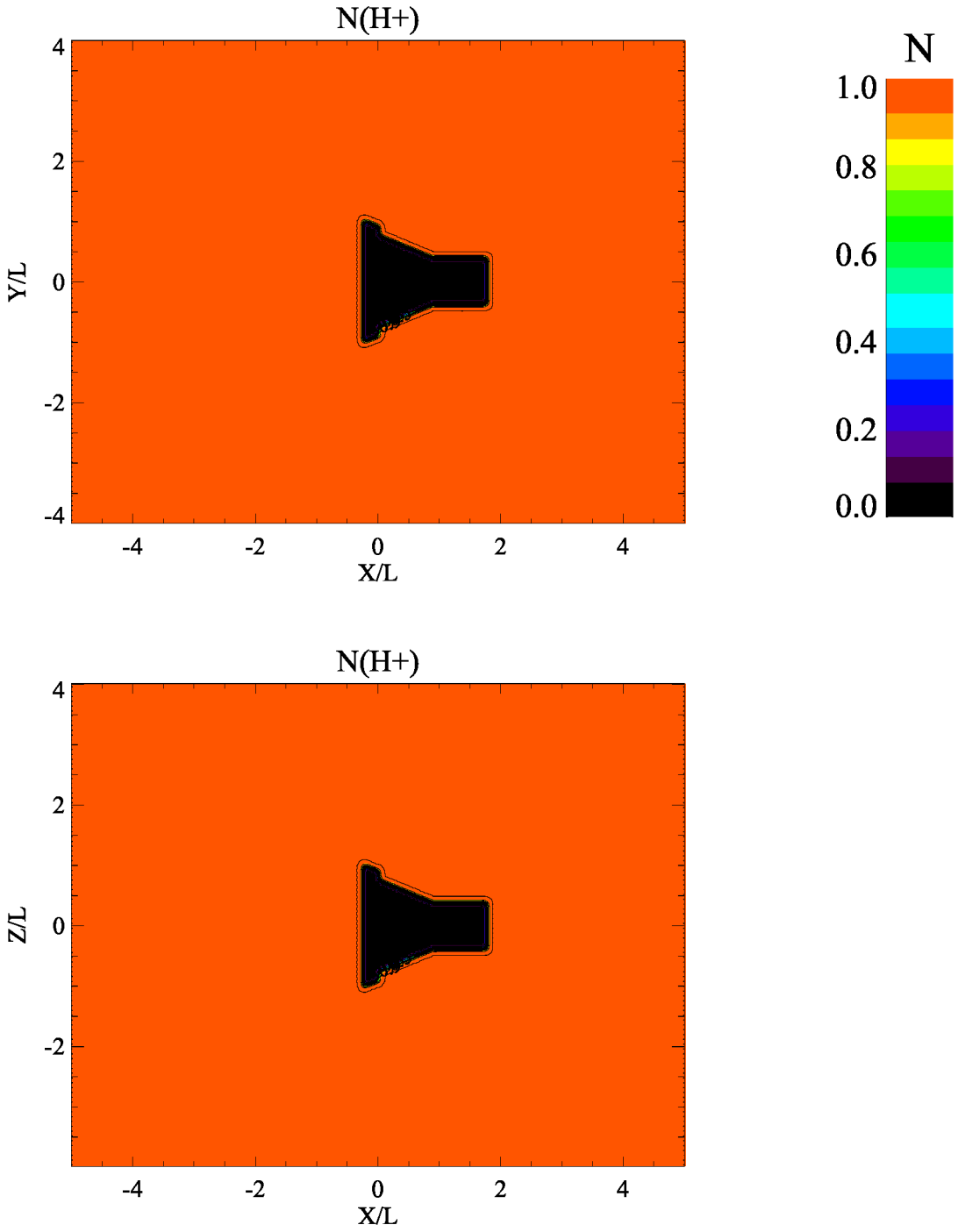

Figure 22. Solar wind ion density in the y-x ($z = 0$) and z-x ($y = 0$) planes. $U_0 = 200\,\mathrm{km/s}$, $M_A = 1.5$, $B_0 = 6250\,\mathrm{nT}$, $E_0 = U_0 B_0 = 1.24\mathrm{V/m}$, $n_{SW} = 10^4\,\mathrm{cm}^{-3}$, $\beta_\mathrm{p} = 0.1$, $\beta_\mathrm{e} = 0.025$, $\theta_{bu} = 11^o$. Linear perturbations at the beginning of simulation $t = 0.014\,T_{ce}$

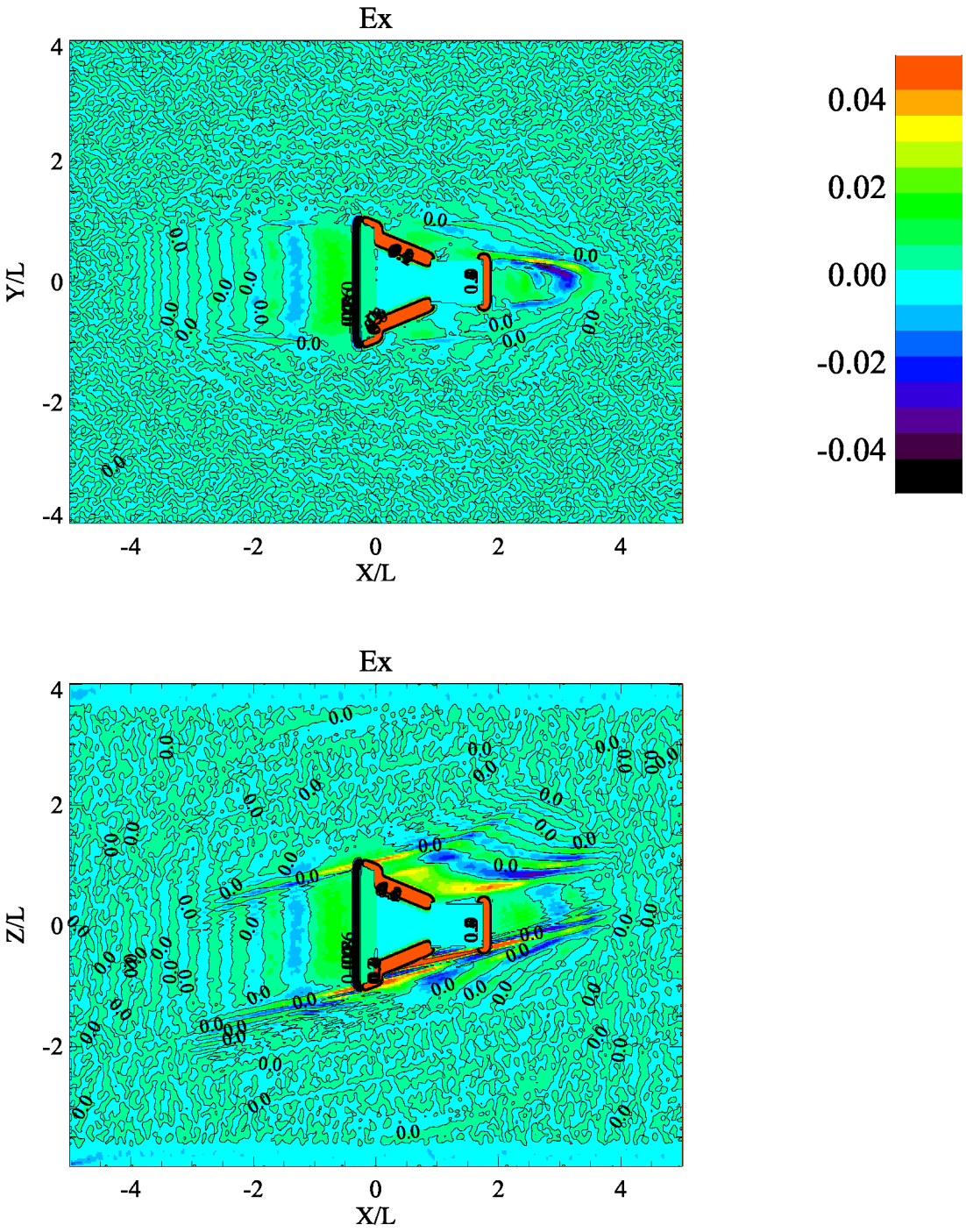

Figure 23. Electric field component $E_x(1.24\,\mathrm{V/m})$ in the y-x ($z = 0$) and z-x ($y = 0$) planes. $W = 200\,\mathrm{km/s}$, $M_A = 1.5$, $B_0 = 6250\,\mathrm{nT}$, $n_{SW} = 10^4\,\mathrm{cm}^{-3}$, $\beta_\mathrm{p} = 0.1$, $\beta_\mathrm{e} = 0.025$, $\theta_{bu} = 11^o$. Linear perturbations at the beginning of simulation $t = 0.014\,T_{ce}$

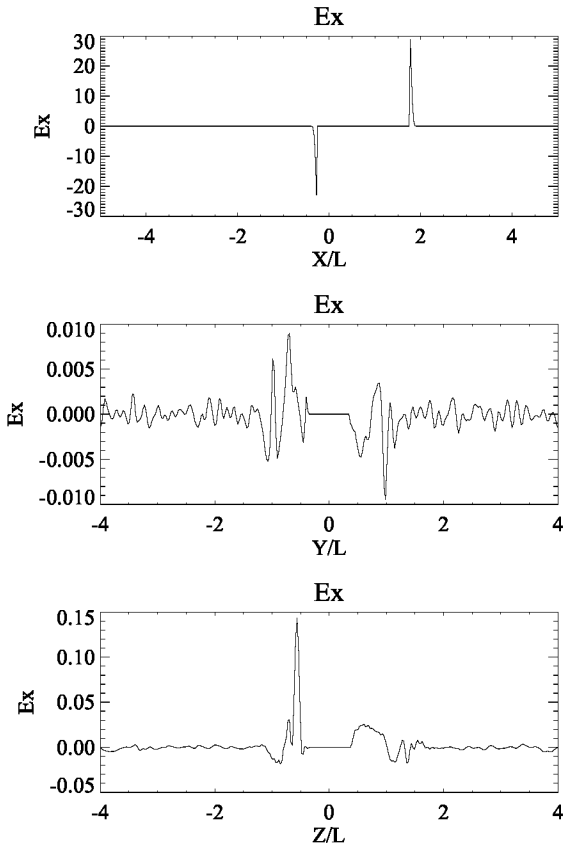

Figure 24. 1-D cuts for the electric field component $E_x(1.24\,\mathrm{V/m})$ (top: $y = 0$, $z = 0$; middle: $x = 1.5$, $z = 0$; bottom: $x = 1.5$, $y = 0$). $U_0 = 200\,\mathrm{km/s}$, $M_A = 1.5$, $B_0 = 6250\,\mathrm{nT}$, $n_{SW} = 10^4\,\mathrm{cm}^{-3}$, $\beta_\mathrm{p} = 0.1$, $\beta_\mathrm{e} = 0.025$, $\theta_{bu} = 11^o$. Linear perturbations at the beginning of simulation $t = 0.014\,T_{ce}$

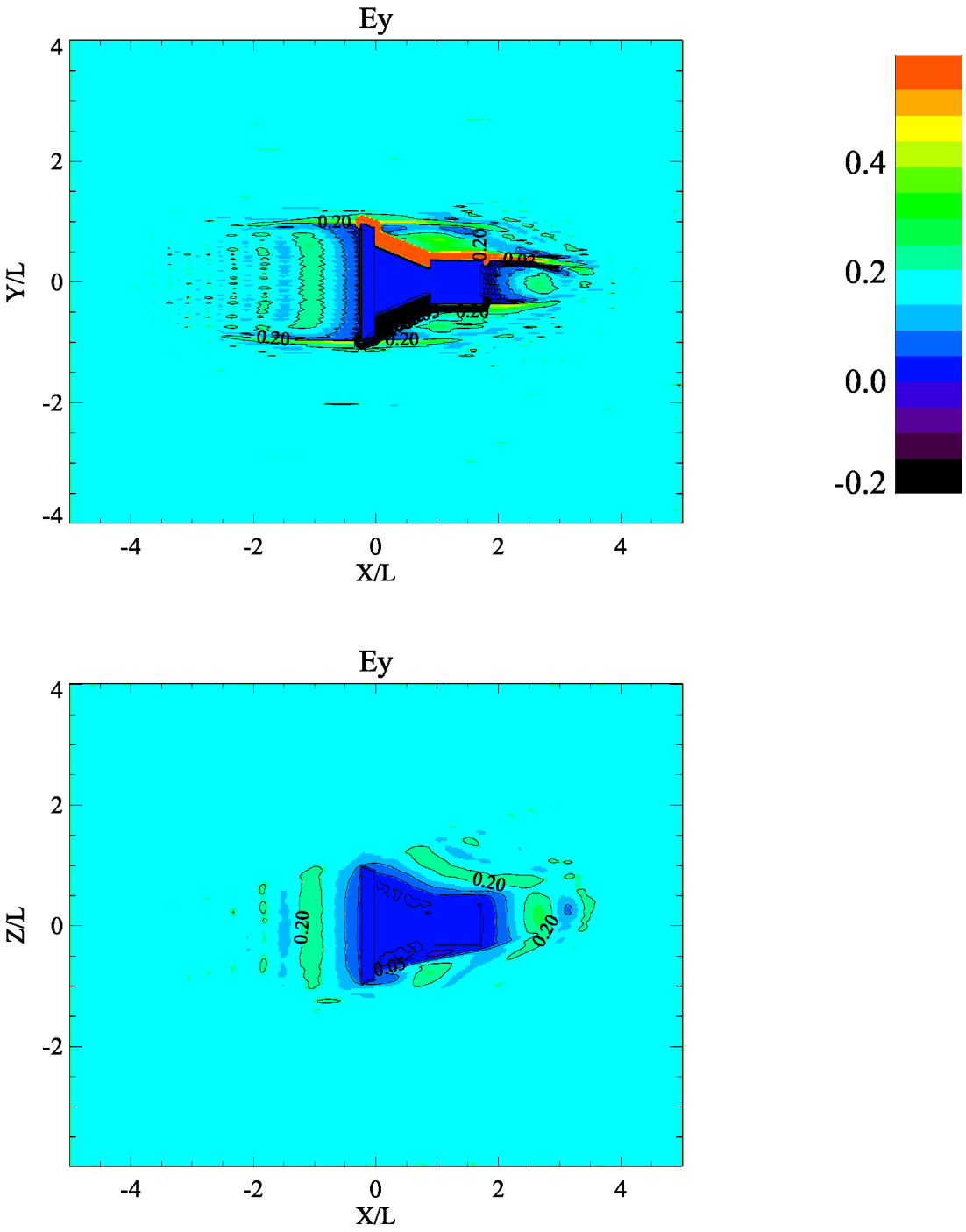

Figure 25. Electric field component $E_y(1.24\,\mathrm{V/m})$ in the y-x ($z = 0$) and z-x ($y = 0$) planes. $U_0 = 200\,\mathrm{km/s}$, $M_A = 1.5$, $B_0 = 6250\,\mathrm{nT}$, $n_{SW} = 10^4\,\mathrm{cm}^{-3}$, $\beta_\mathrm{p} = 0.1$, $\beta_\mathrm{e} = 0.025$, $\theta_{bu} = 11^o$. Linear perturbations at the beginning of simulation $t = 0.014\,T_{ce}$

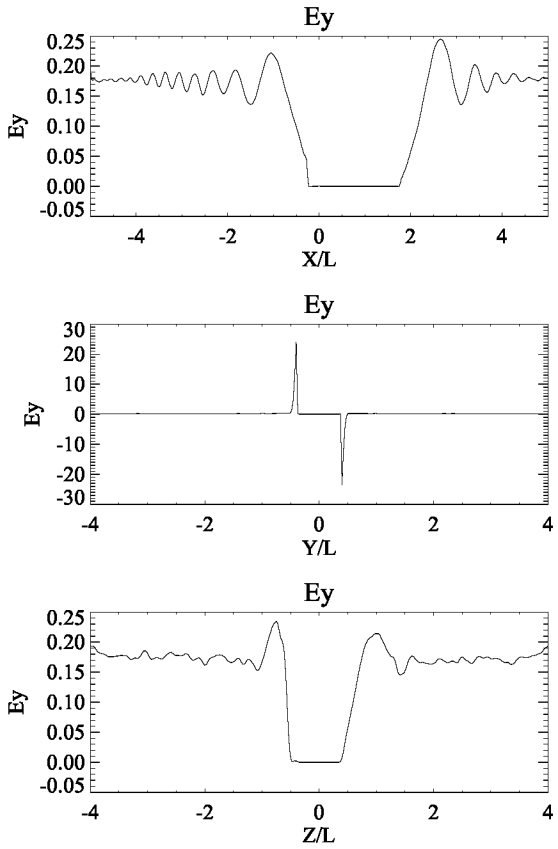

Figure 26. 1-D cuts for the electric field component $E_y(1.24\,\mathrm{V/m})$ (top: $y = 0$, $z = 0$; middle: $x = 1.5$, $z = 0$; bottom: $x = 1.5$, $y = 0$). $U_0 = 200\,\mathrm{km/s}$, $M_A = 1.5$, $B_0 = 6250\,\mathrm{nT}$, $n_{SW} = 10^4\,\mathrm{cm}^{-3}$, $\beta_\mathrm{p} = 0.1$, $\beta_\mathrm{e} = 0.025$, $\theta_{bu} = 11^o$. Linear perturbations at the beginning of simulation $t = 0.014\,T_{ce}$

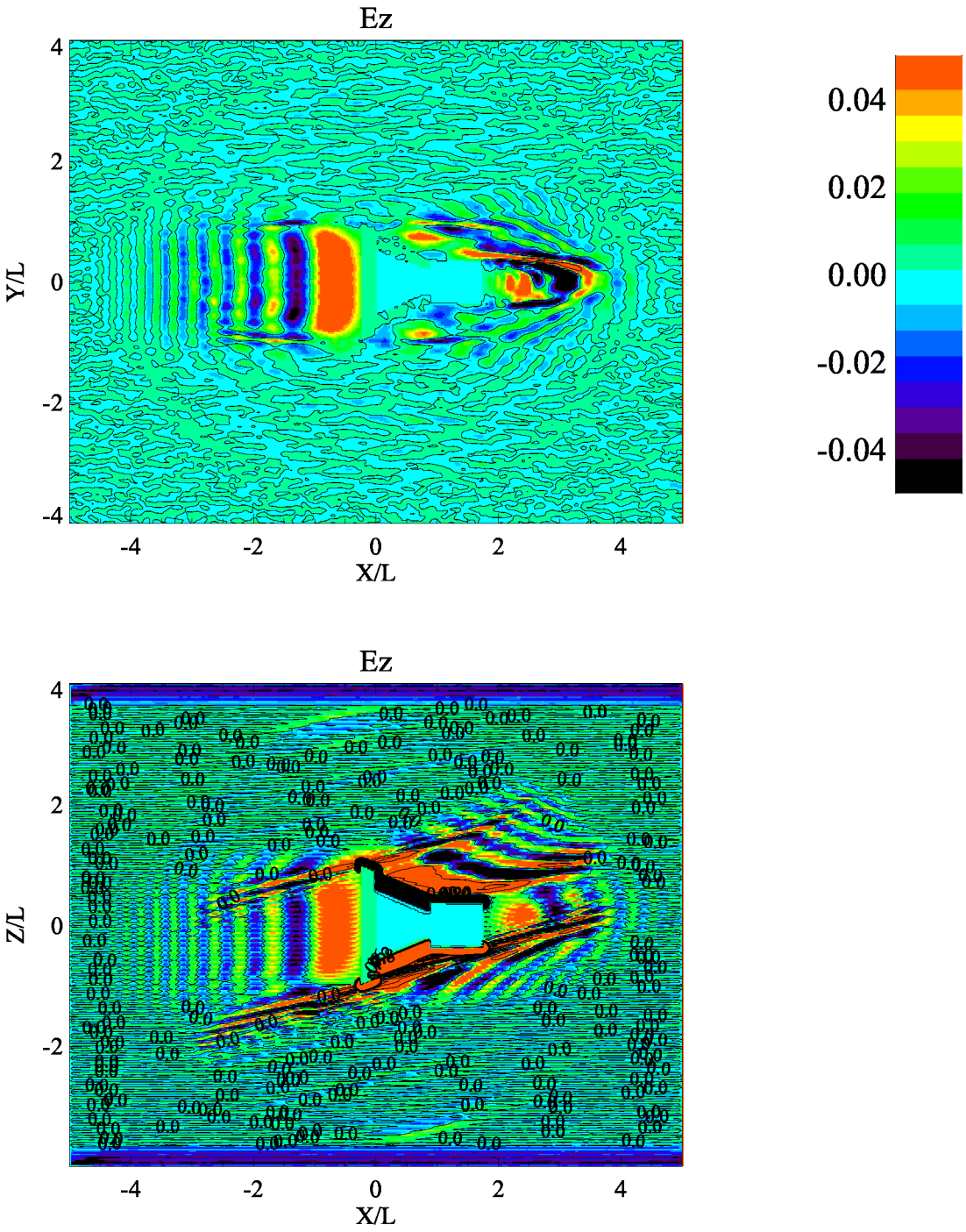

Figure 27. Electric field component $E_z(1.24\,\mathrm{V/m})$ in the y-x ($z = 0$) and z-x ($y = 0$) planes. $U_0 = 200\,\mathrm{km/s}$, $M_A = 1.5$, $B_0 = 6250\,\mathrm{nT}$, $n_{SW} = 10^4\,\mathrm{cm}^{-3}$, $\beta_\mathrm{p} = 0.1$, $\beta_\mathrm{e} = 0.025$, $\theta_{bu} = 11^o$. Linear perturbations at the beginning of simulation $t = 0.014\,T_{ce}$

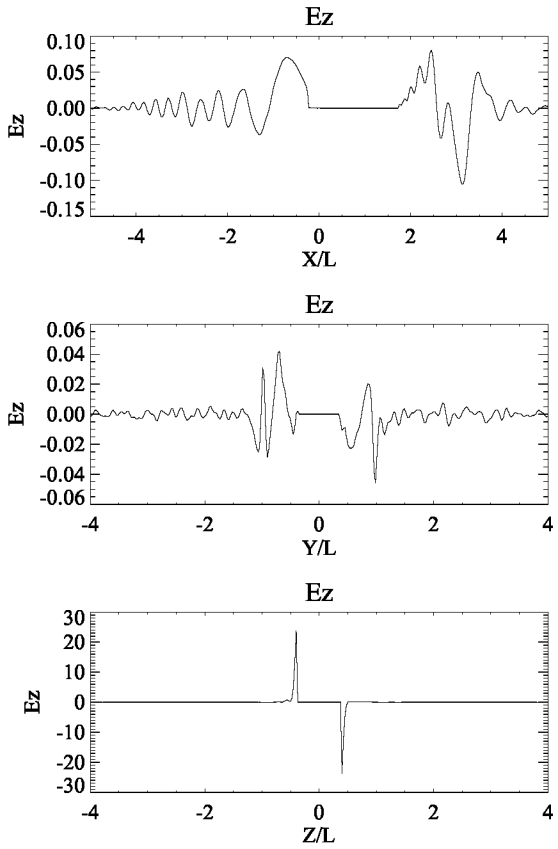

Figure 28. 1-D cuts for the electric field component $E_z(1.24\,\mathrm{V/m})$ (top: $y = 0$, $z = 0$; middle: $x = 1.5$, $z = 0$; bottom: $x = 1.5$, $y = 0$). $U_0 = 200\,\mathrm{km/s}$, $M_A = 1.5$, $B_0 = 6250\,\mathrm{nT}$, $n_{SW} = 10^4\,\mathrm{cm}^{-3}$, $\beta_\mathrm{p} = 0.1$, $\beta_\mathrm{e} = 0.025$, $\theta_{bu} = 11^o$. Linear perturbations at the beginning of simulation $t = 0.014\,T_{ce}$

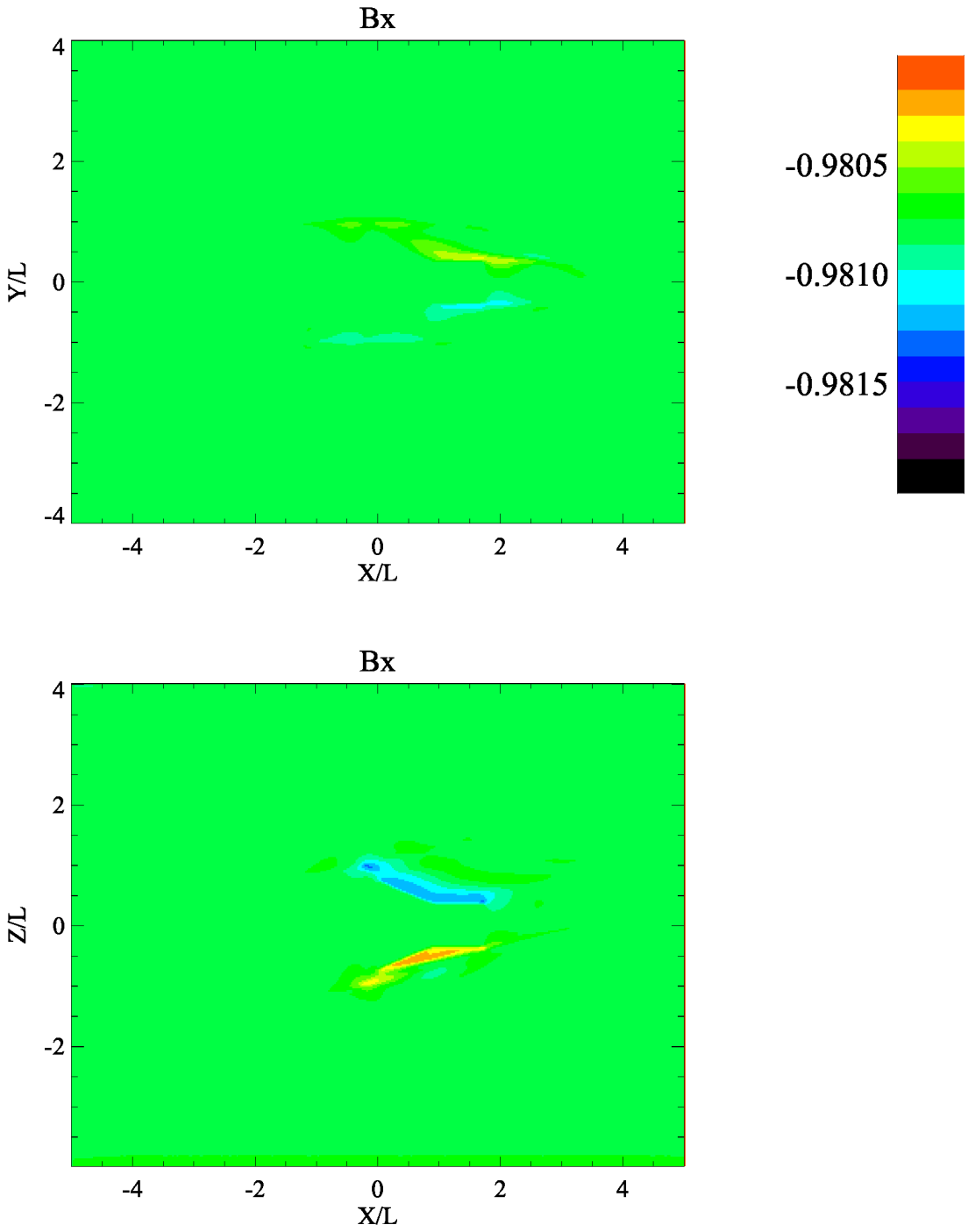

Figure 29. Magnetic field component $B_x(6250\,\mathrm{nT})$ in the y-x ($z = 0$) and z-x ($y = 0$) planes. $U_0 = 200\,\mathrm{km/s}$, $M_A = 1.5$, $B_0 = 6250\,\mathrm{nT}$, $n_{SW} = 10^4\,\mathrm{cm}^{-3}$, $\beta_\mathrm{p} = 0.1$, $\beta_\mathrm{e} = 0.025$, $\theta_{bu} = 11^o$. Linear perturbations at the beginning of simulation $t = 0.014\,T_{ce}$

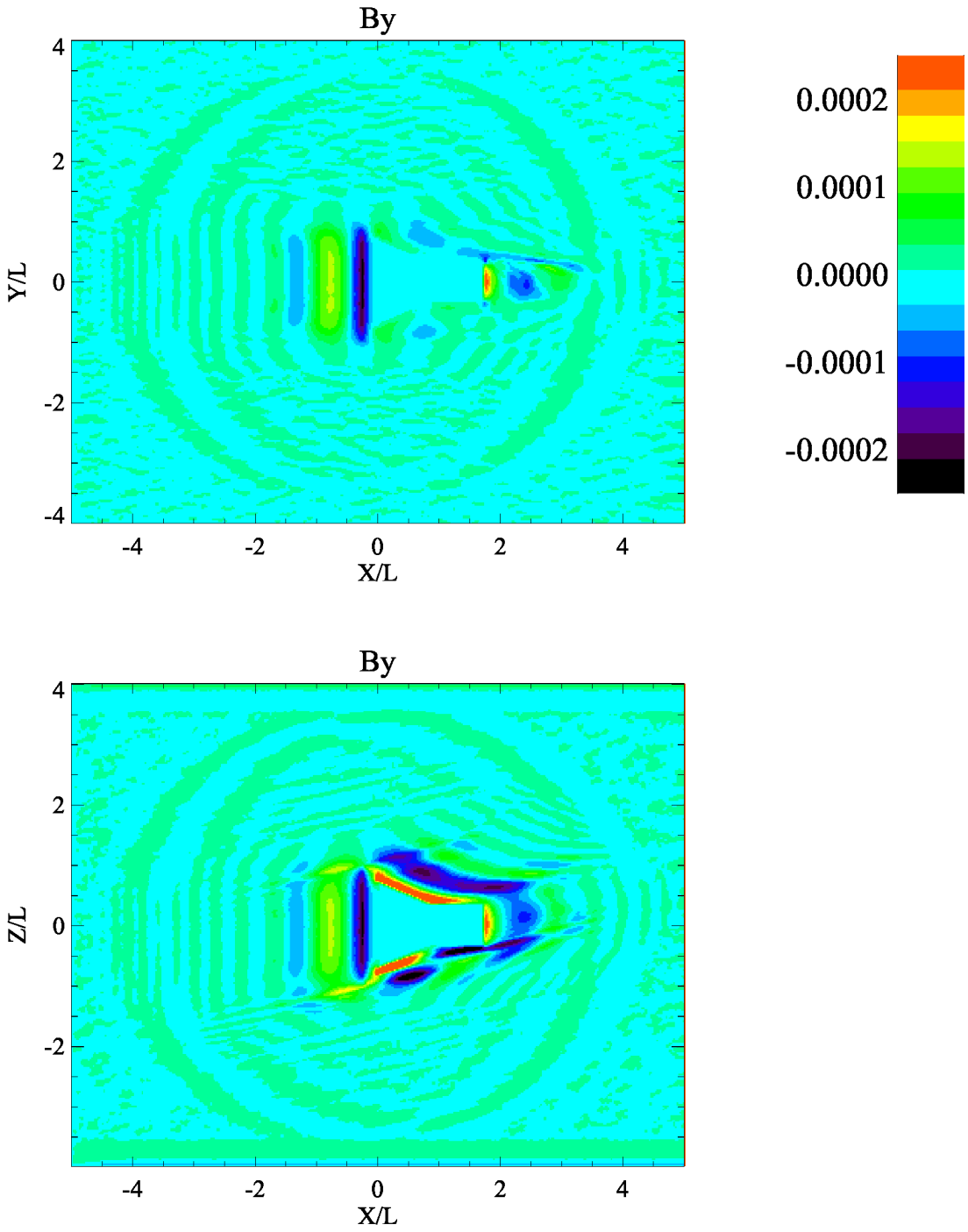

Figure 30. Magnetic field component $B_y(6250\,\mathrm{nT})$ in the y-x ($z = 0$) and z-x ($y = 0$) planes. $U_0 = 200\,\mathrm{km/s}$, $M_A = 1.5$, $B_0 = 6250\,\mathrm{nT}$, $n_{SW} = 10^4\,\mathrm{cm}^{-3}$, $\beta_\mathrm{p} = 0.1$, $\beta_\mathrm{e} = 0.025$, $\theta_{bu} = 11^o$. Linear perturbations at the beginning of simulation $t = 0.014\,T_{ce}$

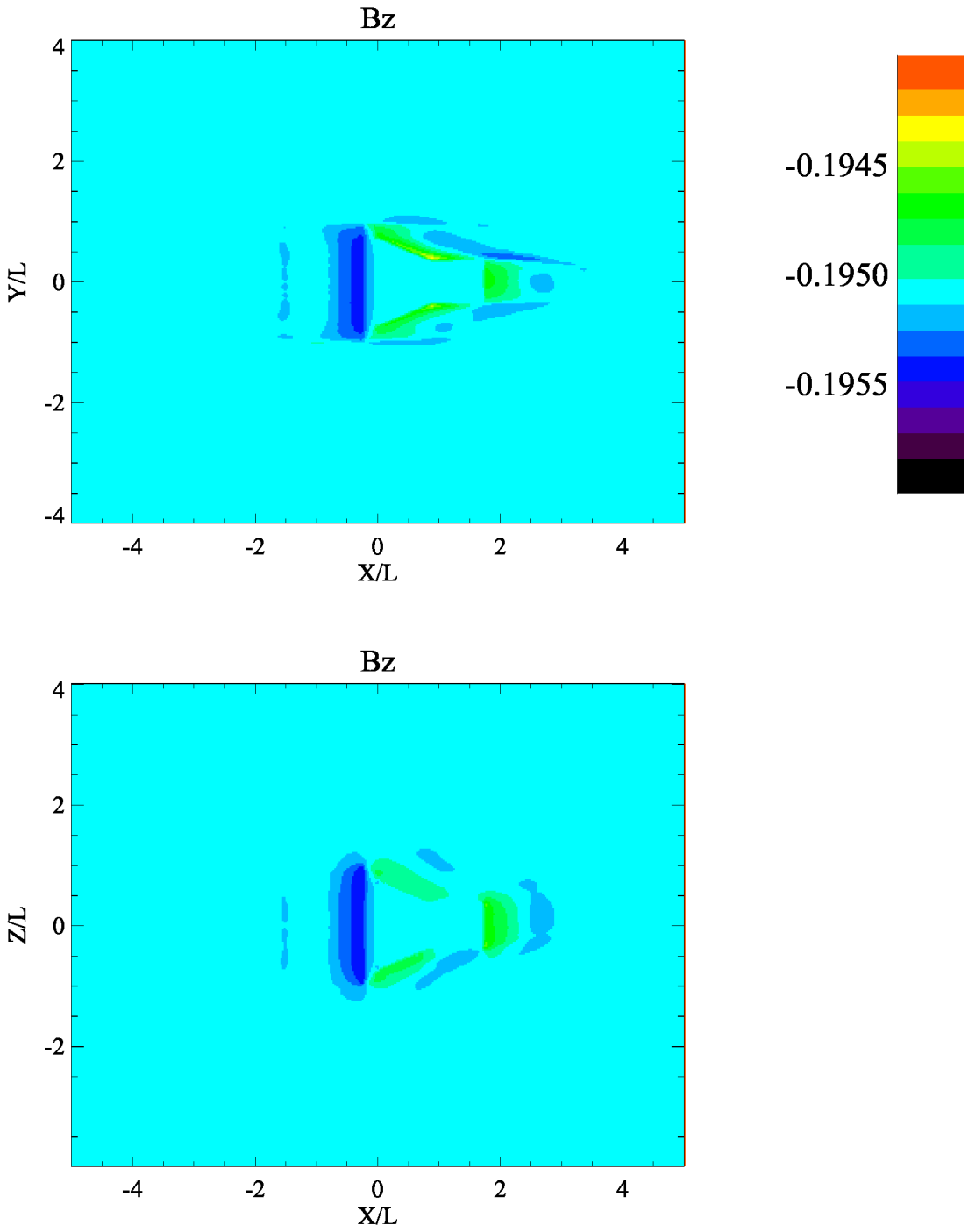

Figure 31. Magnetic field component $B_z(6250\,\mathrm{nT})$ in the y-x ($z = 0$) and z-x ($y = 0$) planes. $U_0 = 200\,\mathrm{km/s}$, $M_A = 1.5$, $B_0 = 6250\,\mathrm{nT}$, $n_{SW} = 10^4\,\mathrm{cm}^{-3}$, $\beta_\mathrm{p} = 0.1$, $\beta_\mathrm{e} = 0.025$, $\theta_{bu} = 11^o$. Linear perturbations at the beginning of simulation $t = 0.014\,T_{ce}$

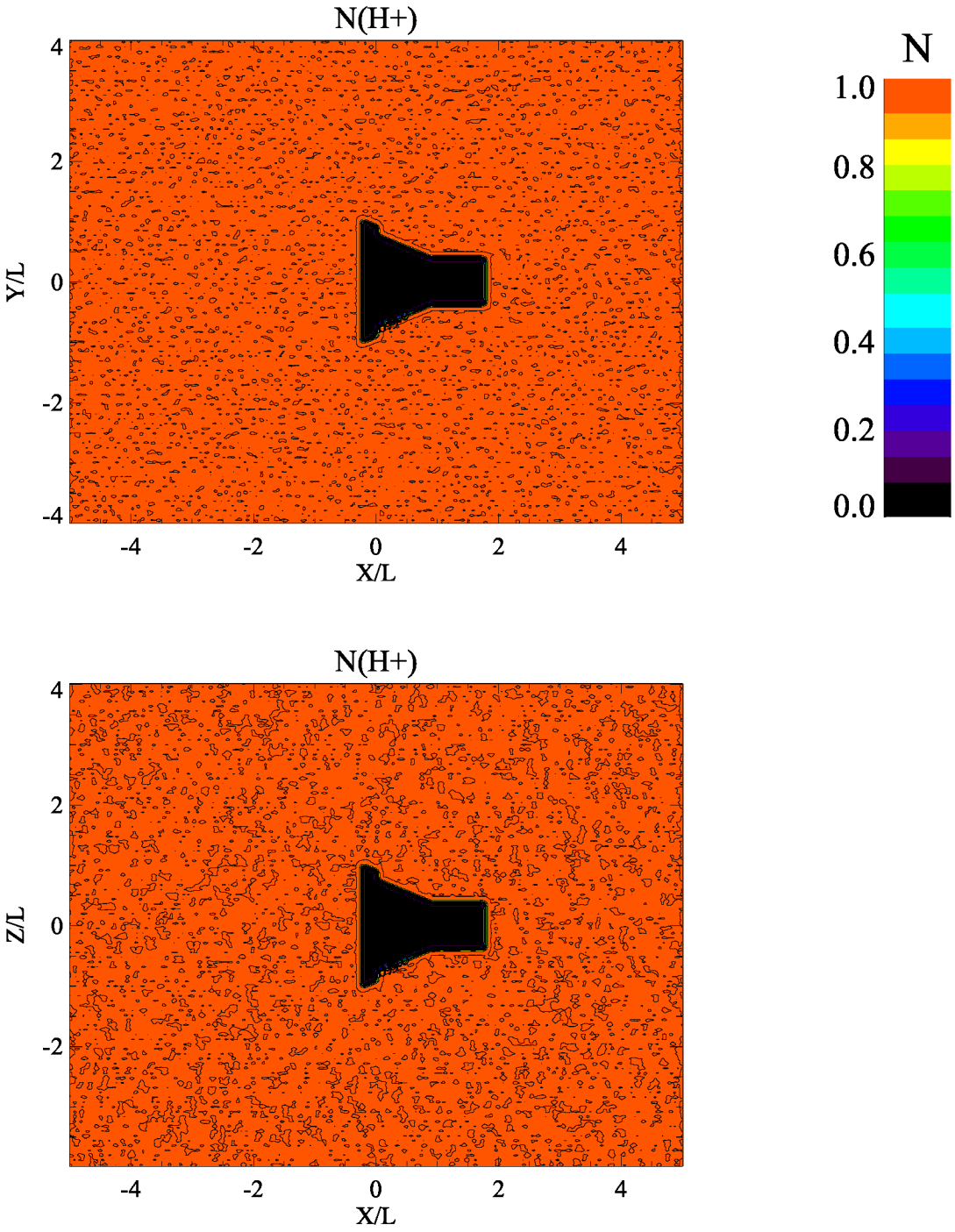

Figure 32. Solar wind ion density in the y-x ($z = 0$) and z-x ($y = 0$) planes. $U_0 = 200\,\mathrm{km/s}$, $M_A = 1.5$, $B_0 = 6250\,\mathrm{nT}$, $E_0 = U_0 B_0 = 1.24\mathrm{V/m}$, $n_{SW} = 10^4\,\mathrm{cm}^{-3}$, $\beta_\mathrm{p} = 0.1$, $\beta_\mathrm{e} = 0.025$, $\theta_{bu} = 11^o$. Nonlinear saturation of the perturbations at $t = 0.03\,T_{ce}$

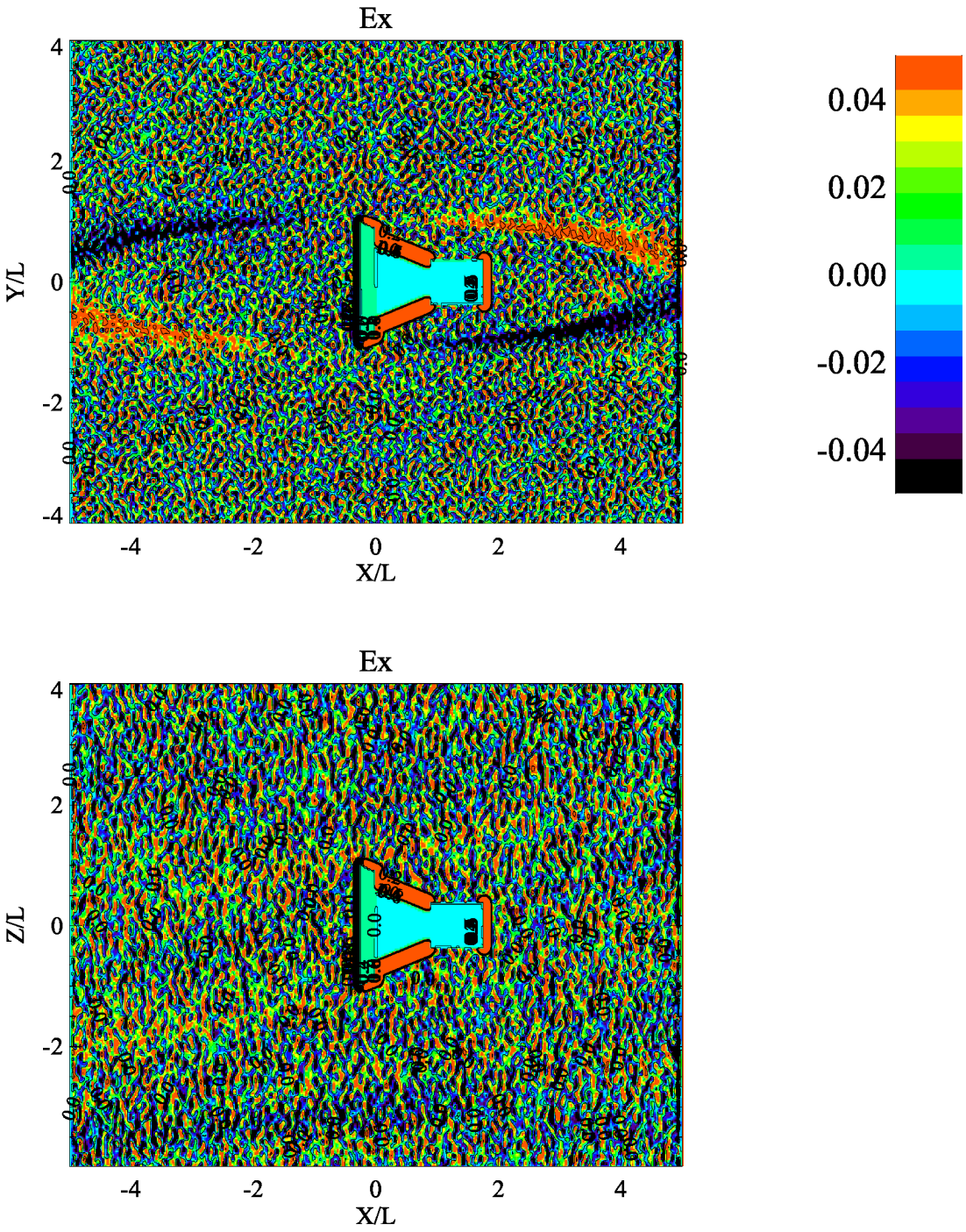

Figure 33. Electric field component $E_x(1.24\,\mathrm{V/m})$ in the y-x ($z = 0$) and z-x ($y = 0$) planes. $U_0 = 200\,\mathrm{km/s}$, $M_A = 1.5$, $B_0 = 6250\,\mathrm{nT}$, $n_{SW} = 10^4\,\mathrm{cm}^{-3}$, $\beta_\mathrm{p} = 0.1$, $\beta_\mathrm{e} = 0.025$, $\theta_{bu} = 11^o$. Nonlinear saturation of the perturbations at $t = 0.03\,T_{ce}$

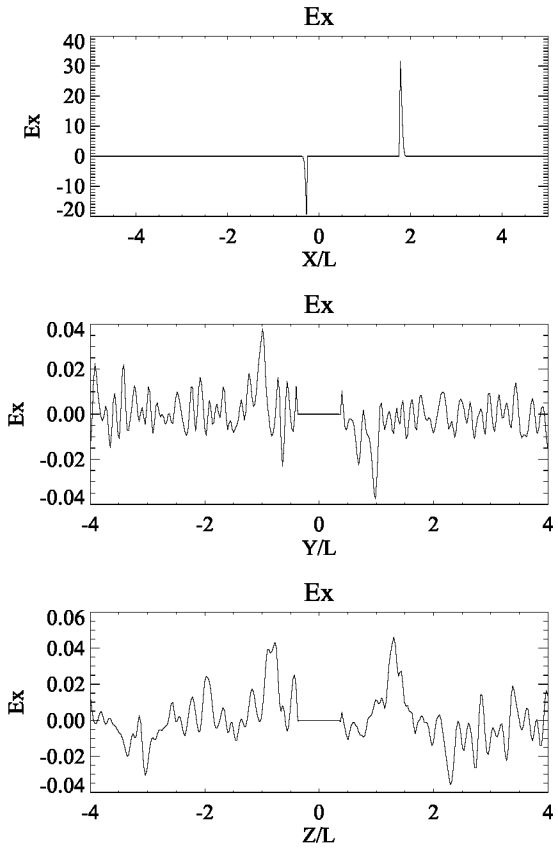

Figure 34. 1-D cuts for the electric field component $E_x(1.24\,\mathrm{V/m})$ (top: $y = 0$, $z = 0$; middle: $x = 1.5$, $z = 0$; bottom: $x = 1.5$, $y = 0$). $U_0 = 200\,\mathrm{km/s}$, $M_A = 1.5$, $B_0 = 6250\,\mathrm{nT}$, $n_{SW} = 10^4\,\mathrm{cm}^{-3}$, $\beta_\mathrm{p} = 0.1$, $\beta_\mathrm{e} = 0.025$, $\theta_{bu} = 11^o$. Nonlinear saturation of the perturbations at $t = 0.03\,T_{ce}$

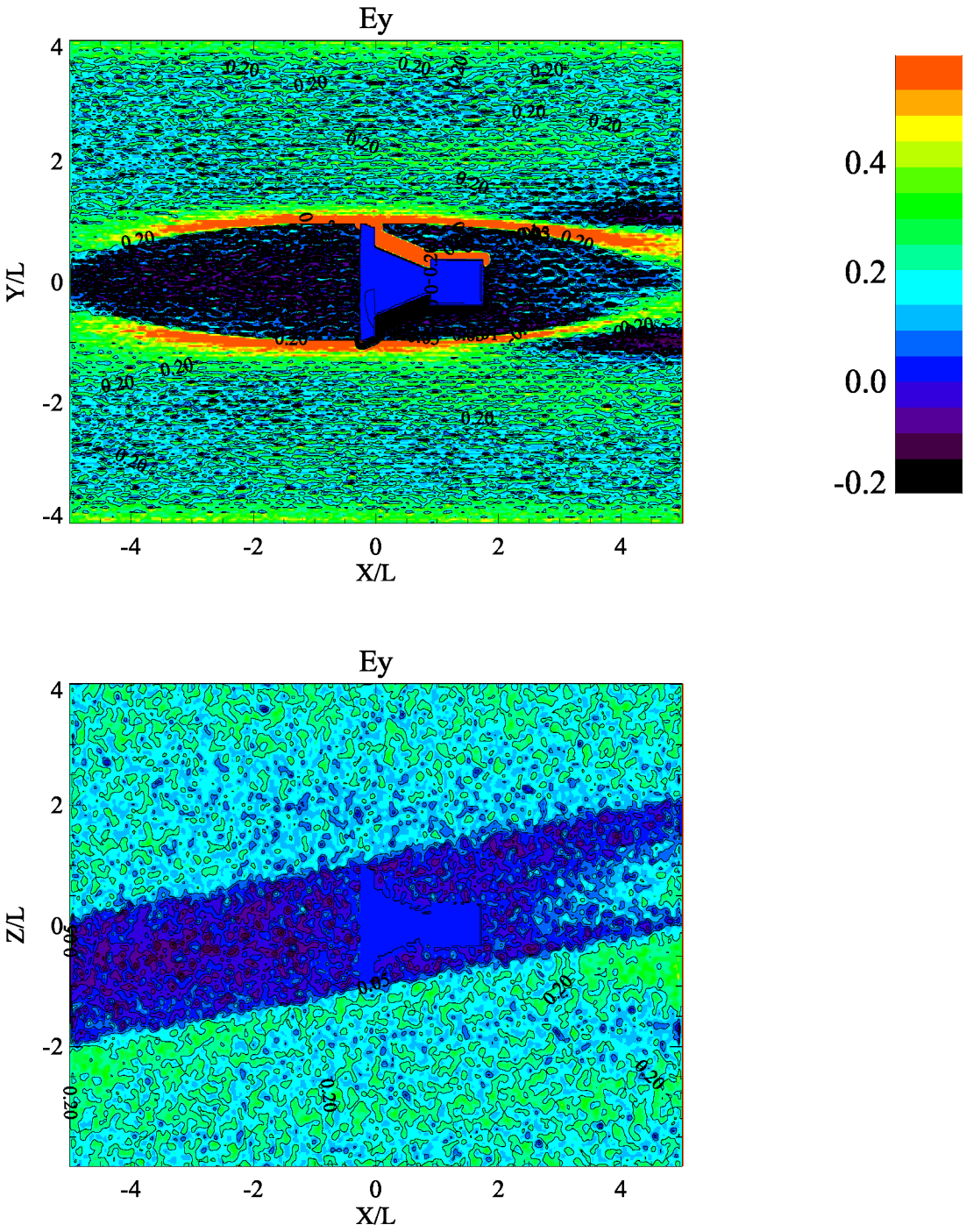

Figure 35. Electric field component $E_y(1.24\,\mathrm{V/m})$ in the y-x ($z = 0$) and z-x ($y = 0$) planes. $U_0 = 200\,\mathrm{km/s}$, $M_A = 1.5$, $B_0 = 6250\,\mathrm{nT}$, $n_{SW} = 10^4\,\mathrm{cm}^{-3}$, $\beta_\mathrm{p} = 0.1$, $\beta_\mathrm{e} = 0.025$, $\theta_{bu} = 11^o$. Nonlinear saturation of the perturbations at $t = 0.03\,T_{ce}$

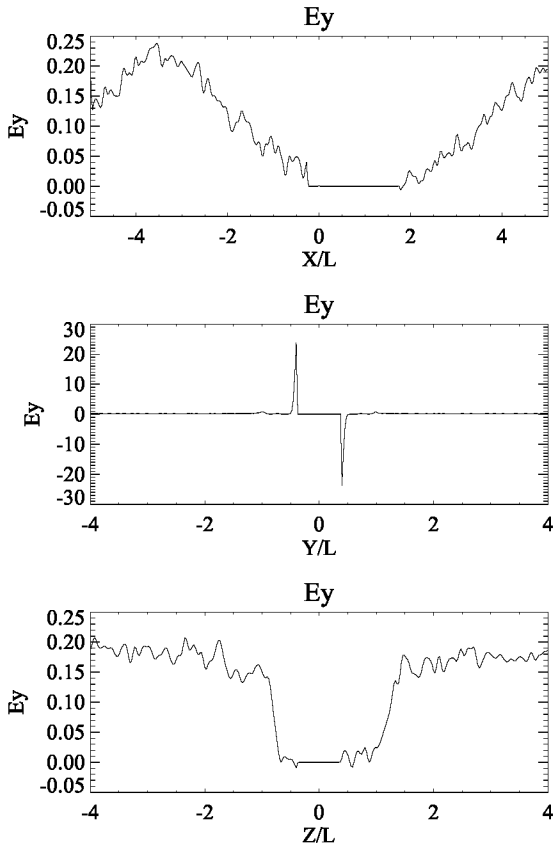

Figure 36. 1-D cuts for the electric field component $E_y(1.24\,\mathrm{V/m})$ (top: $y = 0$, $z = 0$; middle: $x = 1.5$, $z = 0$; bottom: $x = 1.5$, $y = 0$). $U_0 = 200\,\mathrm{km/s}$, $M_A = 1.5$, $B_0 = 6250\,\mathrm{nT}$, $n_{SW} = 10^4\,\mathrm{cm}^{-3}$, $\beta_\mathrm{p} = 0.1$, $\beta_\mathrm{e} = 0.025$, $\theta_{bu} = 11^o$. Nonlinear saturation of the perturbations at $t = 0.03\,T_{ce}$

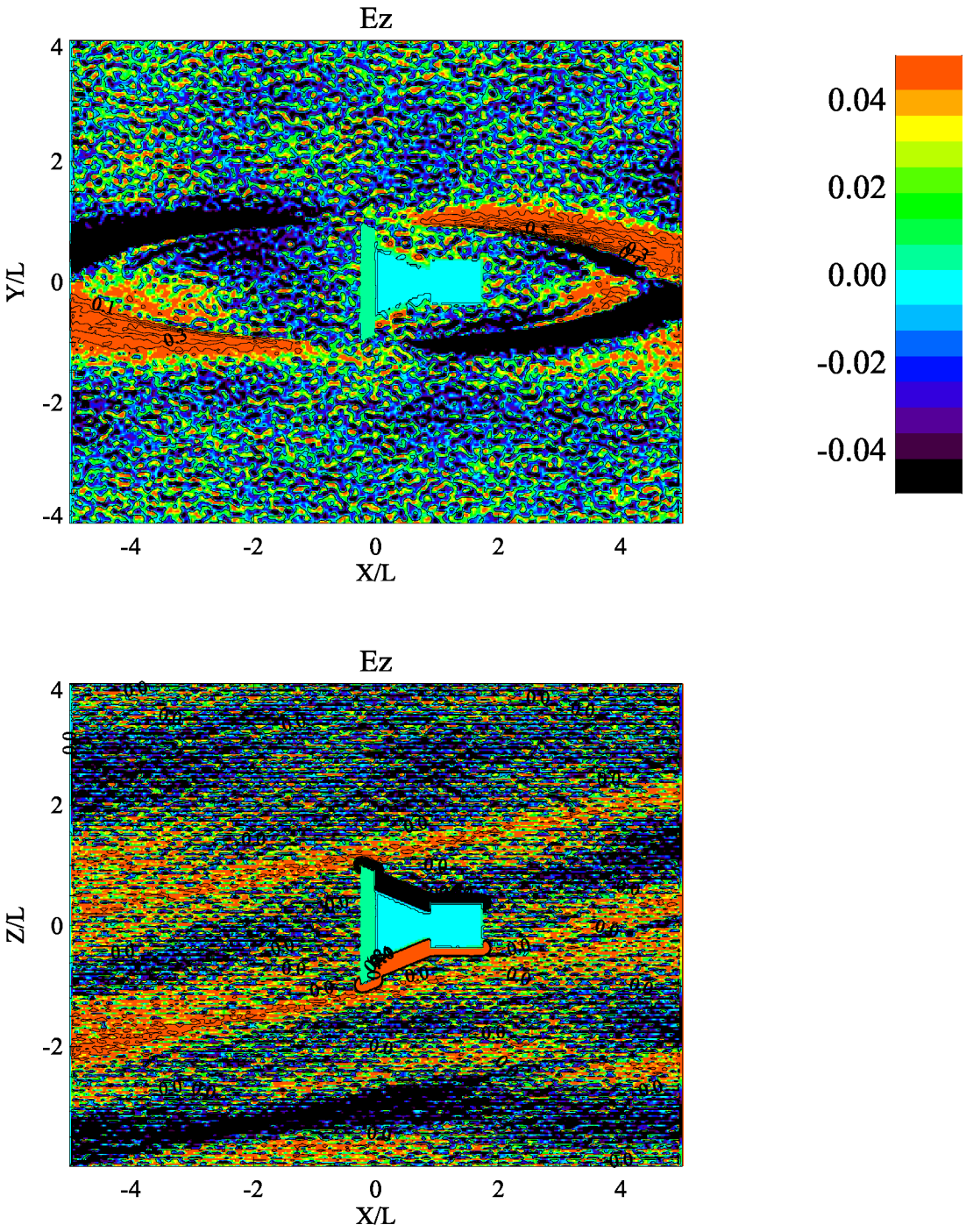

Figure 37. Electric field component $E_z(1.24\,\mathrm{V/m})$ in the y-x ($z = 0$) and z-x ($y = 0$) planes. $U_0 = 200\,\mathrm{km/s}$, $M_A = 1.5$, $B_0 = 6250\,\mathrm{nT}$, $n_{SW} = 10^4\,\mathrm{cm}^{-3}$, $\beta_\mathrm{p} = 0.1$, $\beta_\mathrm{e} = 0.025$, $\theta_{bu} = 11^o$. Nonlinear saturation of the perturbations at $t = 0.03\,T_{ce}$

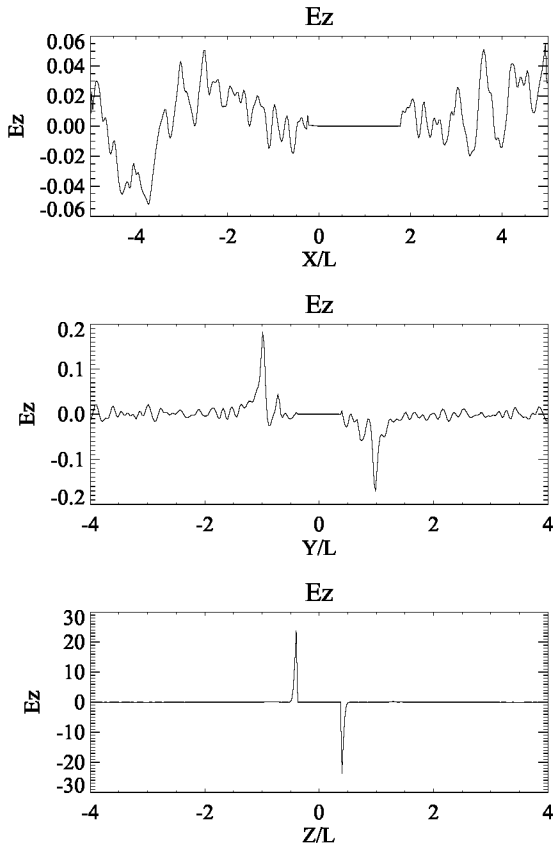

Figure 38. 1-D cuts for the electric field component $E_z(1.24\,\mathrm{V/m})$ (top: $y = 0$, $z = 0$; middle: $x = 1.5$, $z = 0$; bottom: $x = 1.5$, $y = 0$). $U_0 = 200\,\mathrm{km/s}$, $M_A = 1.5$, $B_0 = 6250\,\mathrm{nT}$, $n_{SW} = 10^4\,\mathrm{cm}^{-3}$, $\beta_\mathrm{p} = 0.1$, $\beta_\mathrm{e} = 0.025$, $\theta_{bu} = 11^o$. Nonlinear saturation of the perturbations at $t = 0.03\,T_{ce}$

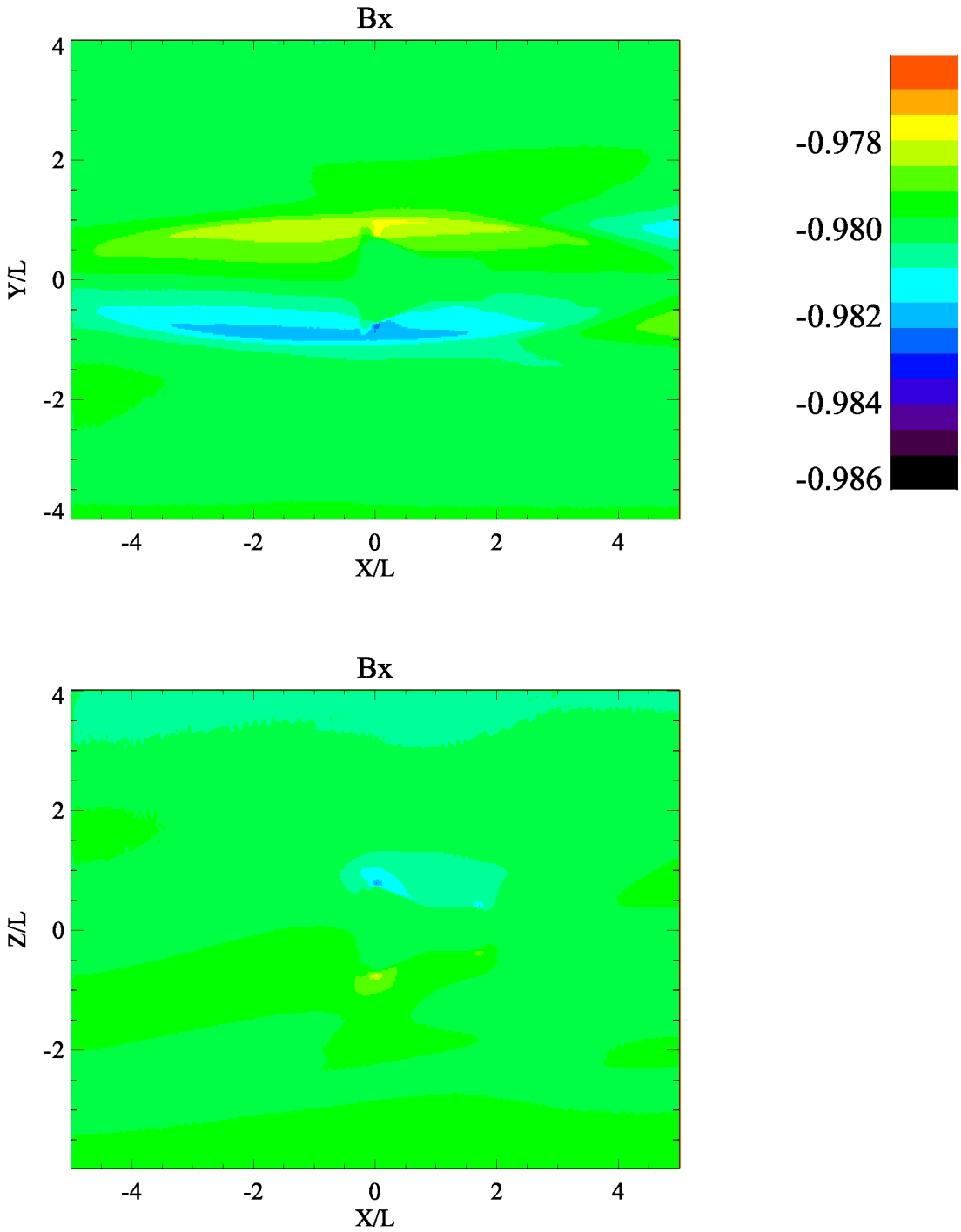

Figure 39. Magnetic field component $B_x(6250\,\mathrm{nT})$ in the y-x ($z = 0$) and z-x ($y = 0$) planes. $U_0 = 200\,\mathrm{km/s}$, $M_A = 1.5$, $B_0 = 6250\,\mathrm{nT}$, $n_{SW} = 10^4\,\mathrm{cm}^{-3}$, $\beta_\mathrm{p} = 0.1$, $\beta_\mathrm{e} = 0.025$, $\theta_{bu} = 11^o$. Nonlinear saturation of the perturbations at $t = 0.03\,T_{ce}$

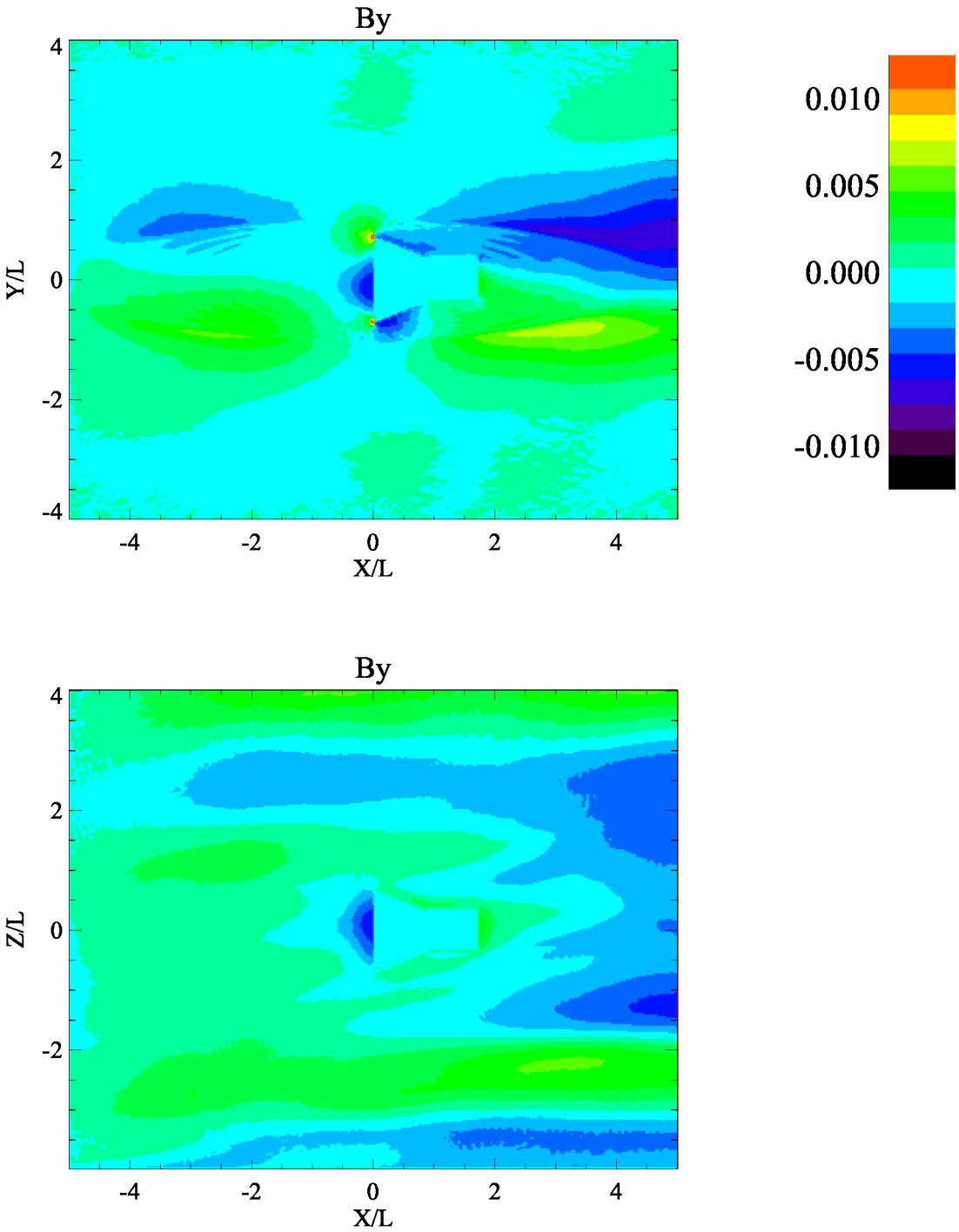

Figure 40. Magnetic field component $B_y(6250\,\mathrm{nT})$ in the y-x ($z = 0$) and z-x ($y = 0$) planes. $U_0 = 200\,\mathrm{km/s}$, $M_A = 1.5$, $B_0 = 6250\,\mathrm{nT}$, $n_{SW} = 10^4\,\mathrm{cm}^{-3}$, $\beta_\mathrm{p} = 0.1$, $\beta_\mathrm{e} = 0.025$, $\theta_{bu} = 11^o$. Nonlinear saturation of the perturbations at $t = 0.03\,T_{ce}$

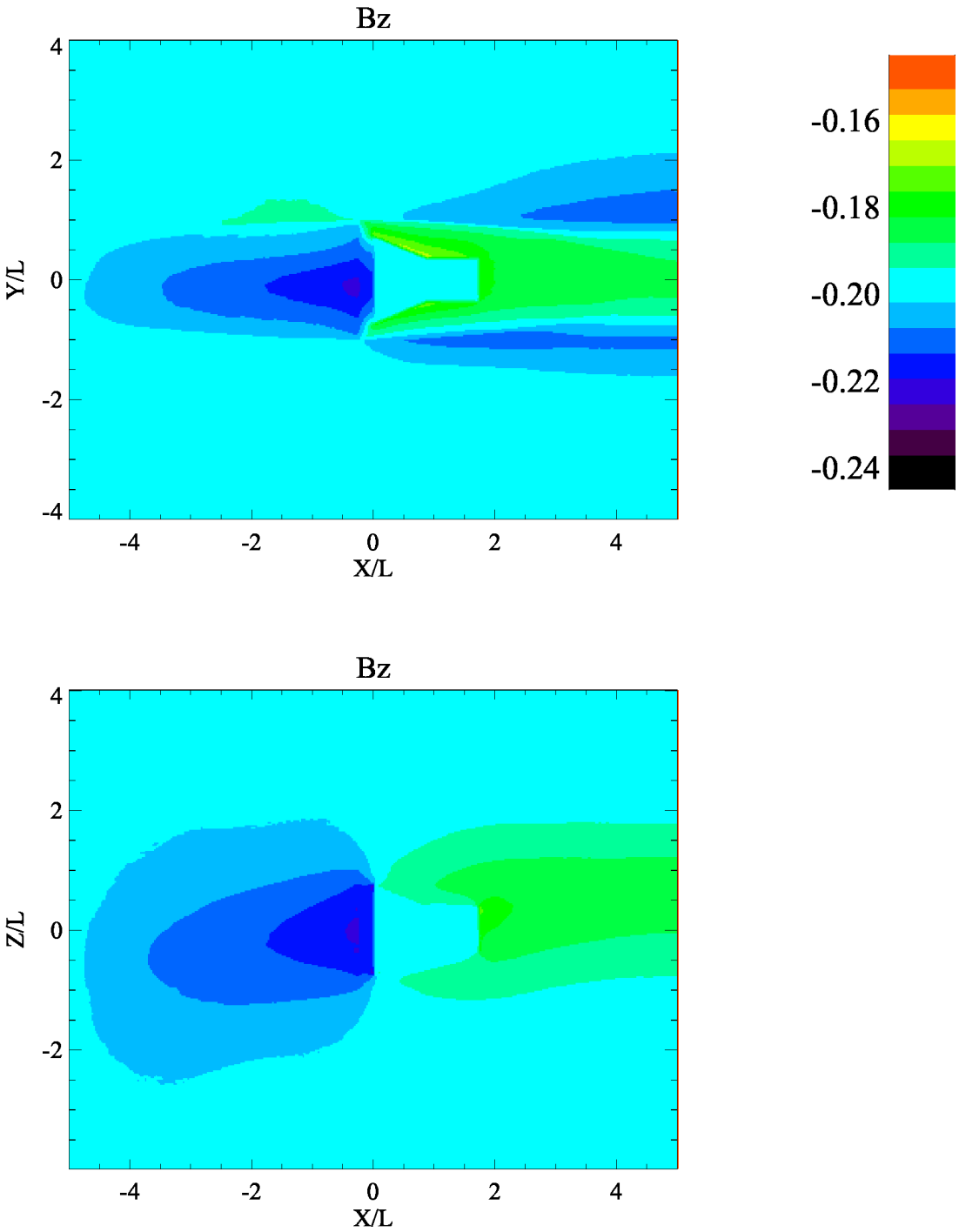

Figure 41. Magnetic field component $B_z(6250\,\mathrm{nT})$ in the y-x ($z = 0$) and z-x ($y = 0$) planes. $U_0 = 200\,\mathrm{km/s}$, $M_A = 1.5$, $B_0 = 6250\,\mathrm{nT}$, $n_W = 10^4\,\mathrm{cm}^{-3}$, $\beta_\mathrm{p} = 0.1$, $\beta_\mathrm{e} = 0.025$, $\theta_{bu} = 11^o$. Nonlinear saturation of the perturbations at $t = 0.03\,T_{ce}$

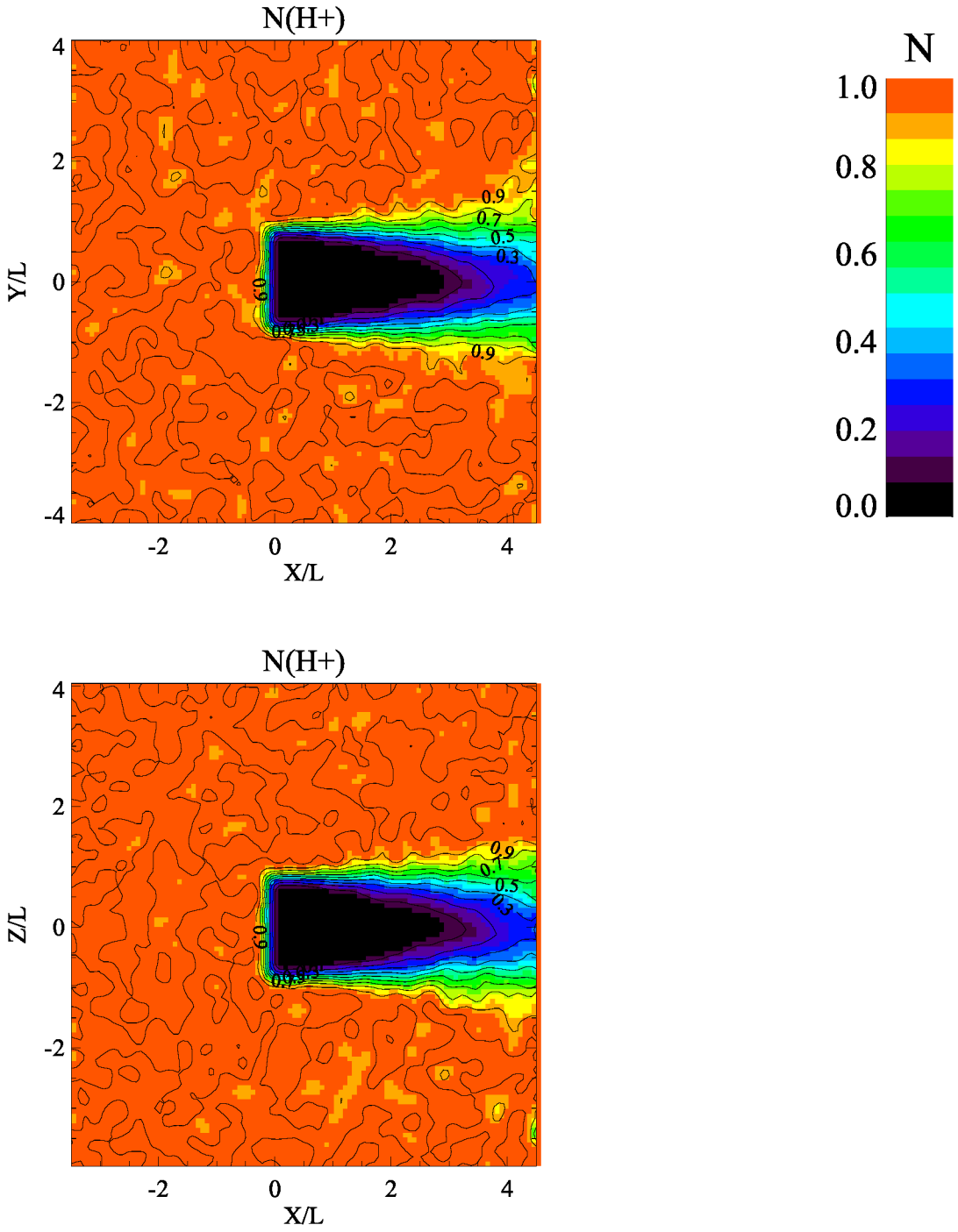

Figure 42. Solar wind ion density in the y-x ($z = 0$) and z-x ($y = 0$) planes. $U_0 = 200\,\mathrm{km/s}$, $M_A = 2$, $B_0 = 6250\,\mathrm{nT}$, $E_0 = U_0 B_0 = 1.24\mathrm{V/m}$, $n_{SW} = 10^4\,\mathrm{cm}^{-3}$, $\beta_\mathrm{p} = 0.1$, $\beta_\mathrm{e} = 0.0125$, $\theta_{bu} = 45^o$, $t = 13.6\,T_{ce}(1.875\,T_{transit.})$

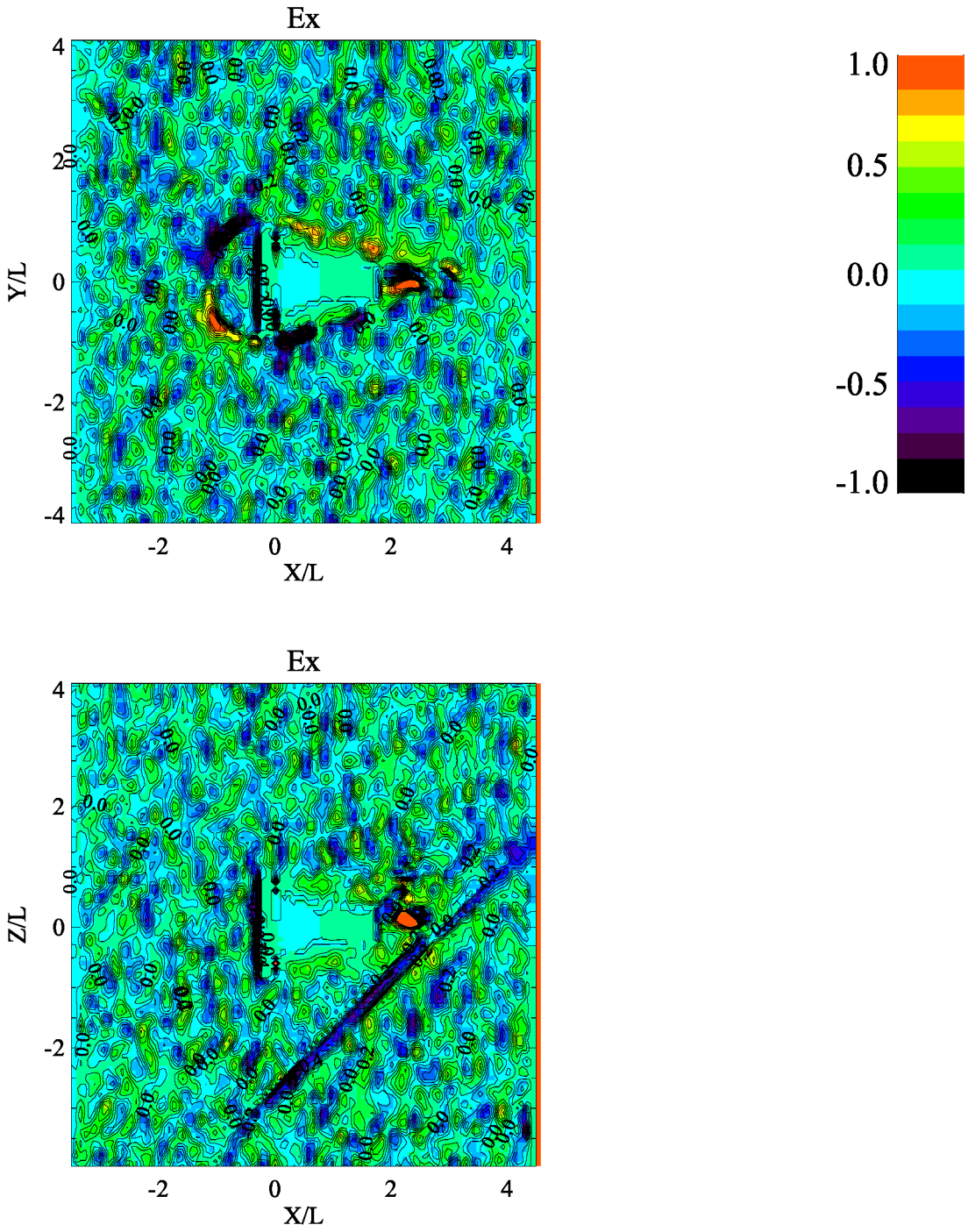

Figure 43. Electric field component $E_x(1.24\,\mathrm{V/m})$ in the y-x ($z = 0$) and z-x ($y = 0$) planes. $U_0 = 200\,\mathrm{km/s}$, $M_A = 2$, $B_0 = 6250\,\mathrm{nT}$, $n_{SW} = 10^4\,\mathrm{cm}^{-3}$, $\beta_\mathrm{p} = 0.1$, $\beta_\mathrm{e} = 0.0125$, $\theta_{bu} = 45^o$, $t = 13.6\,T_{ce}(1.875\,T_{transit.})$

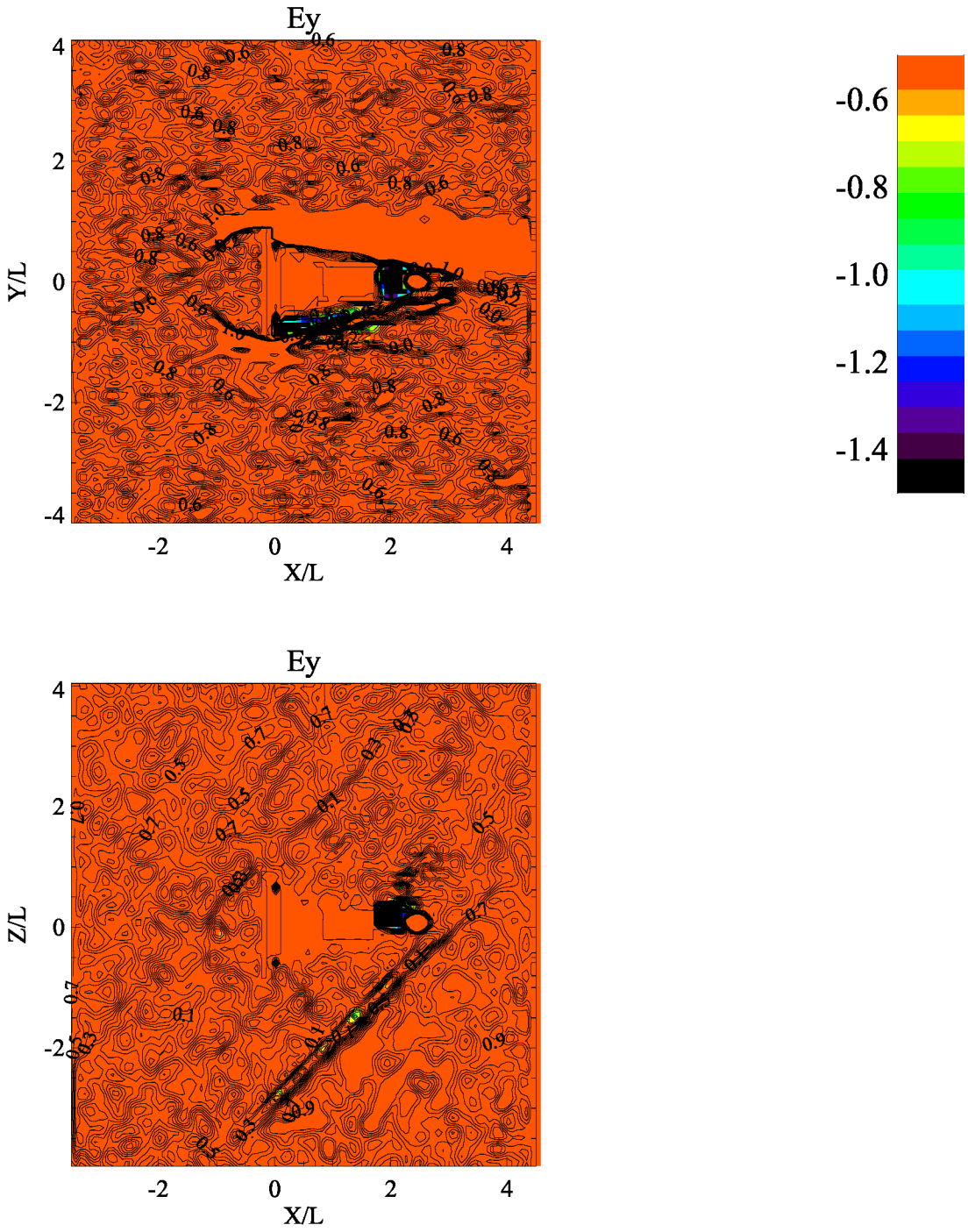

Figure 44. Electric field component $E_y(1.24\,\mathrm{V/m})$ in the y-x ($z = 0$) and z-x ($y = 0$) planes. $U_0 = 200\,\mathrm{km/s}$, $M_A = 2$, $B_0 = 6250\,\mathrm{nT}$, $n_{SW} = 10^4\,\mathrm{cm}^{-3}$, $\beta_\mathrm{p} = 0.1$, $\beta_\mathrm{e} = 0.0125$, $\theta_{bu} = 45^o$, $t = 13.6\,T_{ce}(1.875\,T_{transit.})$

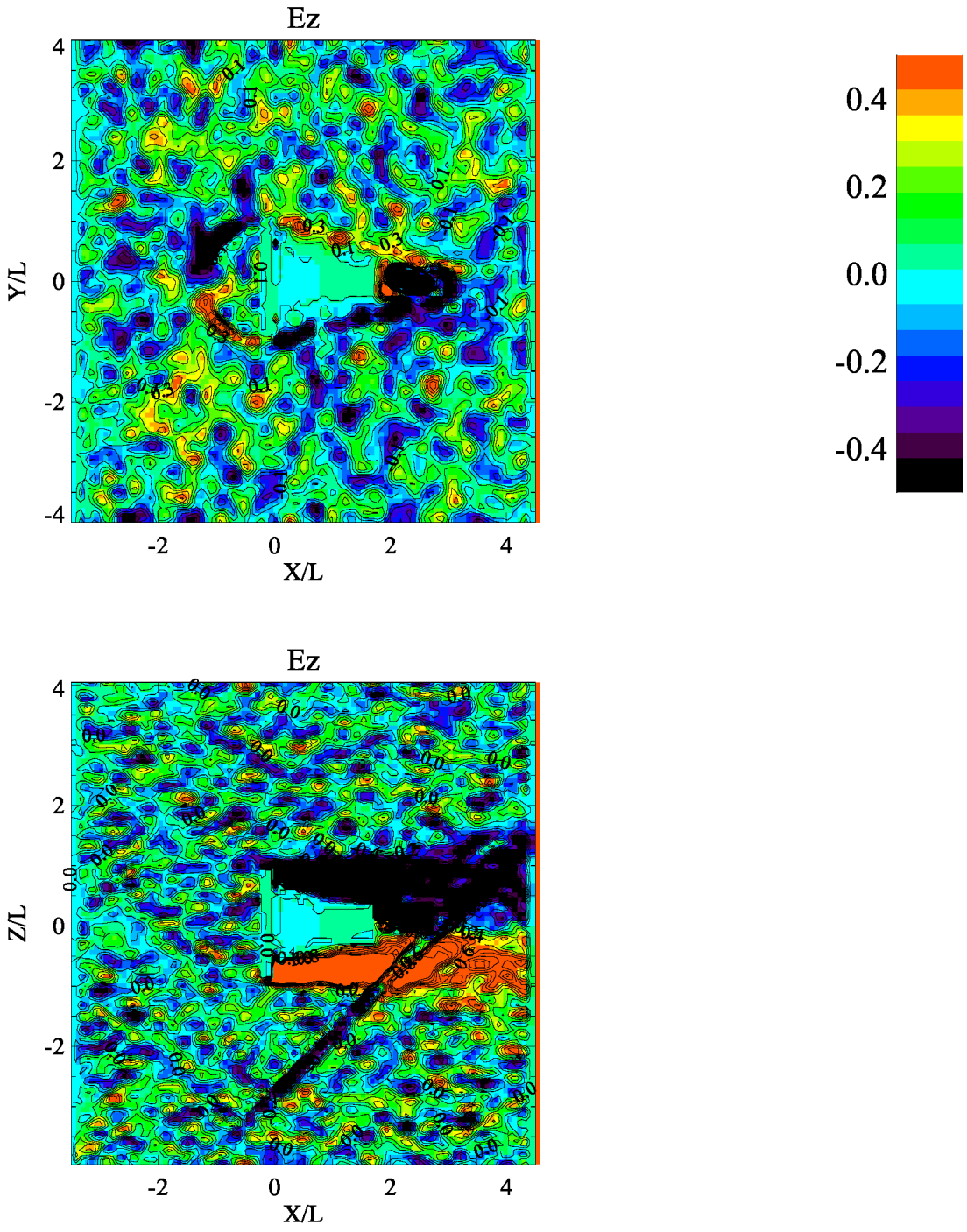

Figure 45. Electric field component $E_z(1.24\,\mathrm{V/m})$ in the y-x ($z = 0$) and z-x ($y = 0$) planes. $U_0 = 200\,\mathrm{km/s}$, $M_A = 2$, $B_0 = 6250\,\mathrm{nT}$, $n_{SW} = 10^4\,\mathrm{cm}^{-3}$, $\beta_\mathrm{p} = 0.1$, $\beta_\mathrm{e} = 0.0125$, $\theta_{bu} = 45^o$, $t = 13.6\,T_{ce}(1.875\,T_{transit.})$

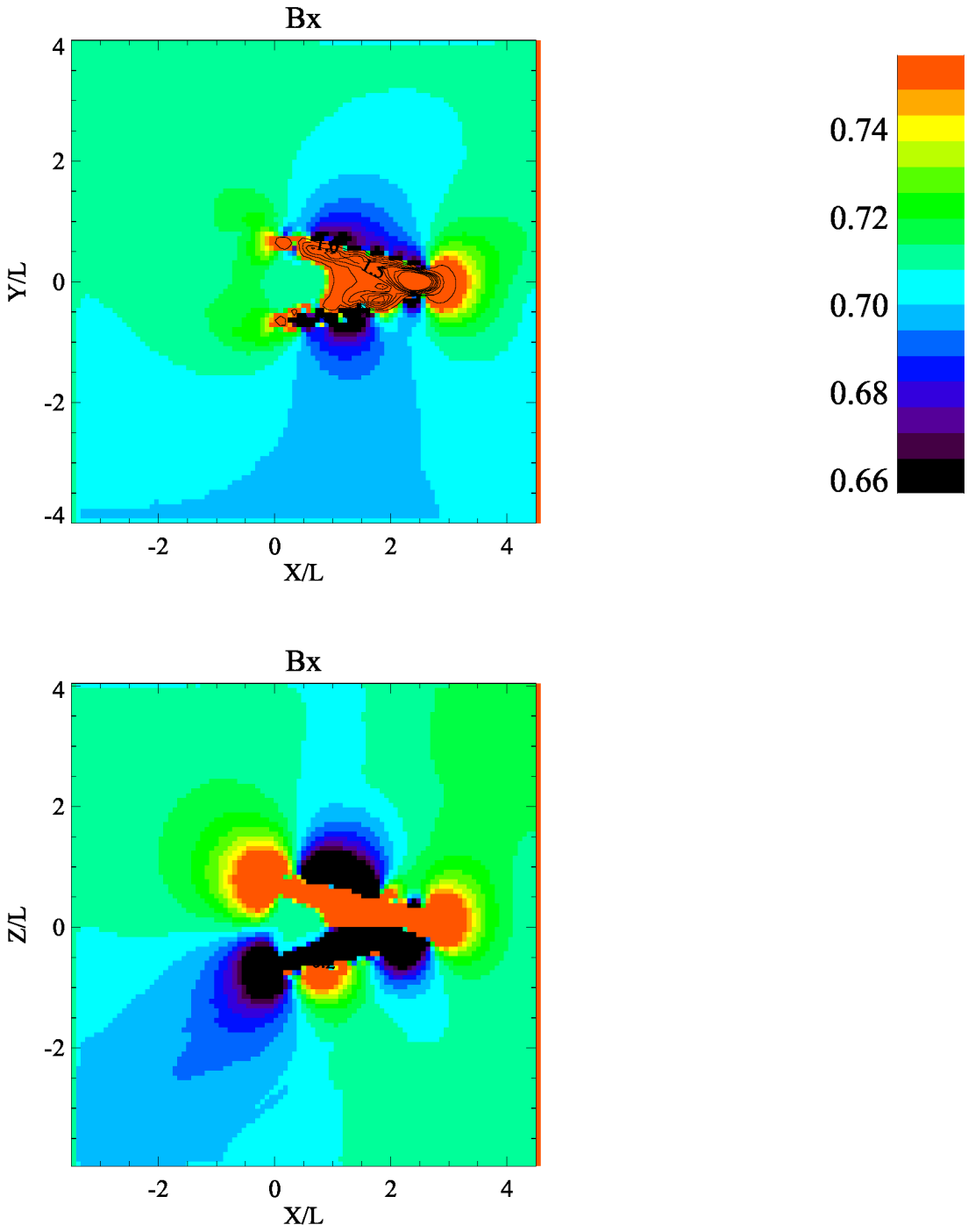

Figure 46. Magnetic field component B_x in the y-x ($z = 0$) and z-x ($y = 0$) planes. $U_0 = 200\,\mathrm{km/s}$, $M_A = 2$, $B_0 = 6250\,\mathrm{nT}$, $n_{SW} = 10^4\,\mathrm{cm}^{-3}$, $\beta_\mathrm{p} = 0.1$, $\beta_\mathrm{e} = 0.0125$, $\theta_{bu} = 45^o$, $t = 13.6\,T_{ce}(1.875\,T_{transit.})$

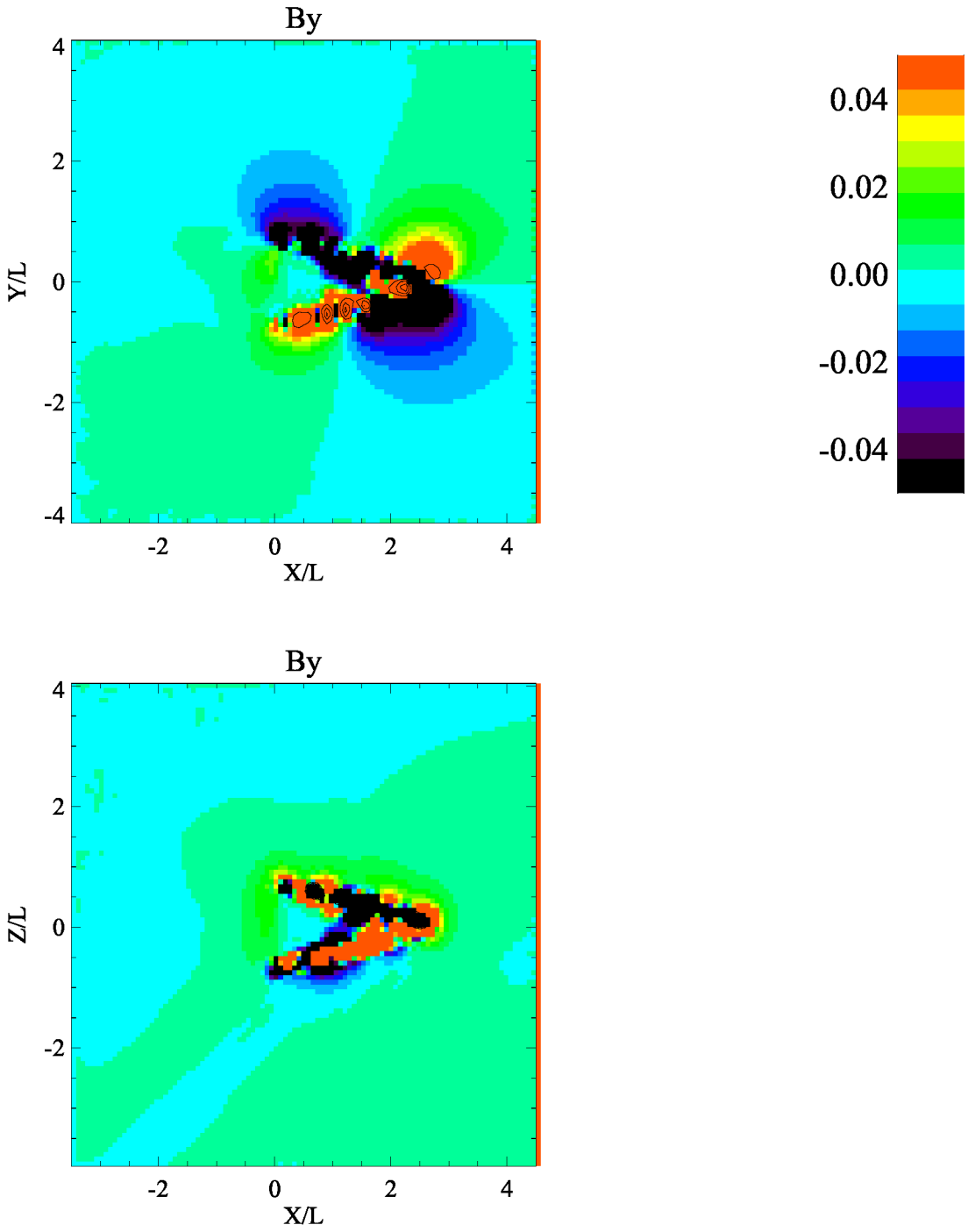

Figure 47. Magnetic field component $B_y(6250\,\mathrm{nT})$ in the y-x ($z = 0$) and z-x ($y = 0$) planes. $U_0 = 200\,\mathrm{km/s}$, $M_A = 2$, $B_0 = 6250\,\mathrm{nT}$, $n_{SW} = 10^4\,\mathrm{cm}^{-3}$, $\beta_\mathrm{p} = 0.1$, $\beta_\mathrm{e} = 0.0125$, $\theta_{bu} = 45^o$, $t = 13.6\,T_{ce}(1.875\,T_{transit.})$

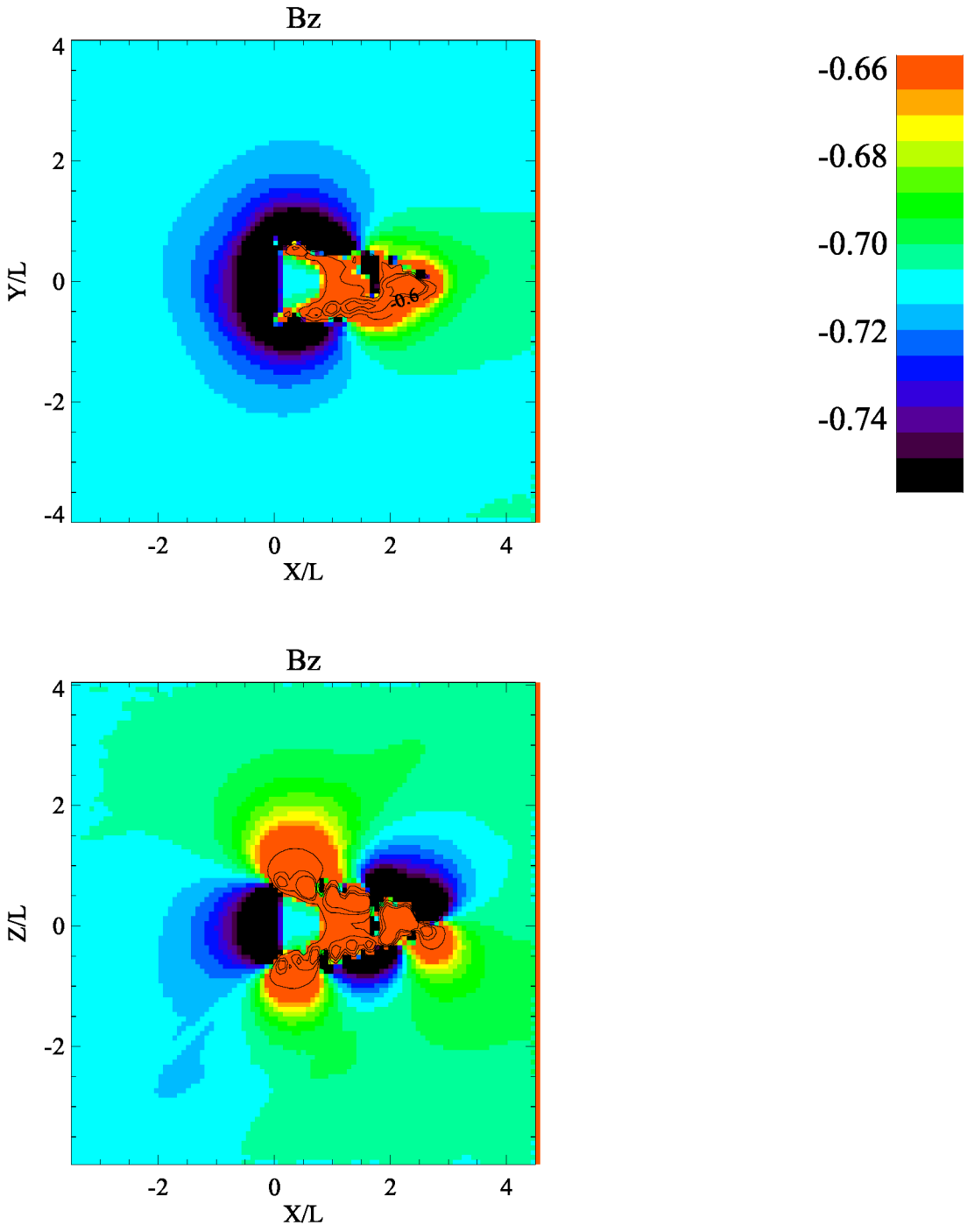

Figure 48. Magnetic field component $B_z(6250\,\mathrm{nT})$ in the y-x ($z = 0$) and z-x ($y = 0$) planes. $U_0 = 200\,\mathrm{km/s}$, $M_A = 2$, $B_0 = 6250\,\mathrm{nT}$, $n_{SW} = 10^4\,\mathrm{cm}^{-3}$, $\beta_\mathrm{p} = 0.1$, $\beta_\mathrm{e} = 0.0125$, $\theta_{bu} = 45^o$, $t = 13.6\,T_{ce}(1.875\,T_{transit.})$

REPORT DOCUMENTATION PAGE

Form Approved
OMB No. 0704-0188

1. REPORT DATE *(DD-MM-YYYY)*	2. REPORT TYPE	3. DATES COVERED *(From - To)*
01-12-2010	Technical Memorandum	January 1, 2008 - January 1, 2009

4. TITLE AND SUBTITLE

The Interaction of the Solar Wind with Solar Probe Plus
— A 3D Hybrid Simulation
Report No. 1: The study for the distance 4.5Rs

5a. CONTRACT NUMBER

5b. GRANT NUMBER
NCC5–494

5c. PROGRAM ELEMENT NUMBER

6. AUTHOR(S)

Alexander S. Lipatov, Edward C. Sittler, Richard E. Hartle, and John F. Cooper

5d. PROJECT NUMBER

5e. TASK NUMBER

5f. WORK UNIT NUMBER
93672302010619

7. PERFORMING ORGANIZATION NAME(S) AND ADDRESS(ES)

Goddard Space Flight Center
Greenbelt, MD 20771

8. PERFORMING ORGANIZATION REPORT NUMBER
2011-00670

9. SPONSORING/MONITORING AGENCY NAME(S) AND ADDRESS(ES)

National Aeronautics and Space Administration
Washington, DC 20546-0001

10. SPONSORING/MONITOR'S ACRONYM(S)
NASA GSFC

11. SPONSORING/MONITORING REPORT NUMBER
TM-2010-215862

12. DISTRIBUTION/AVAILABILITY STATEMENT

Unclassified-Unlimited, Subject Category: 75, 90
Report available from the NASA Center for Aerospace Information, 7115 Standard Drive, Hanover, MD 21076. (443)757-5802

13. SUPPLEMENTARY NOTES

14. ABSTRACT

Our report devotes a 3D numerical hybrid model of the interaction of the solar wind with the Solar Probe spacecraft. The SPP model includes 3 main parts, namely, a non-conducting heat shield, a support system, and cylindrical section or spacecraft bus that contains the particle analysis devices and antenna. One observes an excitation of the low frequency Alfven and whistler type wave directed by the magnetic field with an amplitude of about (0.06-0.6) V/m. The compression waves and the jumps in an electric field with an amplitude of about (0.15-0.7) V/m were also observed. The wave amplitudes are comparable to or greater than previously estimated max wave amplitudes that SPP is expected to measure. The results of our hybrid simulation will be useful for understanding the plasma environment near the SPP spacecraft at the distance 4.5 Rs. Future simulation will take into account the charging of the spacecraft, the charge separation effects, an outgassing from heat shield, a photoionization and an electron impact ionization effects near the spacecraft.

15. SUBJECT TERMS

Solar Probe Plus, plasma physics, astrophysics, Solar wind; Alfv´en waves, Whistlers, ionospheres, atmospheres, induced magnetospheres, magnetic barrier, satellites

16. SECURITY CLASSIFICATION OF:			17. LIMITATION OF ABSTRACT	18. NUMBER OF PAGES	19b. NAME OF RESPONSIBLE PERSON
a. REPORT	b. ABSTRACT	c. THIS PAGE			Edward C. Sittler
U	U	U	U	78	19b. TELEPHONE NUMBER *(Include area code)* (301) 286-9215